

An ab initio study of the band gaps of high-entropy silicides based on FeSi₂

Jørn-Marcus Høylo-Rosenberg



Thesis submitted for the degree of
Master in Materials Science for Energy and
Nanotechnology
60 credits

Department of Chemistry
Faculty of mathematics and natural sciences

UNIVERSITY OF OSLO

Spring 2022

An ab initio study of the band gaps of high-entropy silicides based on FeSi₂

Jørn-Marcus Høylo-Rosenberg

© 2022 Jørn-Marcus Høylo-Rosenberg

An ab initio study of the band gaps of high-entropy silicides based on
FeSi₂

<http://www.duo.uio.no/>

Printed: Reprosentralen, University of Oslo

Abstract

In this work we have set out to examine the band gaps of potential high-entropy stabilized transition metal silicides, based on the FeSi₂ semiconductor. Here, we have performed a first principles study utilizing density functional theory in combination with the special quasi-random structures method. The band gaps has been evaluated primarily with the PBE GGA functional, but also the SCAN meta-GGA functional and hybrid functional HSE06 has been applied in this project. Potential alloys has been examined by generating a set of distinct supercells of the FeSi₂ structure, where the iron sites are populated quasi-randomly by a combination of 3d transition metals. The alloys we have studied in this project are comprised of combinations of Cr, Fe, Mn, Ni, Co and Ti, most emphasis has been put on the Cr-Fe-Mn-Ni-Si system. In the (CrFeMnNi)Si₂ composition, we can report several semiconducting supercells with band gaps ranging between 0 - 0.05 eV using PBE GGA. The band gaps displayed significant spin polarization, in the spin up direction most supercells pointed to a gap around 0.3 eV. Contrary, the band gaps in spin down varied between 0 - 0.05 eV. Accordingly, we found a finite magnetic moment in this alloy equal to 0.083 μ_B , this was attributed mainly to chromium and manganese atoms in the lattice. Successive simulations of alloys based on the Cr-Fe-Mn-Ni-Si system with non-equimolar distribution of 3d elements, resulted most frequently in half-metallic structures with a spin up band gap ranging between 0.1 eV and 0.5 eV. Of the different compositions we tested, the ones either rich in manganese and/or poor in chromium showed the most promise with respect to the band gap. In particular, we report a PBE total band gap equal to 0.1 eV in the Cr₃Fe₅Mn₅Ni₃Si₃₂ composition. Lastly, we looked at compositions where either Cr, Mn or Ni were replaced by either cobalt or titanium. This yielded predominately metallic compounds, where the lack of band gaps could be ascribed to defect states at the band edges.

Acknowledgments

I would like to express my gratitude towards my supervisor Ole Martin Løvvik. For always being available and prioritize my work from the first day to the last. Coming into this project, I had no prior knowledge of density functional theory or quantum mechanical modeling. So, for your guidance in this project I am truly thankful, and know that this project would have been impossible without you. I also feel as if I have made a friend and someone I could talk through throughout this project. Due to the oddity of these recent years with the covid-19 outbreak and self-isolation this have been very important to my sanity and mental health combined with the difficulty involved in writing a master theses. On this same note, I would like to thank all my friends and family members that have been there and believed in me, and always reminding me to stay positive.

Contents

1	Introduction	1
I Theory		3
2	High-Entropy alloys	4
2.1	Fundamentals	4
2.2	Core effects and properties	7
3	Modeling of random alloys	9
3.1	The Special Quasi-random Structures method	9
3.1.1	Mathematical description	10
3.1.2	Applications to high-entropy alloys	13
4	Density Functional Theory	16
4.1	Review of Quantum Mechanics	17
4.1.1	The Shrödinger equation	17
4.1.2	Approximations to the many-body Shrödinger equation	18
4.2	Kohn-Sham density functional theory	19
4.2.1	Density functional theory	20
4.2.2	The Kohn-Sham Equation	20
4.3	Limitations of DFT	22
II Method		24
5	Practical aspects of DFT	25
5.1	The Exchange-Correlation functional	25
5.1.1	Local density approximation	26
5.1.2	Generalized gradient approximation	26
5.1.3	Meta-GGA	26
5.1.4	Hybrid functionals	27
5.1.5	Outlook	27
5.2	Plane waves and reciprocal space	28
5.3	Self-consistent field calculation	30

6 Computational details	32
6.1 Settings and dependencies	32
6.2 Material	33
III Results and Discussion	35
7 The high-entropy silicide (CrFeMnNi)Si₂	36
7.1 β -FeSi ₂	36
7.2 (CrFeMnNi)Si ₂	37
7.2.1 The band gap	39
7.2.2 Local and projected density of states	42
7.2.3 The band gap of (CrFeMnNi)Si ₂ with SCAN and HSE06	45
7.2.4 Pair distribution functions	50
7.2.5 Charge density	51
7.2.6 SQS size	52
8 Alternative compositions	56
8.1 Exploring the quaternary phase diagram of Cr, Fe, Mn and Ni.	56
8.2 High-entropy silicides with cobalt/titanium	61
8.3 Negative systems	65
IV Conclusion and future work	66
9 Conclusion	67
10 Future work	69
A Figures	70
A.1 Density of states	70
A.2 Projected density of states	72
A.3 Charge density	73

List of Figures

2.1	Formation of HEAs based on $\Omega = \frac{T_m \delta S_{\text{mix}}}{ \Delta H_{\text{mix}} }$, the atomic size effect δ , and number of constituents N . Figures adopted from [11]	6
2.2	A schematic illustration of lattice distortion in high-entropy alloys, compared to conventional materials. Figure from [14].	8
3.1	Pair distribution functions of (a) 20-atom and (b) 250-atom SQSs of CoCrFeMnNi. Figure adopted from [21].	13
3.2	Density of states of FCC CoCrFeNi with MC/MD and SQS. figure adopted from [21].	14
3.3	Pair distribution functions of HCP CoOsReRu, from MC/MD and SQS simulations. Figure adopted from [21].	14
4.1	Number of DFT studies per year from 1980 to 2021. Gathered from [29].	16
5.1	Jacob's ladder, developed by Perdew. Illustrating the relationship between accuracy and complexity of different exchange-correlation functionals. Figure from [35].	25
5.2	Flow chart of the self-consistent field calculation scheme of DFT calculations. Figure adopted from the lecture notes of the course FYS-MENA4111 at the University of Oslo [27].	31
6.1	Five distinct 48-atom SQSs of $\text{Cr}_4\text{Fe}_4\text{Mn}_4\text{Ni}_4\text{Si}_{32}$ based on the $\beta-\text{FeSi}_2$ crystal structure. Manganese atoms are represented as purple spheres, chromium as dark blue and silicon as light blue, followed by iron and nickel presented as gold and silver spheres respectively. The respective SQSs are denoted as A, B, C, D and E. Figures illustrated with VESTA [60]	34
7.1	Density of states [states/eV] of $\beta\text{-FeSi}_2$	37
7.2	Density of states [states/eV] of SQS D of $(\text{CrFeMnNi})\text{Si}_2$	39
7.3	Density of states [states/eV] of SQS B of $(\text{CrFeMnNi})\text{Si}_2$	39
7.4	Density of states [states/eV] of SQS A of $(\text{CrFeMnNi})\text{Si}_2$	40
7.5	Local density of states [states/eV] of Si, in SQS D of $(\text{CrFeMnNi})\text{Si}_2$	43
7.6	Local density of states [states/eV] of (a) Cr, (b) Mn, (c) Fe, (d) Ni in SQS D of $(\text{CrFeMnNi})\text{Si}_2$	43

7.7	Projected density of states [states/eV] of SQS D of (CrFeMnNi)Si ₂	44
7.8	Projected density of states [states/eV] of SQS D and B of (CrFeMnNi)Si ₂ around the Fermi energy.	44
7.9	Density of states [states/eV] illustrating the difference between band gaps of SQS E and D of (CrFeMnNi)Si ₂ with PBE and SCAN.	46
7.10	Density of states [states/eV] of SQS B of (CrFeMnNi)Si ₂ with HSE06.	46
7.11	Pair distribution functions of SQS D (top) and B (bottom) of (CrFeMnNi)Si ₂	50
7.12	Contour plots of the Charge density of SQS A, B, D and E of (CrFeMnNi)Si ₂	51
7.13	CPU time of 48, 96 and 192-atom SQSs of (CrFeMnNi)Si ₂ . . .	52
7.14	Density of states [states/eV] of SQS E of the 192-atom model of (CrFeMnNi)Si ₂	54
7.15	Pair distribution functions of (CrFeMnNi)Si ₂ (top) 48-atom SQS, (middle) 96-atom SQS, (bottom) 192-atom SQS.	55
8.1	Projected density of states [states/eV] of (a) Cr ₃ Fe ₃ Mn ₇ Ni ₃ Si ₃₂ (SQS B), (b) Cr ₅ Fe ₅ Mn ₃ Ni ₃ Si ₃₂ (SQS C), (c) Cr ₅ Fe ₃ Mn ₅ Ni ₃ Si ₃₂ (SQS A), (d) Cr ₃ Fe ₅ Mn ₅ Ni ₃ Si ₃₂ (SQS D)	58
8.2	Projected density of states [states/eV] of Cr ₃ Fe ₃ Mn ₃ Ni ₇ Si ₃₂ around the Fermi energy.	59
8.3	Projected density of states [states/eV] of (CrFeMnCo)Si ₂ . . .	63
8.4	Projected density of states [states/eV] of alloys comprised of combinations of Cr, Fe, Mn, Ni, Co, Ti and Si.	64
8.5	Density of states [states/eV] of SQS A and E of (CoFeMnNi)Si ₂ . . .	64
A.1	Density of states [states/eV] of SQS E of (CrFeMnNi)Si ₂ . . .	70
A.2	Density of states [states/eV] of SQS C (CrFeMnNi)Si ₂ . NE-DOS represents the number of points in the DOS calculation.	71
A.3	Density of states [states/eV] of SQS C of Cr ₅ Fe ₅ Mn ₃ Ni ₃ Si ₃₂ , illustrating the small finite DOS at E_F due to the impurity gap.	71
A.4	Projected density of states [states/eV] of SQS A of (CrFeMnNi)Si ₂	72
A.5	Projected density of states [states/eV] of SQS B of (CrFeMnNi)Si ₂	72
A.6	Projected density of states [states/eV] of SQS E of (CrFeMnNi)Si ₂	73
A.7	Contour plot of the charge density of SQS C of (CrFeMnNi)Si ₂ .	73

List of Tables

6.1	Convergence tests of the cutoff energy and density of k-points, with respect to the total energy. The tests were conducted for a 48-atom supercell of Cr ₄ Fe ₄ Mn ₄ Ni ₄ Si ₃₂	33
7.1	Total energy per atom (Toten), final magnetic moment per atom (Mag), band gap (E_G) and formation energy (E_{FPA}) of 5 SQS of (CrFeMnNi)Si ₂	37
7.2	Band gap of five SQSs of (CrFeMnNi)Si ₂ in spin up, spin down and total. The band gaps are calculated from the Kohn-Sham eigenvalues of PBE simulations.	40
7.3	Band gap of SQS D of (CrFeMnNi)Si ₂ as a function of occupancy cutoff <i>occ</i> in the eigenvalues.	41
7.4	Band gaps of five supercells of (CrFeMnNi)Si ₂ in spin up, spin down and total, calculated with PBE, SCAN and HSE06 functionals.	45
7.5	Minimum gap between k-point in valence band and conduction band in SQS B of (CrFeMnNi)Si ₂ from PBE, SCAN and HSE06 simulations.	47
7.6	Band gap of five supercells of (CrFeMnNi)Si ₂ from HSE06 calculations using Gaussian smearing, with smearing width σ equal to 0.05 eV and 0.005 eV, and the tetrahedron method (TBC). "-" means that the band gap are unchanged between occ = 0.5 and occ = 0.01.	48
7.7	Total energy (Toten), magnetic moment (Mag) and formation energy (E_{extFPA}) of 48, 96 and 192 atom SQSs of (CrFeMnNi)Si ₂	53
7.8	Band gap of SQSs of 48, 96 and 192-atoms of (CrFeMnNi)Si ₂ . The names are arbitrary, A in 48 does not equal A in 96 or A in 192. The values listed in <i>italic</i> relate to a defect band gap. Structures listed in bold text represents the most stable supercell of the set of SQSs.	53
8.1	Total energy (Toten), magnetic moment (Mag) and formation energy E_{FPA} of various compositions of the Cr-Fe-Mn-Ni-Si system.	56

8.2	Band gaps of various compositions of the Cr-Fe-Mn-Ni-Si system. The most stable SQS of a set is highlighted in bold text, defect/impurity band gaps are listed in <i>italic</i> . Some SQSs were excluded from the table due to unsuccessful calculations. All band gaps calculated with PBE GGA.	57
8.3	Total energy (Toten), magnetic moment (Mag) and formation energy (E_{FPA}) of alloys based on combinations of Cr, Fe, Mn, Ni, Co, Ti and Si.	61
8.4	Magnetic moment of the most stable SQS of alloys comprised of combinations of Cr, Fe, Mn, Ni, Co, Ti and Si.	62
8.5	The band gaps in spin up/down and total of the most stable SQS of alloys comprised of combinations of Cr, Fe, Mn, Ni, Co, Ti and Si. Calculated from eigenvalues with different occupancy cutoff <i>occ</i> using PBE GGA.	63

Chapter 1

Introduction

A major concern in the energy sector is the loss of energy as waste heat. For instance, [1] estimated that about 60 percent of the energy produced in USA in 2012 was lost as waste heat. Contrary to common energy sources that suffer from this problem of losing energy to heat, thermoelectricity can generate electricity from heat by what's known as the Seebeck effect [2]. Hence, thermoelectricity can have many promising applications, for example one could imagine a conjunction between thermoelectric generators and mechanical generators to recover a portion of the waste heat produced by the latter. However, currently thermoelectricity is of limited practical use due to a lack of efficient thermoelectric materials. This can be explained from the thermoelectric figure of merit, composed of the Seebeck Coefficient S , electrical conductivity σ , working temperature T and the thermal conductivity κ , in the following relation [3]

$$zT = \frac{S^2 \sigma T}{\kappa}. \quad (1.1)$$

An efficient thermoelectric material consists of three dependent variables: A high Seebeck coefficient, high electrical conductivity, and low thermal conductivity. A popular strategy to achieve this relation is the phonon-glass electron crystal approach [4], in which one will introduce complexity and anharmonicity to the crystal lattice by some means to increase levels of phonon scattering, without also increasing the scattering of electrons. Furthermore, good thermoelectrics are narrow gap semiconductors. [5] found highest zT values for semiconductors with band gap between 6-10 $k_B T$, which at room temperature equals around 0.2 eV.

In this project we will look at high-entropy alloys as potential thermoelectric materials. High-entropy alloys are a novel material class that extends the concept of traditional binary-alloys such as steel, to multi-component alloys. The name "high-entropy" stems from that the materials are stabilized by the high configurational entropy caused by alloying multiple constituents. These materials are in particular known for their strong mechanical properties [6], such as high strength at elevated temperatures. Moreover, evidence of low thermal conductivity originating from the disordered crystal structure. Hence, provided that we can find narrow gap

high-entropy alloys, these could be relevant and promising high zT thermoelectric materials.

Specifically, in this project we will look at high-entropy silicides. These are a lesser studied subclass of high-entropy alloys. The first experimentally synthesized high-entropy silicide was found in 2019 by Gild. et al [7]. He studied a first of its kind single-phase high-entropy disilicide $(\text{MoNbTaW})\text{Si}_2$. This silicide adopted the hexagonal C40 crystal structure, and displayed low thermal conductivity compared to conventional disilicides in the equivalent crystal structure. Additionally, very recently a master student at the University of Oslo managed to synthesize three phases of non-cubic high-entropy silicides based on Si, Co, Cr, Fe, and Ni in both hexagonal and orthorhombic symmetries [8]. We base this project on silicides because firstly silicon and various transition metal-silicides are environmentally sound and silicon in particular is heavily applied in micro-electronic devices and renewable energy sources such as solar power, thus silicon based alloys could readily be implemented into these technologies. Secondly, transition metal silicides offer a good range of initial compounds with suitable band gaps for thermoelectrics [9].

This project is performed by ab initio methods in the framework of density functional theory. The disordered structure of high-entropy alloys are handled with a numerical method called special quasi-random structures. The particular materials investigated in this project will be based on the semiconductor $\beta\text{-FeSi}_2$. We will mainly investigate the band gap of such alloys, for this we employ three classes of functionals in DFT: GGA, meta-GGA and hybrid functionals. In addition, we will perform a brief analysis of the stability and magnetism. The potential high-entropy silicides are studied by constructing five distinct supercells of the master compound, where the iron sites are populated by a quasi-random distribution between 3d transition metals. Special emphasis are placed on alloys consisting of Cr, Fe, Mn and Ni, as these along with silicon are sustainable non-toxic elements.

We begin this project by reviewing the fundamentals and properties of high-entropy alloys, thereafter we present a theoretical description of the computational methods used in this project, SQS, and DFT. Next, we discuss various practical aspects of DFT, such as the exchange-correlation functionals and numerical convergence. Following, is a section on the computational settings and dependencies necessary to reproduce the results presented in this thesis. Finally, we present and discuss the results, which begins with the high-entropy silicide $(\text{CrFeMnNi})\text{Si}_2$, followed by various derivatives and alternatives to this system. In the end we give a brief conclusion of our work and discuss possible directions for future research.

Part I

Theory

Chapter 2

High-Entropy alloys

High-Entropy Alloys (HEAs) has become an increasingly popular field in materials science, from to the large flexibility and possibilities for discovering new materials with unique properties. Since the original discovery in 2004, as of 2015 there has been over 1000 published journal articles on high-entropy alloys [10]. In the following section we will cover the fundamentals and some applications of high-entropy alloys. This section is based on the fantastic description of HEAs in the book "High-Entropy Alloys - Fundamentals and Application", in particular chapters 1,2,3 and 7 [10], [11], [12], [13], and references therein.

2.1 Fundamentals

A high entropy alloy can in a way be compared to a smoothie. In a smoothie one can produce unique combinations of flavors and nutritional values based on both the properties of the individual fruits and vegetables, and their interplay in the mixture. In materials science, a similar approach can be applied to generate a large range of materials with tunable properties depending on the intended application. In respect to HEAs, examples can be increased strength, ductility, corrosive resistance and low thermal conductivity. Moving on from the rather banal fruit analogy, a high-entropy alloy can be defined from two conditions:

1. The material consists of at least 5 distinct elements, where each element contribute between 5-35% of the composition.
2. The total configurational entropy is greater than $1.5R$, where R is the gas constant.

The latter is an especial case for high-entropy alloys. The ideal configurational entropy of a random N-component solid-solution is described as

$$\Delta S_{\text{config}} = -R \sum_{i=1}^N X_i \ln X_i, \quad (2.1)$$

where X_i is the mole fraction of the i th component. Its clear that ΔS_{config} increase with a higher number of constituents in the mix. For instance,

the ideal configurational entropy of a equimolar binary alloy is 0.69 R, as opposed to 1.61 R in a five-component equimolar alloy. If we neglect the other factors that influence the formation of solid solutions (will be covered later), from Gibbs free energy

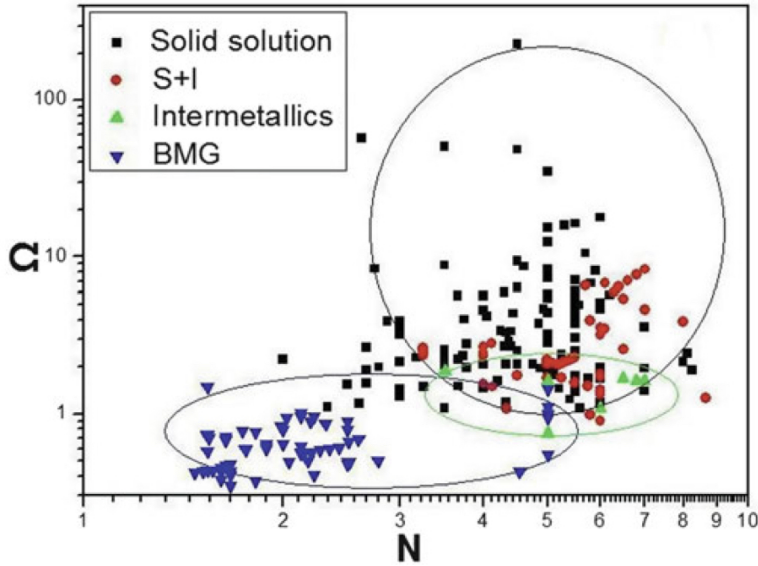
$$\Delta G_{\text{mix}} = \Delta H_{\text{mix}} - T\Delta S_{\text{mix}}, \quad (2.2)$$

the two primary factors in formation of solid solution is the mixing enthalpy, which is the driving force to form compounds, and the mixing entropy which is the driving force to form random solid solutions. At elevated temperatures especially, the energy associated to the entropy of the system becomes comparative to the mixing enthalpy and can impact the formation. In summary, the overall concept of high-entropy alloys is that through alloying a greater number of elements, the gain in configurational entropy of the system prohibits the formation of intermetallic compounds, in favor of random solid solution. The random term simply relate to the various components occupying lattice positions based on probability. In fact, a narrower definition of high-entropy alloys would be structures with a single-phase disordered solid solution. The two "definitions" given previously, can be considered as guidelines for the latter.

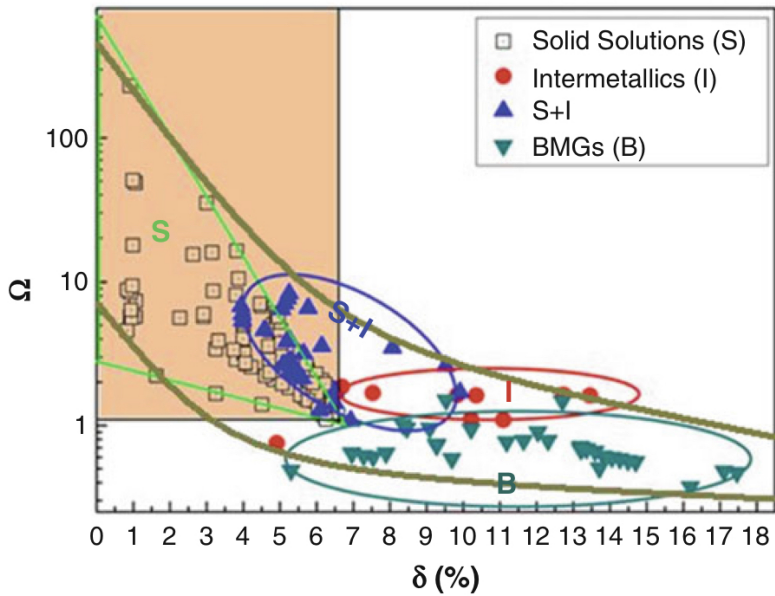
Although the mixing entropy mentioned above plays a central role in the formation, there are other factors to consider that can either favor or oppose the formation of a single disordered phase. One of these is the atomic size effect, which is related to the differences in atomic size between constituents in the alloy. This quantity is denoted δ . Y. Zhang et al. in 2008 illustrated the relationship between ΔH_{mix} and δ . When δ is very small, in other words when the alloys are comprised of elements with similar atomic sizes, the elements have an equal probability to occupy lattice sites to form solid solutions, but the mixing enthalpy is not negative enough to promote formation of solid solution. Increasing δ results in greater ΔH_{mix} , but leads to a higher degree of ordering. The formation of solid solution high-entropy alloys occur in a narrow range of δ values, that satisfy both the enthalpy of mixing and the disordered state. Recently, Yang and Zhang proposed the parameter Ω to evaluate the stability of high-entropy alloys. This quantity is a product of the melting temperature T_m , mixing entropy and mixing enthalpy in the following relation

$$\Omega = \frac{T_m \delta S_{\text{mix}}}{|\Delta H_{\text{mix}}|}. \quad (2.3)$$

They found that the formation of single disordered solid solution occurs at $\Omega \geq 1.1$ and $\delta \leq 6.6\%$, while compounds such as intermetallics form for greater values of δ and lesser values of Ω . Similarly, replacing the atomic size effect with the number of elements results in an equivalent condition. These findings are summarized in figure 2.1.



(a) HEA formation based on Ω and the atomic size effect δ



(b) HEA formation based on Ω and the number of constituents N

Figure 2.1: Formation of HEAs based on $\Omega = \frac{T_m \delta S_{\text{mix}}}{|\Delta H_{\text{mix}}|}$, the atomic size effect δ , and number of constituents N . Figures adopted from [11]

An important quantity in terms of characterizing high-entropy alloys, is the total number of valence electrons VEC. Derived from the work of Guo et al. on the phase stability of the $\text{Al}_x\text{CrCuFeNi}_2$ HEA, the VEC can be directly related to the crystal structure of high-entropy alloys. A lower VEC stabilize the BCC phase, while higher values stabilize FCC, in between is a mixture of the two. Specifically values greater than 8.0 stabilize FCC, and values bellow 6.87 favor BCC. However, these boundaries are not rigid when including elements outside of transition metals, exceptions has also

been found for high-entropy alloys consisting of manganese. Although a heavy majority of reported high-entropy alloys that form solid solutions has been found to adopt simple cubic structures, such as FCC and BCC. In addition to the high-entropy silicides mentioned in the introduction, recent studies have reported HEAs in less symmetric structures, such as $\text{CoFeMnTi}_x\text{V}_y\text{Zr}_z$, CrFeNiTiVZr and CoFeNiTi in HCP, as well as the $\text{Ti}_{35}\text{Zr}_{27.5}\text{Hf}_{27.5}\text{Ta}_5\text{Nb}_5$ HEA in the orthorhombic crystal system.

2.2 Core effects and properties

In this section, we will summarize the discussion above into four core effects that can be used to explain high entropy alloys, and discuss some of the properties observed in various HEAs. The first core effect is called the "high-entropy effect", as explained in the previous section the high configurational entropy of HEAs compared to traditional solids or even binary alloys is central to stabilize the disordered phase ahead of intermetallic or strongly ordered structures. This effect can result in enhanced strength and ductility. From considerations of Gibbs free energy, we see that this effect is most prominent at elevated temperatures.

The second effect is the "severe lattice distortion effect" that arises from the fact that every element in a high-entropy structure is surrounded by non-homogeneous elements, thus leading to severe lattice strain and stress. The overall lattice distortion is additionally attributed to the differences in atomic size, bonding energies and crystal structure tendencies between the components. Therefore, the total lattice distortion observed in HEAs are significantly greater than that of conventional alloys. This effect mostly affects the strength and conductivity of the material, such that a higher degree of distortion yields greater strength and greatly reduces the electronic and thermal conductivity due to increased electron and phonon scattering. An upside to this is that the scattering and following properties become less temperature dependent given that it originates from the lattice rather than thermal vibrations. The concept of lattice strain in high-entropy alloys can be visualized as in figure 2.2 below.

The two remaining effects, "sluggish diffusion" and "cocktail effect" can be summarized swiftly. The first is a direct consequence of the multi-component layout of high-entropy alloys that results in slowed diffusion and phase transformation because of the number of different elements that is involved in the process. The most notable product from this effect is an increased creep resistance. Lastly, we have the cocktail effect which is identical to the smoothie analogy mentioned previously, in that the resultant characteristics of a high-entropy alloy is a combination of both the individual elements and their interplay. This is possibly the most promising concept behind high-entropy alloys, which fuels researchers with ambitions to discover highly optimized materials by meticulously combining and predicting properties from different elements. Examples of this can be the refractory HEAs developed by the "Air Force Research Laboratory" that significantly exceeded the melting points and strength of

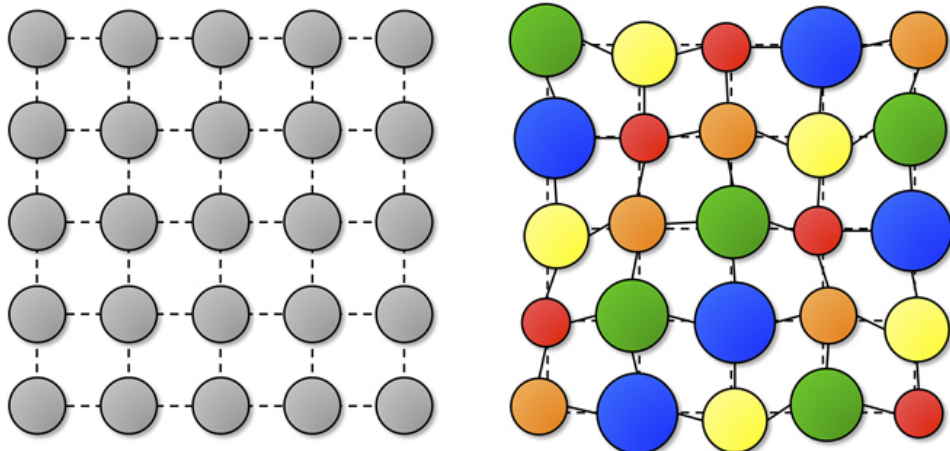


Figure 2.2: A schematic illustration of lattice distortion in high-entropy alloys, compared to conventional materials. Figure from [14].

previous Ni or Co-based superalloys, by alloying specifically refractory elements such as Mo, Nb and W. Another example is the research conducted by Zhang et al. on the high-entropy system $\text{FeCoNi}(\text{AlSi}_x)$, with ($0 < x < 0.8$). In this HEA it was found that increased amount of either Al or Si lowered the saturation magnetization of the alloy. By tuning the relative amounts, it was found excellent properties for an $x = 0.2$ HEA in terms of the magnetization, electrical resistivity and yield strength to produce a promising soft-magnet. The same was also found in $\text{Al}_{0.2}\text{CoCrFeNi}$ HEAS, where the addition of Al reduced the ferromagnetism of the alloy, and in CoCrCuFeNiTi_x alloys where $x = 0$ was paramagnetic and $x > 0.8$ showed superparamagnetic properties. In general we find that the saturation magnetism is mostly dependent on the contents and distribution of ferromagnetic elements such as Fe, Co and Ni while the addition of anti-ferromagnets like Cr could be difficult to predict. For example in the ferromagnetic HEA CoFeMnNiX , $X = \text{Al, Cr, Ga, Sn}$, studied in [15], Mn pushed the material to the ferromagnetic phase, meanwhile addition of Cr pushed the material to a paramagnetic phase. Likewise in the equimolar system of CrMnFeCoNi [16], the local magnetic moment of Cr was found to align antiferromagnetic, and the ferromagnetic character was attributed to local magnetic moments around Fe and Mn.

As we have seen from the above examples, what makes high-entropy alloys a particularly interesting and promising field, is that they possesses the ability to be tuned for specific applications and properties, by testing specific combinations and distributions of different elements. In many ways, not indifferent to a smoothie or a cocktail.

Chapter 3

Modeling of random alloys

The disordered structure of high-entropy alloys, in which the alloying elements occupy lattice sites by a random probability, pose a problem on conventional numerical methods. Density functional theory in particular rely heavily on the periodicity of crystalline solids, as we will discover later. In a brute force approach, this could be solved by randomly distribute the solute and solvent atoms over the lattice sites of a large supercell, and average the energy and related properties over a large number of such supercells with varying distributions. Obviously, despite of the computational means accessible today, this approach is far too computationally demanding. Today, there exists a number of possible methods to more efficiently study such structures. Examples are the Virtual Crystal Approximation (VCA), Coherent Potential Approximation (CPA), Special Quasi-random Structure (SQS), and hybrid Monte-Carlo/Molecular Dynamics (MC/MD). A brief overview of the different methods are given in for example [17]. In this project, we will employ the SQS method due to both easy to use implementation and interpretation in the computational framework of this project, in addition to other benefits that will become clear after the following sections.

3.1 The Special Quasi-random Structures method

In the original paper published in 1990 describing the SQS method [18], it was proposed a selective occupation strategy to design special periodic quasi-random structures that exceeded previous methods in both accuracy and cost. The key concept was to create a periodic unit cell of the various components in a finite N lattice site single configuration such that the structure most closely resemble the configuration average of an infinite perfect random alloy. In an attempt to work under the 50 lattice sites boundary of ab initio methods at that time, the working theory was that if one can resemble an infinite perfect random alloy by a periodic finite N cell, also the electronic properties would be similar between the two. The solution to this problem, was that for each N , ie lattice site, to minimize the difference of structural correlation functions between the approximated cell and the perfect random alloy. There are obviously errors involved with

approximating a random alloy by a periodic structure, but by a hierarchical relation to the properties of the material, interactions between distant sites offer negligible small contributions to the total energy of the system. Thus, the aim of the SQS method is focused around optimizing the correlations within the first few shells of a given site.

3.1.1 Mathematical description

Below we give a summary of the mathematical description of the special quasi-random structures method, and cover various statistical methods and notations. For a more comprehensive discussion on these topics and the SQS method, we refer the reader to the article "Electronic properties of random alloys: Special quasirandom structures", by Wei [18].

The different possible atomic configurations are denoted σ . The physical properties of a given configuration is $E(\sigma)$, and $\langle E \rangle$ is the ensemble average over all configurations. In practice, this quantity is unfeasible in terms of computational cost, seeing as the average require calculations and relaxations of all possible configurations, for a binary alloy this is 2^N for a fixed N number of lattice sites. A solution to this is to use the theory of cluster expansions and discretize each configuration into "figures" f . A figure in the lattice is defined in terms of the number of atoms at each vertex k , the order of neighbor distances separating them m , and position in the lattice l . Further, each site in the figure is assigned a spin value \hat{S}_i to denote which element it holds (+1,-1 for a binary alloy). By defining the spin product of spin variables in a figure at lattice position l as $\Pi_f(l, \sigma)$, we can write the average of all locations in the lattice of a given figure f as

$$\Pi_f(\sigma) = \frac{1}{ND_f} \sum_l \Pi_f(l, \sigma), \quad (3.1)$$

where D_f is the number of equivalent figures per site. The brilliance of this notation is that we now can express the physical property $E(\sigma)$ in terms of the individual contributions ϵ_f of a figure f .

$$E(\sigma) = \sum_{f,l} \Pi_f(l, \sigma) \epsilon_f(l) \quad (3.2)$$

The quantity ϵ_f is called the "effective cluster property" and is defined as (for a random binary alloy $A_{1-x}B_x$)

$$\epsilon_f(l) = 2^{-N} \sum_{\sigma}^{2^N} \Pi_f(l, \sigma) E(\sigma). \quad (3.3)$$

Inserting the equation for Π_f into that of $E(\sigma)$, we can describe the previous cluster expansion of $E(\sigma)$ as

$$E = N \sum_f D_f \langle \Pi_f \rangle \epsilon_f. \quad (3.4)$$

Thus, we have successfully managed to reduce the expensive task of sampling all $E(\sigma)$ into calculating the effective cluster properties and

summing over all types of figures. Remembering that $E(\sigma)$ can relate to many physical properties, the most common and applied case is that $E(\sigma)$ is the total energy, while ϵ_f are the many body interaction energies. The cluster expansion above converge rather quickly with increasing number of figures, an effective method is thus to select a set of configurations to evaluate the effective cluster properties. The next step is to select a finite largest figure denoted F , and "specialize" the cluster expansion to a set of N_s periodic structures $\sigma = s$ to obtain the two expressions for $E(s)$ and ϵ_f using matrix inversion to obtain the result for ϵ_f :

$$E(s) = N \sum_f^F D_f \Pi_f(s) \epsilon_f \quad (3.5)$$

$$\epsilon_f = \frac{1}{ND} \sum_s^{N_s} [\Pi_f(s)] - 1 E(s) \quad (3.6)$$

Assuming now that the sum of figures F and N_s periodic structures are well converged, $E(\sigma)$ can be rewritten as a superposition of $E(s)$ as

$$E(\sigma) = \sum_s^{N_s} \xi_s(\sigma) E(s) \quad (3.7)$$

$$\xi_s(\sigma) = \sum_f^F [\Pi_f(s)]^{-1} \Pi_f(\sigma), \quad (3.8)$$

where ξ are the weights. Hence, we have effectively reduced the problem to a convergence problem of the number of figures F and structures N_s . This can be easily solved given that we are dealing with periodic crystal structures s that can employ the general applications of ordered structures from ab initio methods, and increasing F until the truncation error falls bellow a desired threshold. However, this approach requires that the variance of the observable property is much lower than the sample mean, otherwise one would have to employ a much bigger sample size to reach statistical convergence. Because of the different relationships between various physical properties and the correlation functions, one observe different convergence depending on the meaning of E . The idea behind SQS was therefore to design single special structures with correlation functions $\Pi_f(s)$ that most accurately match those of the ensemble average of a random alloy $\langle \Pi_f \rangle_R$.

The correlation functions of an perfect random infinite alloy, denoted as R is defined as

$$\Pi_{k,m}(R) = \langle \Pi_{k,m} \rangle_R = (2x - 1)^l, \quad (3.9)$$

with k, m defined as before and x as the composition ratio of the alloy. In the case of an equimolar alloy ($x = \frac{1}{2}$), the functions equals 0 for all k except $\langle \Pi_{0,1} \rangle_R = 1$. If we now randomly assign either atom A or B to every lattice site, for a sufficiently large value of N , the goal is then to create a single configuration that best match the random alloy. Keeping with the $x = \frac{1}{2}$ case, the problem is now that even though the average

correlation functions of a large set of these structures approaches zero, like for the random alloy. The variance of the average is nonzero meaning that a selected structure of the sample is prone to contain errors. The extent of these errors can be evaluated from the standard deviations

$$v_{k,m}(N) = | < \Pi_{k,m}^2 > |^{\frac{1}{2}} = (D_{k,m}N)^{-\frac{1}{2}}. \quad (3.10)$$

Given the computational aspects, its obvious that economical structures with small N are prone to large errors. In fact, in some cases these errors can result in correlation functions centering around 1, as opposed to 0 for a perfect random alloy.

The degree to which a structure s fails to reproduce the property E of the ensemble-averaged property of the random alloy can be described by a hierarchy of figures

$$< E > - E(s) = \sum'_{k,m} D_{k,m} [(2x - 1)^k - \Pi_{k,m}(s)] \epsilon_{k,m}, \quad (3.11)$$

the prime is meant symbolize the absence of the value 0,1 for k, m . The contribution from the figure property ϵ is smaller in larger figures. In disordered systems the physical property "E" at a given point R falls off exponentially as $|R - R'| / L$, where L is a characteristic length scale relating to the specific property. Using this, the approach of SQS is to specify a set of correlation functions that hierarchically mimic the correlation functions of the random alloy. Meaning that it prioritize the nearest neighbor interactions. With the set of functions decided on, the objective it finally to locate the structures that correspond to the selected structures.

With this approach, [18] managed by mimicking the correlation functions exact for the first two shells, to reduce the computational measures of an accurate model. In this exact study, they matched the results of an $N \rightarrow \infty$ alloy, by an $N = 8$ SQS. In the final section of this chapter, to recover from this lengthy mathematical derivation, we will take a look at recent advances made to the special quasi-random structures method and applications to high-entropy alloys.

3.1.2 Applications to high-entropy alloys

The success of the SQS method is in large part related to the fact that we can create simple periodic structures, this allows for the use of standard DFT methods to calculate properties such as the total energy, charge density and electronic band structure [19], [20]. Despite for the method being developed in mind of a binary random alloy, the approach has successfully been extended to multi-component alloys as well. However, certain obstacles arise when trying to apply the SQS model to high-entropy alloys. An exhaustive analysis discussing several of these factors and comparing the SQS method to alternative methods is presented in [21], by M.C Gao et al. In this section we will go through some of the major findings of his research.

The first initial concern is the size of the supercell. This parameter needs to be balanced between accuracy and cost. A larger SQS cell consisting of a greater number of atoms better encapsulate the disordered structure of HEAs, but both the generation and simulation of such large SQSs come with an increased computational cost. M.C Gao discovered a sensitivity between the registered stability and predicted crystal structures of CoCrFeNi and CoCrFeMnNi HEAs, and the SQS size. Experimentally, both of these are stabilized in FCC. By calculating the enthalpy of formation, it was found that SQSs consisting of less than 64 atoms wrongly predicted the HCP structure as the most stable structure, while larger SQSs correctly predicted the FCC structure. Furthermore, similar outcomes were found with respect to the pair distribution functions of the CoCrFeMnNi HEA as well. This is displayed in figure 3.1, where the Cr-Mn bond is clearly much better modeled in the larger SQS model.

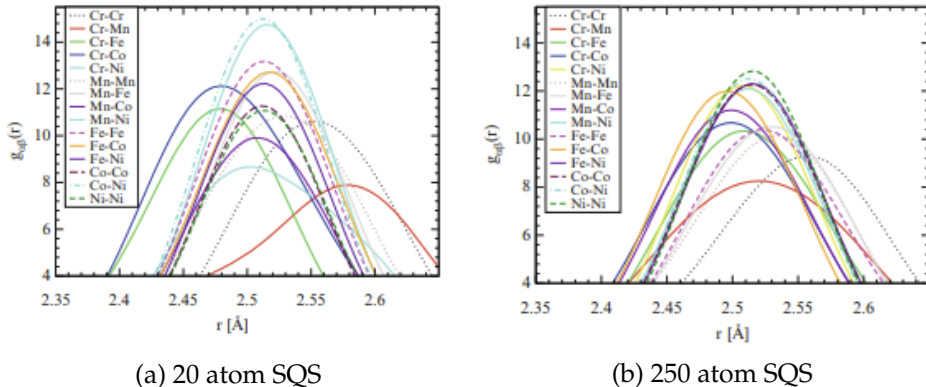


Figure 3.1: Pair distribution functions of (a) 20-atom and (b) 250-atom SQSs of CoCrFeMnNi. Figure adopted from [21].

It was also observed a similar dependence to the SQS size for the entropy and mechanical properties, however these topics are not relevant for this project and will thus not be elaborated further.

Compared to hybrid Monte-Carlo/Molecular Dynamics, we observe from the density of states of the CoCrFeMnNi HEA (figure 3.2), that the SQSs method measures up very well with the much more complicated

method. Furthermore, the SQS method yields comparative outcomes in terms of the pair distribution functions to MC/MD, as seen in figure 3.3 for HCP CoOsReRu.

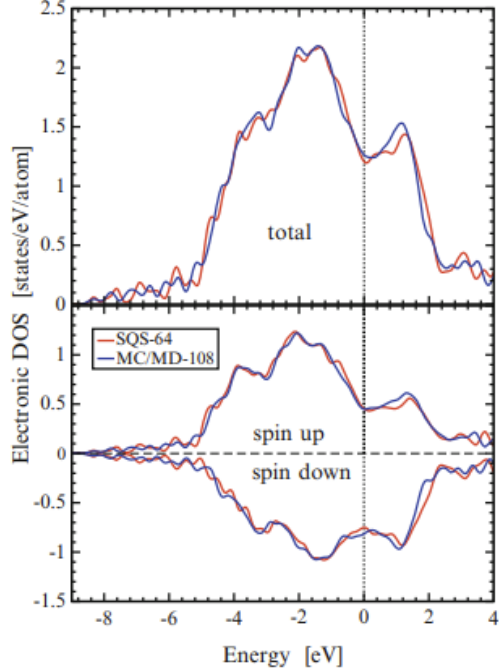


Figure 3.2: Density of states of FCC CoCrFeNi with MC/MD and SQS. figure adopted from [21].

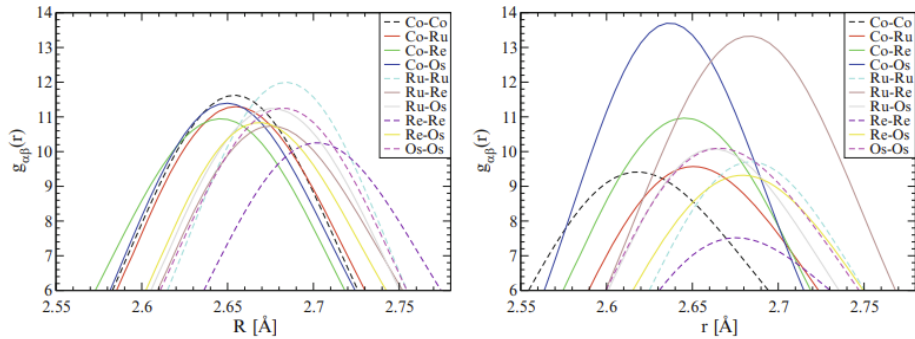


Figure 3.3: Pair distribution functions of HCP CoOsReRu, from MC/MD and SQS simulations. Figure adopted from [21].

The discrepancy in the PDFs between MC/MD simulations and SQS, arises from the fact that SQS fails to include inter-atomic interactions and preferences to the same extent as MC/MD. This is seen in figure 3.3 for the HCP CoOsReRu alloy, in which clear preference of Co-Os and Re-Ru pairs is apparent from MC/MD simulations but not in the SQS model. Compared to the Coherent Potential Approximations, there is indication that the SQS method is less equipped for dealing with specific compositions such as

$A_{1/3}BCDE$ structures, and notably worse performance for paramagnetic materials.

We have seen up until this point that the SQS method utilizes an intelligent approach which allows for simple implementation and calculations while providing results mostly on par to other more intricate and complex methods. One distinct factor concerning SQS that does not apply for CPA and MC/MD, is that one compound can obtain a number of unique configurations (SQSs). For example, quaternary and quinary alloys make for 24 and 124 unique configurations respectively, resulting in an uncertainty of the energy regarding the different configurations. This effect is most prominent in anisotropic lattices such as HCP and alloys with chemically dissimilar constituents, and particularly in smaller SQSs.

Despite of its flaws, especially in recent years SQS have emerged as a viable and trusted method of modeling disordered structures such as HEAs. This is down to both the increasingly available computational power and improvements to the SQS method. The latter in particular saw a boost in 2013 with the introduction of the MC-SQS method [22], short for Monte-Carlo Special Quasirandom Structures. Contrary to the original SQS method that seeks to minimize the difference between the correlation functions of the approximated cell and the true random alloy, this method employ monte-carlo simulations to perfectly match a maximum number of correlation functions. Furthermore, emphasizes an efficient and fast implementation in addition to an exhaustive unbiased search of possible atomic configurations. Following, this is the preferred and most widely used implementation of the SQS method. This has resulted in an increased number of studies utilizing SQSs to investigate high-entropy alloys in recent times, for instance [23], [24], [25], and [26].

Chapter 4

Density Functional Theory

The density functional theory (DFT) is recognized as an overwhelmingly successful and important theory in quantum chemistry and the overall study and understanding of materials. As illustrated in figure 4.1, this is a increasingly popular method with rapid growth to this day due to improvements to both the method and computational power. The overarching goal of DFT is to efficiently solve the many-body Shrödinger equation, therefore we begin this section by reviewing central concepts of quantum mechanics such the Shrödinger equation and the various approximations one can apply to it. Next, follows a derivation of the Kohn-Sham density functional theory, and finally we discuss some of the limitation of the DFT. The content in this section is based on the lecture notes from the course FYS-MENA4111 - "Quantum Mechanical Modeling of Nanomaterials" at the University of Oslo, written by Clas Persson [27], and the book "A practical introduction to DFT" by Sholl [28].

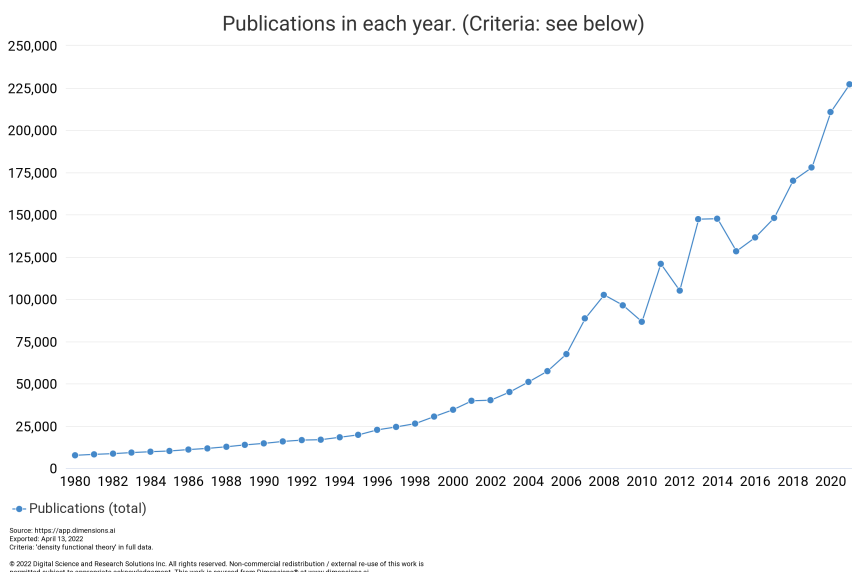


Figure 4.1: Number of DFT studies per year from 1980 to 2021. Gathered from [29].

4.1 Review of Quantum Mechanics

4.1.1 The Shrödinger equation

The fundamental equation that describes a material at microscopic level is the Shrödinger equation. The time-dependent Shrödinger equation for one electron is

$$i\hbar \frac{\partial}{\partial t} \Psi(\mathbf{r}, t) = \hat{H}(\mathbf{r}, t) \Psi(\mathbf{r}, t), \quad (4.1)$$

which consists of the the wavefunction $\Psi(\mathbf{r}, t)$ to describe the electron, and the Hamiltonian $\hat{H}(\mathbf{r}, t)$ where \mathbf{r} and t are the spatial position and time. The Hamiltonian describes the total energy of the system by a kinetic part $T = -\frac{\hbar^2 \nabla^2}{2m_e}$, where m_e is the electron mass and \hbar is the Planck constant, and a potential energy operator U , typically an external potential denoted as $V_{ext}(\mathbf{r}, t)$.

Eigenfunctions of the Hamiltonian are denoted as $\psi_\kappa(\mathbf{r}, t)$, with an energy eigenvalue ϵ_κ for the κ eigenstate. Above we included the time-dependent Shrödinger equation, but almost all cases involving Quantum physics employ rather the time-independent Shrödinger equation in which the external potential is independent of time. This equation is described in equation 4.2 for the eigenvalues E_k of the k -th eigenfunction $\psi_k(\mathbf{r})$ as

$$\left(-\frac{\hbar^2 \nabla^2}{2m_e} + V_{ext}(\mathbf{r}) \right) \psi_\kappa(\mathbf{r}) = E_k \psi_\kappa(\mathbf{r}). \quad (4.2)$$

Solving the single electron time-independent equation often results in infinite eqienstates that an electron can occupy. The most probable state to find the electron in is the lowest energy state called the ground state, this state is indicated by $\kappa = 0$. Extending to a system comprised of multiple particles we have the many-body wavefunction Ψ^{en} in equation 4.3 and the many-body Hamiltonian H^{en} in equation 4.4. In the many-body wavefunction r_j represents the coordinates of the j :th electron and likewise R_α describes the coordinates of the α :th nucleus, and the subscript "en" indicates that both electrons and nuclei are considered.

$$\Psi^{en}(\mathbf{r}, \mathbf{R}) = \Psi^{en}(\mathbf{r}_1, \mathbf{r}_2, \dots, \mathbf{r}_{N_e}, \mathbf{R}_1, \mathbf{R}_2, \dots, \mathbf{R}_{N_n}). \quad (4.3)$$

The many-body Hamiltonian accounts for the kinetic energy T_e of N_e electrons, the interaction energy between electrons U_{ee} , the kinetic energy of N_n nuclei, the coulomb interaction between nuclei U_{nn} , and finally the attractive interaction between nuclei and electrons U_{en} , in final:

$$H^{en} = - \sum_{j=1}^{N_e} \underbrace{\frac{\hbar^2 \nabla_j^2}{2m_e}}_{T_e} - \sum_{\alpha=1}^{N_n} \underbrace{\frac{\hbar^2 \nabla_\alpha^2}{2m_n}}_{T_n} + \underbrace{\sum_{j=1}^{N_e} \sum_{j' < j} \frac{q^2}{|r_j - r_{j'}|}}_{U_{ee}} \\ + \underbrace{\sum_{\alpha=1}^{N_n} \sum_{\alpha' < \alpha} \frac{q^2 Z_\alpha Z_{\alpha'}}{|R_\alpha - R_{\alpha'}|}}_{U_{nn}} - \underbrace{\sum_{j=1}^{N_e} \sum_{\alpha=1}^{N_n} \frac{q^2 Z_\alpha}{|r_j - R_\alpha|}}_{U_{en}}. \quad (4.4)$$

Combining the many-body wavefunction and the many-body Hamiltonian we get the many body Schrodinger equation with total energy eigenvalue E_{κ}^{en} of the whole system in eigenstate κ as

$$H^{en}\Psi_{\kappa}^{en}(\mathbf{r}, \mathbf{R}) = E_{\kappa}^{en}\Psi_{\kappa}^{en}(\mathbf{r}, \mathbf{R}). \quad (4.5)$$

4.1.2 Approximations to the many-body Shrödinger equation

The first step to solving the many-body problem is how the many body wavefunction depends on the single electron wavefunctions. If we consider a simplified system consisting of just two electrons, the problem is reduced to finding $\Psi_{\kappa}(\mathbf{r}_1, \mathbf{r}_2)$ that is a function of $\psi_1(\mathbf{r}_1)$ and $\psi_2(\mathbf{r}_2)$. In the Hartree approach this is solved by assuming that the two electrons are independent of each-other and employ variable separation to express the two particle wavefunction as

$$\Psi_{\kappa}(\mathbf{r}_1, \mathbf{r}_2) = \psi_1(\mathbf{r}_1)\psi_2(\mathbf{r}_2). \quad (4.6)$$

The flaw of the Hartree approach is that the electrons, which are fermions, in this formulation are distinguishable and hence does not obey the Pauli exclusion principle of fermions. This is corrected in the Hartee-Fock approximation which introduces a spin function $\chi_{mp}(s_1, s_2)$ to make it anti-symmetric with respect to the particle coordinates. The Hartree-Fock approximation is expressed as

$$\Psi_{\kappa}(\mathbf{r}_1, \mathbf{r}_2) = \frac{1}{2} \{ \psi_1(\mathbf{r}_2)\psi_2(\mathbf{r}_2) \pm \psi_1(\mathbf{r}_2)\psi_1(\mathbf{r}_1) \} \chi_{\mp}(s_1, s_2). \quad (4.7)$$

The difference in energy from the improved wavefunction in Hartee-Fock compared to the Hartee approximation is called the exchange energy. Note however that Hartee-Fock is not a complete description either as it fails to model the electron correlations. For the next step we need to make use the variational principle. This is an efficient method for finding the ground state properties of a system. The method states that the energy of any trial wavefunction will always be higher than the ground-state energy E_0 , ie

$$E_0 = \langle \psi_0 | H | \psi_0 \rangle \leq \langle \psi | H | \psi \rangle = E. \quad (4.8)$$

This enables us to find the ground state energy and corresponding wavefunction by a minimization technique. We will apply the variational principle to find the ground state energy $\Psi_0(\mathbf{r}_1, \mathbf{r}_2)$ of a two electron Hartree problem. Here we skip the derivation and mechanism behind the variational principle and simply state the final product. In final, the Hartree single-electron equation is defined as

$$\left[-\frac{\hbar^2 \nabla^2}{2m_e} + V_H(\mathbf{r}) - V_{SI}(\mathbf{r}) + V_{ext}(\mathbf{r}) \right] \psi_j(\mathbf{r}) = \epsilon_j \psi_j(\mathbf{r}), j = 1, 2. \quad (4.9)$$

Furthermore the total energy can be calculated by

$$E = \sum_j \epsilon_j - \frac{1}{2} \int (V_H(\mathbf{r}) - V_{SI}(\mathbf{r})) n(\mathbf{r}) d\mathbf{r}. \quad (4.10)$$

In the above expressions V_H and V_{SI} are the Hartree potential and the self-interaction potential. The self-interaction potential is subtracted to account for that an electron can not interact with itself. The above statements can also be applied for Hartree-Fock systems and is easily extended to a N_E electron problem by setting j equal to $j = 1, 2, \dots, N_e$. In this case it's common to also include the self-interaction term to simplify the calculations by making the total potential equal for all electrons, however this introduces a self-interaction error in the approximation. Moreover, by employing the variational principle, the many body equation has been transformed to a set of single electron equations. The use of the variational principle means that this expression is valid only for the ground state of the system.

A second essential approximation to the many-body equation is the Born-Oppenheimer approximation. Given that the electron mass is negligibly small in comparison to that of a nuclei, we can treat the nuclei as point charges, enabling us to divide the eigenfunction into a separate electronic and nuclear part

$$\Psi_k^{en}(\mathbf{r}, \mathbf{R}) \approx \Psi_k(\mathbf{r}, \mathbf{R}) \cdot \Theta_k(\mathbf{R}), \quad (4.11)$$

In equation 4.11, $\Psi_k(\mathbf{r}, \mathbf{R})$ is the electronic part and $\Theta_k(\mathbf{R})$ the nuclear part. The \mathbf{R} dependence in $\Psi_k(\mathbf{r}, \mathbf{R})$ originates from the fact that electrons can respond instantaneously to updated positions of the nuclei. Writing this in terms of the Hamiltonian yields

$$(T_e + U_{ee} + U_{en}) \Psi_k(\mathbf{r}, \mathbf{R}) = E_k(\mathbf{R}) \Psi_k(\mathbf{r}, \mathbf{R}) \quad (4.12)$$

$$(T_n + U_{nn} + E_k(\mathbf{R})) \Theta(\mathbf{R}) = E_k^{en}(\mathbf{R}) \Theta_k(\mathbf{r}, \mathbf{R}). \quad (4.13)$$

We observe that the two sections are interrelated through the electronic energy $E_k(\mathbf{R})$. Furthermore, the left hand side of the nuclear part can be simplified to $U_{nn} + E_k(\mathbf{R})$, assuming that the kinetic energy of point charges is zero.

4.2 Kohn-Sham density functional theory

With the Hartree, Hartree-Fock and Born-Oppenheimer approximations we are finally ready to tackle the many-body Shrödinger equation. However, despite the aforementioned approximations one can apply, the many-body equation still pose a few obstacles to overcome both numerically and theoretically. The first of which is how the immense number of terms in equation 4.5 can be handled in a numerical manner. As an example, a material of volume equal to 1cm^3 contain about 10^{23} nucleus and electrons which makes for nearly 10^{40} terms to solve. A Second and more present concern is how the many-particle wavefunction

Ψ^{en} depend on the single-particle wavefunctions, and how we can operate the Hamiltonian on Ψ^{en} . This is where the density-functional theory enters. When people mention DFT today, most of the time they refer Kohn-Sham density functional theory, that combines the concept of the original density functional theory with the Kohn-Sham equation.

4.2.1 Density functional theory

The density functional theory was developed by Hohenberg and Kohn in 1964 and centers around the ground-state density of a system, expressed as

$$n_0(\mathbf{r}) = |\Psi_0(\mathbf{r})|^2. \quad (4.14)$$

The working principles of DFT is outlined in two theorems known as the Hohenberg-kohn theorems:

1. "All ground-state properties of the many-body system are determined by the ground state density $n_0(\mathbf{r})$. Each property is thus a functional $f[n]$ and the ground-state property is obtained from $f[n_0]$ ".
2. "There exists a variational principle for the energy density functional such that, if n is not the electron density of the ground-state, then $E[n_0] < E[n]$."

The first theorem states that the ground-state properties of a system can be determined uniquely from the ground-state density, thus the computational complexity of solving the many-body equation with $3N_e$ variables is reduced to a problem comprised of just 3 variables (x, y, z) from the density. While the second theorem provides a method of finding the ground-state density. The total energy of the system can thus be expressed as a functional of the density

$$E[n] = F[n] + \int V_{en}(\mathbf{r})n(\mathbf{r})d\mathbf{r}, \quad (4.15)$$

where $F[n] = T[n] + U_{ee}[n]$ make up the Hohenberg-Kohn functional and $\int V_{en}(\mathbf{r})n(\mathbf{r})d\mathbf{r} = U_{en}[n]$. Note that $F[n]$ is independent of the external potential, hence it is universal for all systems.

4.2.2 The Kohn-Sham Equation

The working principle of Kohn-sham density functional theory is to utilize the Kohn-Sham equation to determine the ground-state density, and then invoke the theorems of DFT to find the ground state energy. The Kohn-Sham approach begins by approximating the many-particle wavefunction by Hartree type functions

$$\Psi(\mathbf{r}_1, \mathbf{r}_2, \dots, \mathbf{r}_{N_e}) = \psi_1^{KS}(\mathbf{r}_1)\psi_2^{KS}(\mathbf{r}_2)\dots\psi_{N_e}^{KS}(\mathbf{r}_{N_e}), \quad (4.16)$$

where ψ_j^{KS} are auxiliary independent single-particle wavefunctions. This means that the density can be calculated as

$$n(\mathbf{r}) = \sum_{j=1}^{N_e} |\psi_j^{KS}(\mathbf{r})|^2. \quad (4.17)$$

The idea behind the Kohn-Sham equation is to now rewrite the energy expressed in equation 4.15 as

$$E[n] = T_s[n] + U_s[n] + U_{en}[n] + \left\{ (T[n] - T_s[n]) + (U_{ee}[n] - U_s[n]) \right\}, \quad (4.18)$$

with the "s" subscript relating to that the wavefunctions are the auxiliary single-particle wavefunctions, as described above. The enclosed term in equation (4.18) is known as the exchange-correlation energy E_{xc} of the system, defined as $E_{xc}[n] = \Delta T + \Delta U$. This quantity contains the leftover energy between the exact energy and the energy corresponding to the simpler terms $T_s[n] + U_s[n] + U_{en}[n]$. This means that the exchange-correlation must account for the more complex energies corresponding to the many-electron interaction, the self-interaction term, and a kinetic energy part. Thus, if E_{xc} is exact, so is the total energy. In full, we can write the energy functional as:

$$E[n] = \underbrace{\sum_j \int \psi_j^{KS*} \frac{-\hbar^2 \nabla^2}{2m} \psi_j^{KS} d\mathbf{r}}_{T_s[n]} + \underbrace{\frac{1}{2} \int \int q^2 \frac{n(\mathbf{r})n(\mathbf{r}')}{|\mathbf{r} - \mathbf{r}'|} d\mathbf{r} d\mathbf{r}'}_{U_s[n]} + \underbrace{\int V_{en}(\mathbf{r}n(\mathbf{r})) d\mathbf{r}}_{U_{en}[n]} + \underbrace{(T[n] - T_s[n]) + (U_{ee}[n] - U_s[n])}_{E_{xc}[n]}. \quad (4.19)$$

Analog to how we derived the single-particle Hartree equation, the single-particle Kohn-Sham equation can be derived with the variational principle to yield

$$\left\{ -\frac{\hbar^2}{2m_e} \nabla_s^2 + v_H(\mathbf{r}) + V_{en}(\mathbf{r}) + V_{xc}(\mathbf{r}) \right\} \psi_s^{KS}(\mathbf{r}) = \epsilon_s^{KS}(\mathbf{r}) \psi_s^{KS}(\mathbf{r}). \quad (4.20)$$

The ground-state density in equation 4.17 can now be calculated by solving the single-particle Kohn-Sham equation for all ground state single electron wavefunctions. Finally, we arrive at the total ground-state energy of the system

$$E[n] = \sum_j \epsilon_j^{KS} - \frac{1}{2} \int V_H(\mathbf{r}) n(\mathbf{r}) d\mathbf{r} + E_{xc}[n] - \int V_{xc}(\mathbf{r}) n(\mathbf{r}) d\mathbf{r}, \quad (4.21)$$

where $V_{xc}(\mathbf{r}) = \frac{\partial E_{xc}[n]}{\partial n}$ is the exchange-correlation potential. This is the Kohn-Sham density functional theory.

4.3 Limitations of DFT

Obviously, the biggest drawback of the density functional theory is that to this day we still don't have the exact form of the exchange-correlation energy. From the above derivations we recognize that this term must account for several complex properties, such as the many-body interaction and large amounts of kinetic energy. Additionally the exchange-correlation energy must also include the self-interaction error from applying Hartree-like wavefunctions in the Kohn-Sham equation. Furthermore, this functional should be applicable in any material, ie metals, semiconductors, liquids and gasses. In the next section we will look at some of the most commonly used approximations to E_{xc} . These approximate functionals range from low-complex and computationally cheap methods such as LDA, to heavy computational methods such as hybrid functionals. This is therefore seen as a disagreement between the theoretical philosophy of the DFT and the practical application of it, ie in practice one must adapt the functional first to the type of system and intention, for example if one wants to study the band gap, or weak Wan-Der Waals interactions. Secondly the functional must be chosen as a compromise between accuracy and cost.

However, even if the exchange-correlation functional was expressed exactly and efficiently implemented, DFT would still serve a couple of drawbacks. For instance the Kohn-Sham eigenfunctions in equations 4.17 are not the true single-electron eigenfunctions, thus also the corresponding eigenvalues are not exact even with an exact expression of E_{xc} . Meaning that the band gap obtained from the eigenvalues is in nature inexact. In fact, the estimation of the band gap of semiconductors is one of the major short-comings of DFT. In addition to the eigenvalue problem, the band gap is also subject to underestimation from a self-interaction term that over-delocalize the occupied states and hence pushes them up in energy, effectively reducing the band gap [30]. More advanced topics regarding the under-estimation of the band gap in semiconductors from DFT calculations can be read about in [31], by John P. Perdew and Mel Levy. Additionally, DFT also have difficulties in simulating weak long-range Wan-der Waal attraction [32], due to an emphasis on primarily the local density.

More practical limitations of DFT include factors such as the calculations not being variational with respect to the functional, meaning that a more complex functional does not guarantee higher accuracy [33]. Moreover the calculations of DFT only deliver a local minimum, in other words the calculations only return the most stable energy for the given initial settings and parameters. An example of this is when studying magnetic materials, where the total energy of a DFT calculation vary between each magnetic configuration of the material, meaning that to obtain the true ground-state energy one must perform an exhaustive search of all possible/probable magnetic orderings. Similar is also the case when comparing crystal structures and geometric features of materials. Finally, despite the possibility of simulations of excited states exists today, DFT in its original formulation is only valid for the ground state. Thus, these calcula-

tions has a lesser theoretical footing in comparison.

Nevertheless, DFT is still considered a widely successful method and accordingly Walter Kohn and John A. Pope won the Nobel prize in chemistry in 1998; "to Walter Kohn for his development of the density-functional theory and to John Pople for his development of computational methods in quantum chemistry." [34]

Part II

Method

Chapter 5

Practical aspects of DFT

5.1 The Exchange-Correlation functional

From the topics covered in chapter 4 we know that the missing piece of the density functional theory is the complex exchange-correlation energy $E_{xc}[n]$, that must account for all the simplifications and approximations employed in Kohn-Sham DFT. In this section we will explore some of the most commonly used approximations to the exchange-correlation functional that we apply in this project. Specifically, we will look at 4 levels of complexity: first is the local density approximation (LDA), followed by the generalized gradient approximation (GGA). These two are the least complex and most computationally affordable approximations to $E_{xc}[n]$. Next, are the meta-GGA functionals and finally the very accurate, but equally demanding hybrid-functionals.

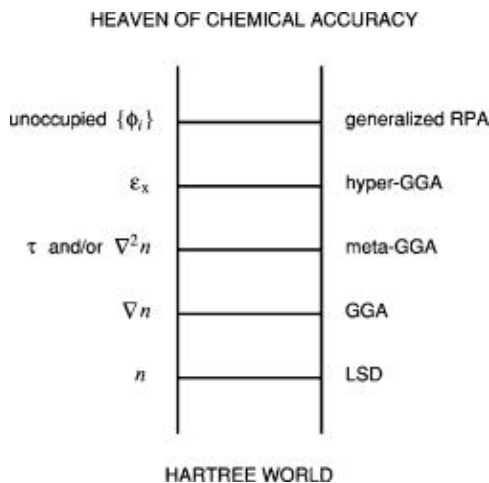


Figure 5.1: Jacob's ladder, developed by Perdew. Illustrating the relationship between accuracy and complexity of different exchange-correlation functionals. Figure from [35].

In addition, we have methods such as DFT+U, the Minnesota functionals, double hybrids and more, but these are outside the scope of this project. The different methods mentioned above of increasing complexity

and accuracy, are often referred to as steps in Jacob's ladder. This illustration/analogy of the different functionals was developed by Perdew [35], the ladder is illustrated in figure 5.1.

5.1.1 Local density approximation

A homogeneous electron gas (HEG) is the sole case we know of where the exchange-correlation functional can be determined exactly, because in this simple case the electron density is constant. The LDA works by setting the exchange-correlation potential $V_{XC}(\mathbf{r})$ at every position equal to that of the homogeneous electron gas [27], ie

$$V_{XC}(\mathbf{r}) = V_{XC}^{\text{HEG}}[n(\mathbf{r})]. \quad (5.1)$$

Obviously the LDA is of limited use given that a large part of what makes materials interesting is the variation in the electronic density [\cite{Sholl2009}]. For example, the LDA is well-known to both overestimate binding energies and underestimate the band gap of semiconductors and insulators. On the other hand, LDA generally provides adequate results of properties such as equilibrium distances and vibrational frequencies in bulk materials with slowly varying charge density. The biggest upside of LDA however, comes from the low computational cost, and was one of the first big success-stories with respect to practical applications of DFT.

5.1.2 Generalized gradient approximation

A natural succession to the local density approximation is the family of generalized gradient approximation (GGA) that also includes the gradient of the electron density

$$V_{XC}^{\text{GGA}}(\mathbf{r}) = V_{XC}[n(\mathbf{r}), \nabla n(\mathbf{r})]. \quad (5.2)$$

The ways one can implement the gradient are plenty-full and complicated. Two of the most common methods are the Perdew-Wang 91 (PW91) [36] and the Perdew-Burke-Ernzerhof (PBE) GGA [37]. This project will utilize the latter, which came to fruition in 1996 in an article by Perdew, Burke and Ernzerhof appropriately named "Generalized Gradient Approximation Made Simple". The key point regarding the PBE functional is that it's a non-empirical method thus providing reliable and adequate accuracy over a wide range of systems, as compared to for instance the BLYP functional that provides excellent accuracy of organic molecules but fails in other cases [38].

5.1.3 Meta-GGA

Meta-GGA functionals are the final level of complexity of the non-empirical approximations to the exchange-correlation functional. In addition to the constant density (LDA) and local gradient of the density (GGA), meta-GGA

methods consider the kinetic energy density of the occupied Kohn-Sham orbitals [39]

$$\tau_\omega = \sum_i^{\text{occ}} \frac{1}{2} |\nabla_{\psi_{i,\omega}}|^2. \quad (5.3)$$

The importance of this quantity on the band gap is well described in [40]. In this project we employ a meta-GGA functional named *Strongly Constrained Appropriately Normed*, or SCAN. This functional is the only known functional to satisfy all 17 known exact constraints of the XC functional [41]. There is indication of that the SCAN functional provides superior accuracy of energies and geometries, especially in diversely bonded structures [42], and of improved accuracy of band gaps and the electronic density of states compared GGA and LDA functionals [43]. On the other, it delivers overall less accurate band gaps compared to other meta-GGA functionals such as the *modified Becke-Johnson* [44]. Unfortunately, MBJ proved too difficult to converge for the particular materials in this project.

5.1.4 Hybrid functionals

The most accurate functional we employ in this project belongs to the family of *hybrid functionals*. This method consists of a hybrid between simpler functionals such as LDA, PBE or even meta-GGA and the exact treatment of exchange energy from Hartree-Fock, for example the global hybrid functional PBE0 [45] described as

$$E_{\text{xc}}^{\text{PBE0}} = (1 - \alpha) E_x^{\text{PBE}} + \alpha E_x^{\text{HF}} + E_c^{\text{PBE}}, \quad (5.4)$$

where α is the mixing parameter to decide the balance between the exchange energy, denoted x of Hartree-Fock with PBE. Similarly the last term represents the correlation energy from the PBE functional. This parameter α is determined empirically, thus this is a semi-empirical model. Heyd-Scuseria-Ernzerhof improved the accuracy of the model by separating the Coulomb interaction into long-range and short-range interaction by a function $\text{erfc}(\mu r)$. These are known as HSE functionals [46], one of the superior methods for accurate band gaps is the HSE06 hybrid functional [47], with $\alpha = 0.25$ and $\mu = 0.11$.

5.1.5 Outlook

In many cases LDA and GGA suffice, PBE especially is by most considered the conventional standard for DFT calculations, for its balance of accuracy, cost and wide range applicability. However, distinctly concerning the band gap of solids, both of these fall short. This is because the band gap of DFT calculations is complicated by the fact that the derivative of the XC-functional is discontinuous with respect to the electron concentration [48]. Thus, the simpler functionals fails to recall the experimental values since the total band gap in DFT is the fundamental gap (valence -

conduction) plus this contribution. This is corrected in meta-GGA and hybrid functionals in the generalized Kohn-Sham scheme. Lastly, we would like to refer the reader to the work of Borlido et al. who in 2019 conducted an exhaustive investigation of the band gap of over 470 unique compounds in order to benchmark the relative performance of several of the available and widely used XC-functionals [49]. In this large-scale project they found overwhelming confirmation that the HSE06 functional followed closely by Modified-Becke Johnson are the superior functionals for accurate band-gap calculations. Regarding the SCAN functional, in several cases this yielded outputs very comparable to MBJ, and produces much better formation energies than PBE, but tends to overestimate in magnetic alloys. On the other side, both LDA and PBE resulted in 50% and 30% underestimation of the band gap or in several cases miss-classified compounds as metals. This was particularly evident in materials consisting of Ni and other 3d elements.

5.2 Plane waves and reciprocal space

In this section, we will cover some of the practical factors that are important to consider when performing DFT calculations. The two most central topics are the energy cutoff parameter of plane waves, and the number of points in reciprocal space. More details on these parameters and relevant examples can be read about in [28].

The Shrödinger equation for a free electron has a simple analytic solution $\psi_k = Ae^{ikr}$. In a crystalline matter with a periodic potential $V(\mathbf{r}) = V(\mathbf{r} + \mathbf{R})$, the single-electron wavefunction takes the form

$$\psi_k(\mathbf{r}) = u_k(\mathbf{r})e^{ikr}, \quad (5.5)$$

where $u_k(\mathbf{r})$ is a Bloch wave with the periodicity of the crystal and e^{ikr} is called a plane wave. Because DFT apply plane waves as basis functions of the electronic density, DFT calculations are often referred to as plane wave calculations. The Bloch wave is the sum of all plane waves with wave vector equal to the reciprocal wave vector \mathbf{G} , described as

$$u_k(\mathbf{r}) = \sum_{\mathbf{G}} c_{\mathbf{G}} e^{i\mathbf{Gr}}, \quad (5.6)$$

which gives us the final expression for $\psi_k(\mathbf{r})$

$$\psi_k(\mathbf{r}) = \sum_{\mathbf{G}} c_{k+\mathbf{G}} e^{i(k+G)r} \quad (5.7)$$

Clearly, the infinite summation over all \mathbf{G} required to evaluate the wavefunction at a single point in reciprocal space is computationally unfeasible. In order to reduce this computational burden, we can introduce a maximum cutoff value of the energy E_{cut} . This is possible because equation 5.7 is the solution of the Shrödinger equation with corresponding kinetic energy

$$E = \frac{\hbar^2}{2m} |\mathbf{k} + \mathbf{G}|^2. \quad (5.8)$$

Assuming that the lower energy plane waves can represent the density adequately, we can limit the calculations to plane waves with energy less than E_{cut} :

$$E_{\text{cut}} = \frac{\hbar^2}{2m} G_{\text{cut}}. \quad (5.9)$$

Thus, we can reduce the infinitely large sum above to a much more feasible calculation

$$\psi_k(\mathbf{r}) = \sum_{|\mathbf{k} + \mathbf{G}| < G_{\text{cut}}} u_{\mathbf{k} + \mathbf{G}}(\mathbf{r}) e^{i(\mathbf{k} + \mathbf{G}) \cdot \mathbf{r}}. \quad (5.10)$$

The cutoff energy can be determined by performing a number of calculations with different cutoffs and observe the convergence with respect to the total energy and other relevant properties of the system. Another important parameter to specify in DFT calculations is the number of k-points. As seen in the above expression the wavevector k plays a big role in DFT. An other case that is more convinient to calculate in k-space is integrals of the form

$$g = \frac{V_{\text{cell}}}{(2\pi)^3} \int_{\text{BZ}} g(\mathbf{k}) d\mathbf{k}, \quad (5.11)$$

for instance the density of states. Note that "BZ" indicates that the integral is evaluated for all \mathbf{k} in the Brillouin zone. This integral can be approximated by evaluating it at a set of discrete k-points in reciprocal space and summing over the points with appropriately assigned weights. A larger set of points leads to more exact approximations. The method for selecting k-points in reciprocal space was developed by Monkhorst and Pack in 1976, where one specifies a number of points in each dimension $N_1 \times N_2 \times N_3$. Recalling that reciprocal space is inverse to regular space, supercells with equal and large dimensions converge at smaller values of N , and inversely for cells of small dimension. The total number of k-points required for converged calculations can be reduced by utilizing the symmetry of the cell, in which we can exactly approximate the entire BZ by extending a lesser zone through symmetry of the crystal lattice. This reduced zone is named the irreducible Brillouin zone (IBZ).

The required number of k-points for a given calculation can be found alike the cutoff energy by performing convergence tests with respect to the total energy of the system. Metals in particular require a large number of k-points because of discontinues integrals in the Brillouin zone around the Fermi surface where the states discontinuously change from occupied to non-occupied. To reduce the cost of this operation, there are two primary methods: efficient sampling with the tetrahedron method, and smearing. The idea behind the tetrahedron method is to use a discrete set of k-points to fill the reciprocal space with tetrahedra and interpolate the function within each tetrahedron such that the function can be integrated in the entire space rather than at discrete points. The latter approach for solving

discontinuous integrals is to smear out the discontinuity at the Fermi level and thus transforming the integral to a continuous one. A good analogy to this method is the Fermi-Dirac function, in which a small variable σ transforms a step-function into a continuous function that can be integrated by standard methods.

A final consideration to how DFT is applied in practice is how the core electrons are handled. Tightly bound core electrons as opposed to valence electrons, demand a greater number of plane-waves to converge. The most efficient method of reducing the expenses of core-electrons are so-called pseudopotentials. This method works by approximating the electron density of the core electrons by a fixed density that mimics the properties of true ion core and core electrons. This density is then fixed for all subsequent calculations, in other words only considering the valence electrons while regarding the core electrons as frozen in. Two very popular pseudopotentials used in DFT are currently so-called ultrasoft pseudopotentials (USPPs) developed by Vanderbilt, and the projector augmented-wave (PAW) method by Blöchl [50], [51].

5.3 Self-consistent field calculation

Preceding this section, we have looked at the fundamental theory of DFT and its practical ability to model various materials. In Figure 5.2, we illustrate the self-consistent field calculation scheme for how DFT calculations are performed in practice. The initial problem posed by DFT is that all properties rely on the density, and are thus dependent on each other. For instance, the effective potential is dependent on the density, which again is dependent on the eigenfunctions, that rely on the effective potential again. The clever approach begins with an initial guess to the density from which we can solve the Kohn-Sham equations and obtain the corresponding eigenfunctions. Following is an iterative method where we apply the recently calculated eigenfunctions to determine a new density and repeat the procedure above. This is repeated until the total energy is converged, by an own-defined criterion. Equivalently, the optimal ionic positions can be found by a similar approach. This method is based on quasi-Newton algorithms to minimize the forces between ions.

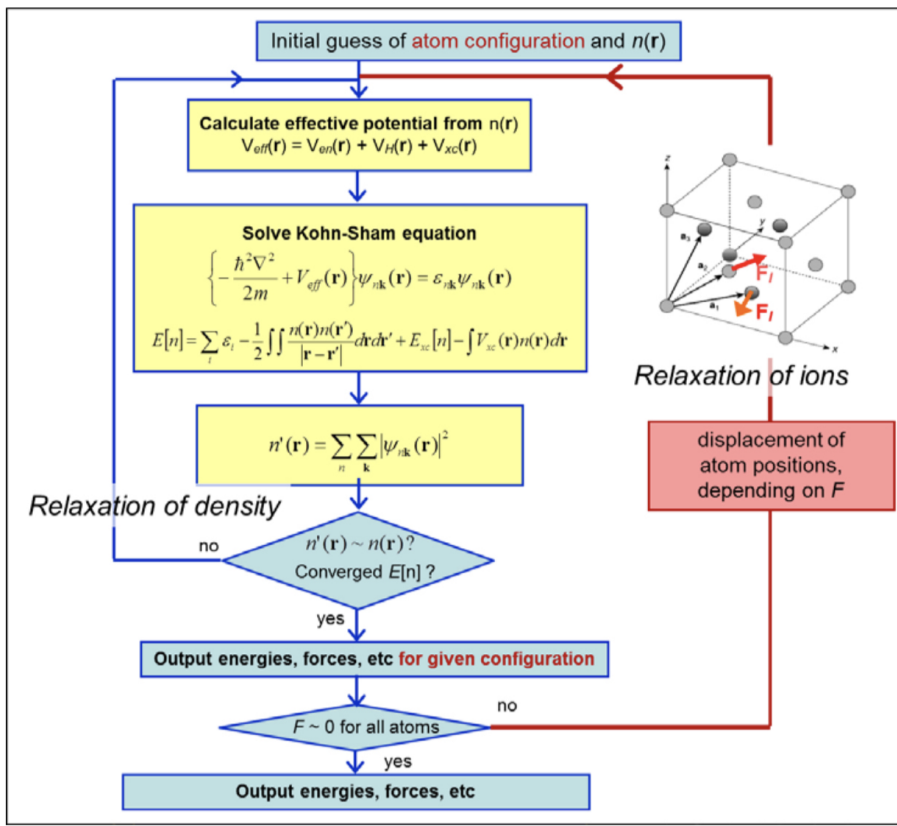


Figure 5.2: Flow chart of the self-consistent field calculation scheme of DFT calculations. Figure adopted from the lecture notes of the course FYS-MENA4111 at the University of Oslo [27].

Chapter 6

Computational details

6.1 Settings and dependencies

The computations were performed on resources provided by Sigma2 - the National Infrastructure for High Performance Computing and Data Storage in Norway, utilizing the Vienna Ab initio Simulation Package (VASP) [52], [53], [54], [55]. As discussed in chapter 5, we employ the projector-augmented-wave method and PBE GGA, in addition to SCAN and HSE06 in certain instances. For the structures studied in this project, we found an energy cutoff of 300 eV and 400 eV suitable for electronic and geometric relaxations respectively. In regards to the number of k-points, we used a gamma centered mesh with a density of 4 per \AA^{-1} . The convergence of these parameters with respect to the total energy can be seen in table 6.1. The convergence tests were conducted for a 48-atom supercell of a $\text{Cr}_4\text{Fe}_4\text{Mn}_4\text{Ni}_4\text{Si}_{32}$ alloy, that is representative for all alloys studied in this project. From table 6.1 we see that the cutoff energy could be increased further for optimal convergence, however to spare computational resources we opt for the lower value. Nevertheless, between 300 eV and 350 eV, the total energy only alters by 3 meV, which is around the limits of computational accuracy of VASP calculations.

The geometric relaxation of ionic positions and cell volume was carried out in two subsequent runs with convergence criterion of 1×10^{-2} eV/ \AA for the forces and 1×10^{-5} eV for the total energy, with Gaussian smearing (ISMEAR = 0 in VASP) and smearing width σ equal to 0.05 eV. After successful geometric relaxation, the structures underwent a final electronic relaxation with the tetrahedron method with Blöch corrections (TBC, ISMEAR = -5 in VASP), and energy criterion of 1×10^{-6} eV between consecutive Kohn-Sham iterations. Calculations with the HSE06 functional in many instances proved difficult to converge electronically. This was solved by two measures: firstly we reduced the density of k-points from 4 \AA^{-1} to 2 per \AA^{-1} . Secondly, we found that HSE06 computations converged much quicker with Gaussian smearing compared to the tetrahedron method. Thus, in order to successfully and economically carry out calculations with HSE06 and the tetrahedron method, we first calculated the charge density with Gaussian smearing and reapplied the

calculated density in a subsequent HSE06 calculation with the tetrahedron method. Magnetic materials consisting of ferromagnetic elements such as iron, nickel and cobalt, were handled with the setting ISPIN = 2 and the default value of MAGMOM = NIONS * 1.0 in VASP, which specifies the initial magnetic moment for each atom. Further customization and testing of magnetic orderings such as antiferromagnetic, ferrimagnetic and ferromagnetic were considered beyond the scope of this project.

The SQS method was implemented through the generate – structure script in the Temperature dependent effective potential (TDEP) package [56], developed by Hellman and Shulumba. The CIF-file of β -FeSi₂ that we used to build are alloys were obtained from Materials Project [57]. Furthermore, Materials Project was used to compare and measure the validity of calculations. To extract and post-process the VASP calculated data, we relied on both VASPKIT [58] and pymatgen [59].

Cutoff energy (eV)	Total energy (eV)	K-points (per Å ⁻¹)	Total energy (eV)
200	-6.444		
250	-6.568	3	-6.584
300	-6.586	4	-6.586
350	-6.589	5	-6.586
400	-6.588	6	-6.586
450	-6.589		

Table 6.1: Convergence tests of the cutoff energy and density of k-points, with respect to the total energy. The tests were conducted for a 48-atom supercell of Cr₄Fe₄Mn₄Ni₄Si₃₂.

6.2 Material

In this project we have constructed high-entropy silicides based on the β -FeSi₂ compound. The unit cell of this material adopts the orthorhombic CMCE space group, and consists of 16 iron atoms and 32 silicon atoms. For each composition, we generate five distinct SQSs of equivalent geometry and composition, that only vary by the atomic configuration. We have emphasized a particular composition of the 3d elements Cr, Fe, Mn, and Ni in a Cr₄Fe₄Mn₄Ni₄Si₃₂ alloy, where the 3d elements are distributed equimolarly over the Fe-sites in the β -FeSi₂ crystal structure. These SQSs can be seen in figure 6.1. In addition to the (CrFeMnNi)Si₂ composition, we have tested alternative compositions with varying distributions of 3d elements and different elements. These supercells has been generated by an identical procedure and remain consistent with the 48 atom SQS model.

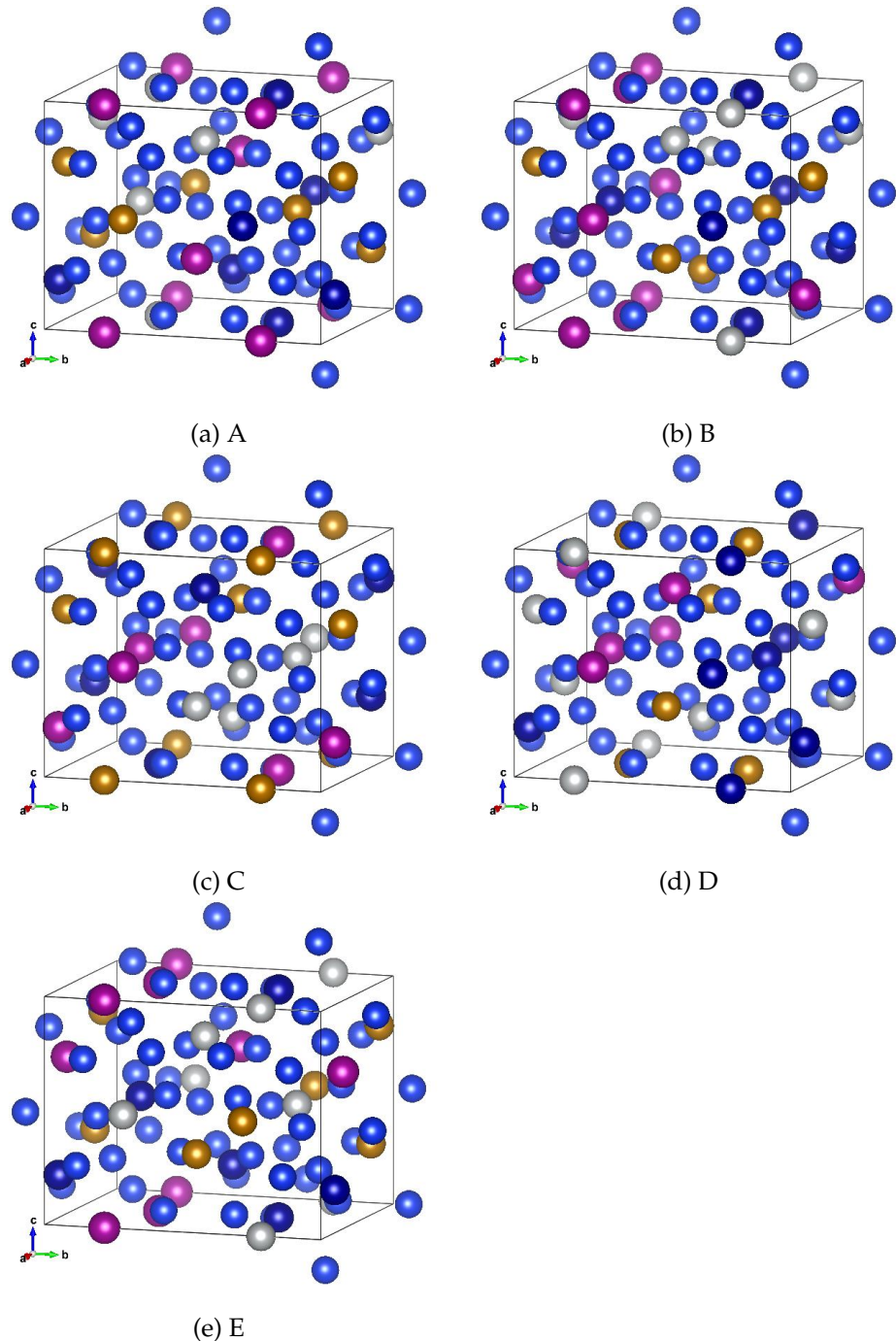


Figure 6.1: Five distinct 48-atom SQSs of $\text{Cr}_4\text{Fe}_4\text{Mn}_4\text{Ni}_4\text{Si}_{32}$ based on the $\beta-\text{FeSi}_2$ crystal structure. Manganese atoms are represented as purple spheres, chromium as dark blue and silicon as light blue, followed by iron and nickel presented as gold and silver spheres respectively. The respective SQSs are denoted as A, B, C, D and E. Figures illustrated with VESTA [60]

Part III

Results and Discussion

Chapter 7

The high-entropy silicide $(\text{CrFeMnNi})\text{Si}_2$

7.1 $\beta\text{-FeSi}_2$

We begin with a brief overview of the master compound $\beta\text{-FeSi}_2$ that we have used as a foundation for the alloys in this project. In addition this is the sole case where our methods and results can be compared to experimental work and relevant literature.

$\beta\text{-FeSi}_2$ is a well known semiconductor with an experimentally measured band gap of around 0.85 eV at room temperature [61]. The nature of the band gap is under debate, although most ab initio studies result in an indirect gap, experimental studies agree on a direct band gap. From our own calculations we get an indirect band gap of 0.65 eV with the PBE GGA functional. In comparison, Materials Project lists a band gap of 0.70 eV with the same functional. This slight discrepancy is most likely down to use of different parameters in the calculations, for instance Materials project use a different pseudopotential with more valence electrons, and a larger cutoff energy of 520 eV. In agreement with Materials Project our calculations return a final magnetic moment of the compound equal to 0. This can be seen in the electronic density of states plotted in figure 7.1, by that the DOS and hence band gap are identical in both spin directions.

The formation energy E_{form} of the compound can be calculated as the difference in total energy between the product and the sum of reactants. For the FeSi_2 compound that consist of 16 iron atoms and 32 silicon we get

$$E_{\text{form}} = -327.72\text{eV} - (16 \times -8.32\text{eV} + 32 \times -5.42\text{eV}) = -21.16\text{eV},$$

or formation energy per atom $E_{FPA} = 0.441\text{eV}$ from $-21.16/48$. The total energy of iron and silicon were calculated separately for the respective base elements with identical parameters as used for the FeSi_2 calculation. The total energies correspond well with the listed energies from materials project of -8.4693 eV and -5.4234 eV for Fe, and Si respectively. Accordingly, the formation energy per atom for $\beta\text{-FeSi}_2$ of 0.441 eV is in good agreement with materials project's value of 0.444 eV.

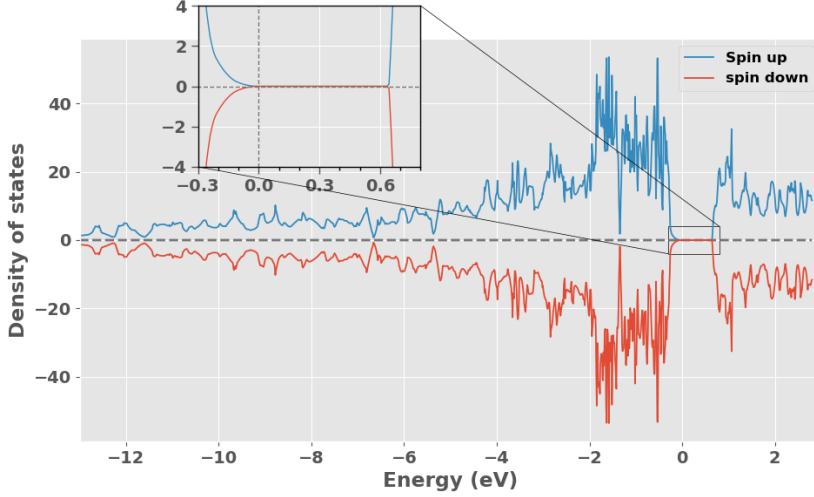


Figure 7.1: Density of states [states/eV] of $\beta\text{-FeSi}_2$

7.2 $(\text{CrFeMnNi})\text{Si}_2$

The first alloy we will look at is the equimolar distribution of Cr, Fe, Mn and Ni. For details on this alloy, and a visualization of the supercells we refer the reader to section 6.2. Below in table 7.1 we list the total energy per atom, final magnetic moment per atom, and band gap of five distinct SQSs of the $\text{Cr}_4\text{Fe}_4\text{Mn}_4\text{Ni}_4\text{Si}_{32}$ alloy. In addition we include the mean and standard deviation (std) between the 5 supercells and the formation energy calculated from the mean total energy.

SQS	Toten (eV)	Mag (μ_B)	E_G (eV)
A	-6.608	0.083	0.028
B	-6.614	0.083	0.052
C	-6.606	0.083	0.034
D	-6.616	0.083	0
E	-6.609	0.083	0.050
Mean	-6.611	0.083	0.033
Std	0.004	0.000	0.021
E_{FPA} (eV)	-0.293	-	-

Table 7.1: Total energy per atom (Toten), final magnetic moment per atom (Mag), band gap (E_G) and formation energy (E_{FPA}) of 5 SQS of $(\text{CrFeMnNi})\text{Si}_2$.

From table 7.1 we observe that the total energy and magnetic moment are quite similar in all 5 supercells, which could be expected from that the only variable between supercells is the atomic configuration. On the other hand, the atomic configuration has a larger impact on the band gap of the

supercells. We find that the band gap ranges from a maximum value of 0.05 eV in SQS B, to a metal in SQS D, nevertheless much smaller than the band gap of 0.65 eV in FeSi₂. We will come back to the band gaps in section 7.2.1.

Contrary to the master compound, these supercells representing the (CrFeMnNi)Si₂ alloy contains a finite magnetic moment of around 0.083 μ_B . However, compared to a ferromagnet such as iron, with Mag = 2.2 μ_B according to Materials Project, we note that this is not a strong ferromagnetic material. In contrast to the high-entropy alloys discussed in section 2.2, we observe common for all supercells that the largest local magnetic moments are ascribed to chromium and manganese atoms in the lattice, while on the other hand both iron and nickel atoms within the numerical accuracy of the calculations, accounts for negligible contributions to the magnetic moment. Considering that the magnetic moment is identical across all five distinct atomic configurations, in addition to that the local magnetic moments displays very similar trends between supercells, the observed magnetism is probably connected to the specific crystal structure. It should be noted however that the magnetic properties in this project could be prone to errors. As we discussed in section 4.3, one of the major drawbacks of DFT in regards to magnetic materials is the local minima problem. In this project we have overlooked this concern, and applied a constant initial magnetic configuration to all structures, disregarding for example antiferromagnetic or possible permutations of ferrimagnetic orderings, to reduce the workload. Thus, its possible that the final magnetic structure of the supercells adopts local minima rather than global. Coupling this with the possible errors associated with the special quasi-random structures method to model the disordered magnetic structure means that the magnetic results and following the total energy and corresponding stability are not immutable nor necessarily accurate in respect to the hypothetical real alloy.

In terms of the total energy the most and least stable SQSs are "D" and "A" respectively, meaning that SQS D is then the most representative configuration of the real material. However, most likely all five SQSs and other possible configurations would appear as local orderings in domains of the real material with a certain probability. Therefore we will consider and discuss the results of all 5 SQSs as well as the most stable supercell. Further, the total energy alone is not sufficient to evaluate the stability of the structure. In this project we have not considered factors such as the configurational entropy or made any finite temperature considerations. Additionally, the discussion above on the magnetic configuration could affect the total energy. Thus, the relative stability between supercells listed in table 7.1 could change. Nevertheless, we put the most effort into analyzing the most stable supercells of each alloy, as according to the considerations made in this project, are the most representative configurations of the real material.

7.2.1 The band gap

As seen from table 7.1, the band gap of the alloy is severely reduced from the master compound, and varies between supercell to supercell. We observed a maximum band gap of 0.05 eV in SQS B, and on the flip side a 0 band gap in the most stable configuration, SQS D. The density of states of SQS D and B are displayed in figures 7.2 and 7.3 below.

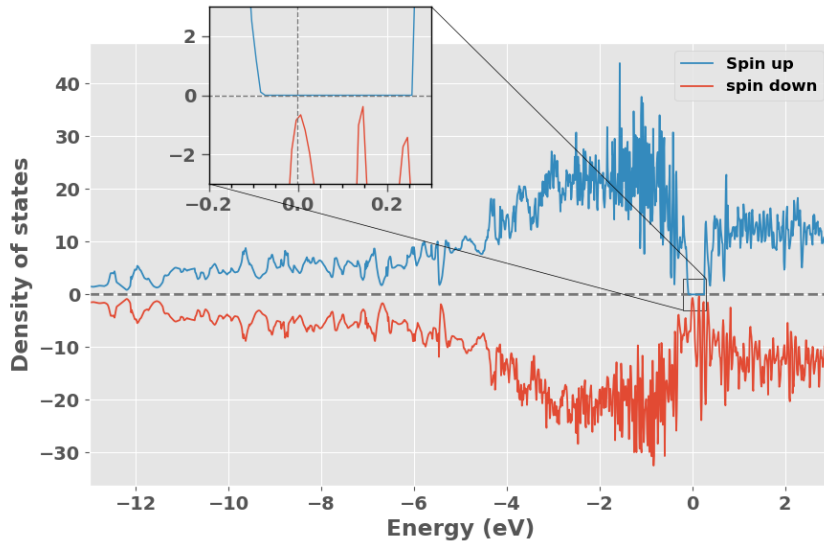


Figure 7.2: Density of states [states/eV] of SQS D of $(\text{CrFeMnNi})\text{Si}_2$.

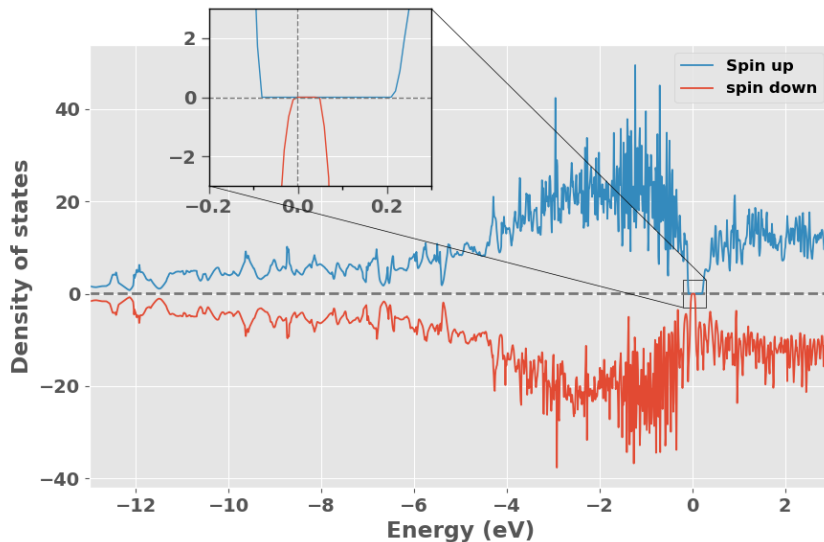


Figure 7.3: Density of states [states/eV] of SQS B of $(\text{CrFeMnNi})\text{Si}_2$.

In figure 7.2 and 7.3 we observe that the band gap in both SQS D and B, in accordance with the magnetic property differ between the spin

directions. Going forward we will refer to the band gap in spin up as E_G^{up} , and spin down as E_G^{dw} . Clearly in both D and B $E_G^{\text{up}} \gg E_G^{\text{dw}}$ as SQS D for instance exhibits a band gap of around 0.3 eV in spin up, contrary to a 0 in spin down. Comparing to the values in table 7.1 we find that the total band gaps of the respective structures are limited by the narrow or nonexistent band gap in spin down.

To obtain further and more precise information on the band gap we look to the calculated Kohn-Sham eigenvalues. The band gaps found from investigating the eigenvalues, denoted as E_G^{eigen} can be seen below in table 7.2 for all five SQS.

SQS	$E_G^{\text{up, eigen}}$ (eV)	$E_G^{\text{dw, eigen}}$ (eV)	$E_G^{\text{tot, eigen}}$ (eV)
A	0.081	0.052	0.028
B	0.293	0.052	0.052
C	0.236	0.034	0.034
D	0.340	0	0
E	0.310	0.050	0.050

Table 7.2: Band gap of five SQSs of $(\text{CrFeMnNi})\text{Si}_2$ in spin up, spin down and total. The band gaps are calculated from the Kohn-Sham eigenvalues of PBE simulations.

Continuing the trend described above we observe equivalent to SQS D and B that $E_G^{\text{up}} \gg E_G^{\text{dw}}$ for all supercells, par SQS A. In this supercell the spin polarization of the band gap is dampened, despite the supercell being equally magnetic to the other supercells. Moreover, in this case the total band gap $E_G^{\text{tot}} = E_G^{\text{up}} - E_G^{\text{dw}}$, as opposed to the other supercells where the total band gap is equal to the lesser spin down band gap of the structure. This can be seen in the density of states in figure 7.4. DOS plots of SQS C and E can be seen in appendix A.1, note that in SQS C we were required to increase the number of points to calculate the density of states (NEDOS in VASP) in order to observe the band gap.

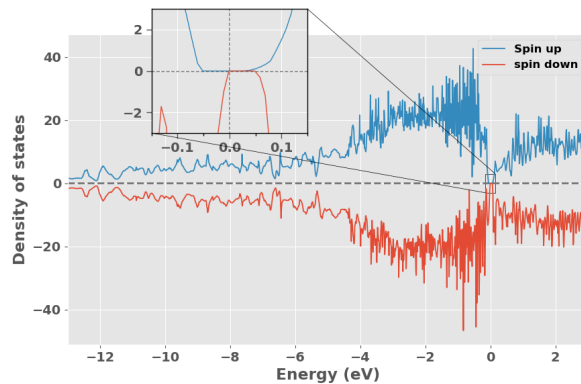


Figure 7.4: Density of states [states/eV] of SQS A of $(\text{CrFeMnNi})\text{Si}_2$.

In VASP the energy eigenvalues are listed for every energy band at all k-points used in the calculation, with corresponding occupancy. An occupancy of 1 represents a fully occupied eigenstate, while a completely unoccupied (empty) eigenstate has occupancy equal to 0. We Recall that occupied states belong to the valence band, and the conduction band consists of unoccupied states (at 0 K). The highest energy valence band in these structures are band 124 in spin down and 128 in spin up, following the lowest energy valence band is 125/129 in spin down/up. The band gap in spin down is then determined from the difference between the lowest energy eigenvalue in band 125 and the highest energy eigenvalue in band 124, and likewise for the spin up band gap between bands 128 and 129. In SQS D different from the semiconducting structures we observe some partially occupied states at the band edges in bands 124 and 125 in spin down. With partially occupied states we refer to eigenstates in the valence band with occupancy less than 1 and states in the conduction band with occupancy above 0. Specifically, the highest energy eigenvalue (9.01 eV) in band 124 has occupancy equal to 0.94, and equivalently the lowest energy eigenvalue (8.98 eV) in band 125 has occupancy equal to 0.08. This results in a zero band gap. The Fermi energy of this structure is 8.99 eV, which means that the partially occupied eigenstate in band 124 is above the Fermi energy, and the partially unoccupied eigenstate in the conduction band below the Fermi energy. This is a clear indication of a metal, in which the conduction band and valence band overlap. In this project we will refer to such eigenstates with partial occupancy as defect states. The effect of the defect states on the band gap of SQS D can be seen in table 7.3. Here we calculate the band gap as a function of the defect states by an occupancy cutoff parameter occ , such that $E_G(0.99, 0.01)$ is the band gap when only including eigenvalues with occupancy above 0.99 in the valence band and below 0.01 in the conduction band. For simplicity we will write this parameter as a single value, where $occ = 0.01$ represents occupancy equal to 1 - 0.01 in the valence band and 0 + 0.01 in the conduction band.

occ	$E_G^{\text{up, eigen}}$ (eV)	$E_G^{\text{dw, eigen}}$ (eV)	$E_G^{\text{tot, eigen}}$ (eV)
0.5	0.340	0	0
0.05	0.340	0.021	0.021
0.01	0.340	0.050	0.050
0.001	0.340	0.073	0.073
<0.0001	0.340	0.086	0.086

Table 7.3: Band gap of SQS D of (CrFeMnNi)Si₂ as a function of occupancy cutoff occ in the eigenvalues.

From table 7.3 we find clear evidence of the defect states prohibiting the band gap in spin down in SQS D, compared to the semiconducting supercells that contain only fully occupied and unoccupied eigenstates. To investigate this effect to greater extent we compare the eigenvalues of

SQS D to a pure metal, such as iron. In this case the energy bands (both spins) around the Fermi energy (5.8 eV) are populated mostly by partially filled eigenstates. Inside a single energy band we observe instances of both more than half-filled states above E_F , and less than half-filled states above E_F , thus a clear overlap between the conduction and valence band. In contrast we find no instances of partial occupants in pure Si, as in the semiconducting SQSs. Therefore we can firmly state that the "defect states" are associated with a metallic character. Compared to the pure metal however, the amount and severity of the partial occupants are very dampened in SQS D. The concept of defect or impurity states in the band gap has been found as a common feature of the band structure of random alloys [62], however we have reservations about if this is a physical result or related to numerical factors. In addition to partial occupants in Fe and SQS D we observe a plural of unphysical states where the occupancy exceeds 1 and 0. Recalling that the discontinuous Fermi surface of metals poses several obstacles on DFT calculations with respect to the smearing and number of k-points. This result could then be imagined as a consequence of numerical methods. For instance in SQS B we conducted three separate electronic calculations, one with the tetrahedron method (value listed in tables) and two calculations with Gaussian smearing with smearing width 0.05 and 0.005 eV. With the Gaussian method and smearing width $\sigma = 0.05\text{eV}$ we get $E_G^{\text{up, eigen}} = 0.299\text{eV}$ and $E_G^{\text{dw, eigen}} = 0.050\text{eV}$. Further calculations with the Gaussian method with smearing width of 0.005 eV results in $E_G^{\text{up, eigen}} = 0.293\text{eV}$ and $E_G^{\text{dw, eigen}} = 0.052\text{eV}$. Compared to the values in table 7.3 with TBC, we observe that Gaussian (0.005 eV) and TBC are identical, while Gaussian (0.05 eV) show some deviation. Furthermore we find that the eigenvalues of Gaussian 0.05 eV contain defect states, and that the spin down band gap, as we experienced for SQS D, can be enlarged from $E_G^{\text{dw, eigen}}(0.01) = 0.170\text{eV}$. However, in this case we find no instances of non-naturalistic states as we described above for SQS D with TBC.

In conclusion, the defect states observed in SQS D appear to be related to a metallic structure, however from the discussion above we have seen that the results could be subject to numerical factors as well. It would have been instructive to visualize and analyze the eigenvalues by plotting the band structure. Unfortunately this is neither simple to perform or interpret for large supercells consisting of several elements and a large number of energy bands. One solution could be band-unfolding, but this did not work in conjunction with the implementation of the SQS method in this project.

7.2.2 Local and projected density of states

In this section we will analyze the local and projected density of states of primarily SQS D (most stable). Below we include the local density of states of silicon in figure 7.5, and the respective LDOS plots of the various 3d elements of the compound in figure 7.6.

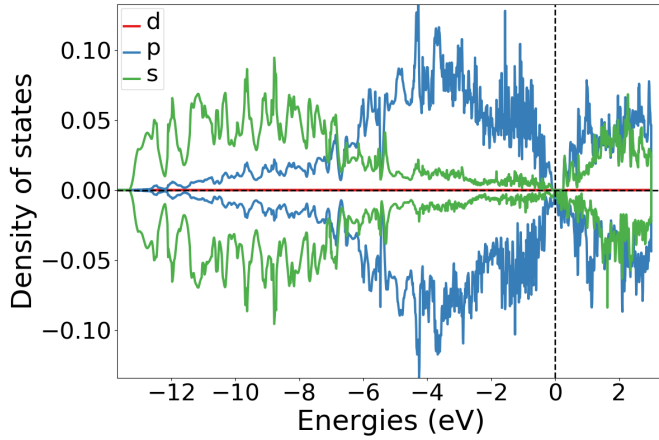


Figure 7.5: Local density of states [states/eV] of Si, in SQS D of $(\text{CrFeMnNi})\text{Si}_2$.

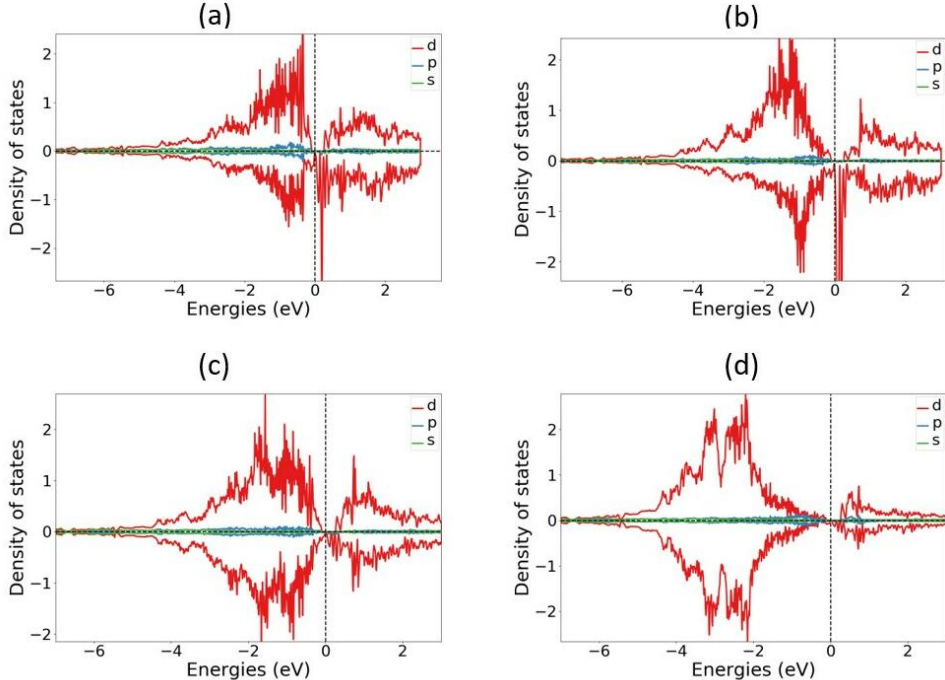


Figure 7.6: Local density of states [states/eV] of (a) Cr, (b) Mn, (c) Fe, (d) Ni in SQS D of $(\text{CrFeMnNi})\text{Si}_2$.

In the local density of states of Si we see that the s-electrons in Si occupy states in the lower energy regions and p electrons at slightly elevated energies closer to the Fermi energy. Above E_F states are occupied by s and p electrons equally. Between the 3d electrons of the transition metals, markedly manganese and chromium display a strong presence at energies just above E_F and manganese additionally below E_F . Iron and Nickel show largest contributions at energies further from the Fermi energy, most notably below E_F . In the spin up channel we see a similar trend where

chromium lie closest to E_F followed by manganese, iron and lastly nickel at the lowest energies. The interplay between the 3d elements and silicon can be seen from the projected density of states in figure 7.7.

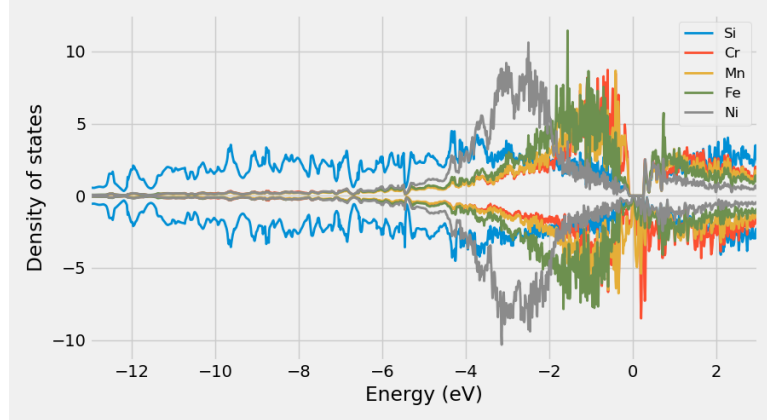


Figure 7.7: Projected density of states [states/eV] of SQS D of $(\text{CrFeMnNi})\text{Si}_2$

Compared to bulk $\beta\text{-FeSi}_2$ [63], we observe good agreement of the local DOS of Fe and Si in this alloy. Moreover the relative positions are in good agreement with observed trends in simpler Si-rich 3d transition metal silicides [64]. In these compounds, the electronic structure tends to be dominated by d electrons, and the valence band density of states are filled by d states near E_F . The p-d hybridization between Si and TM elements is typically found at about 6 eV below E_F , and Si s states about 10 eV below. In our alloy we observe good agreement of s-electrons as seen in the local density of states in figure 7.5, but the p electrons are pushed up in energy closer to E_F .

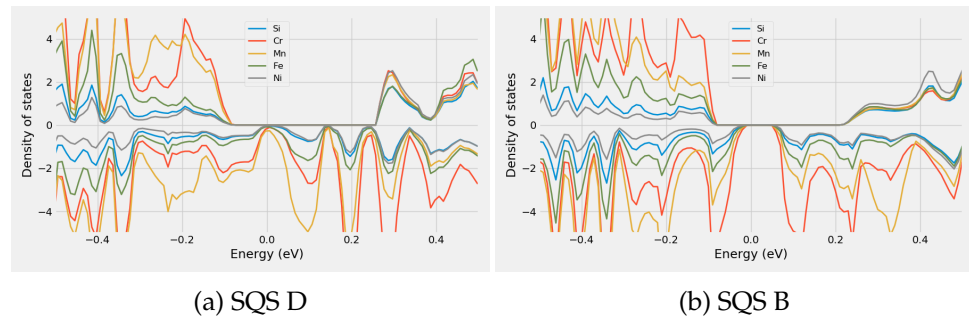


Figure 7.8: Projected density of states [states/eV] of SQS D and B of $(\text{CrFeMnNi})\text{Si}_2$ around the Fermi energy.

In figure 7.8 above we have plotted the projected DOS of the half-metallic structure (SQS D) and the configuration with the largest E_G^{dw} (SQS B) around the Fermi energy. Compared to the semiconducting structure we can distinctly observe a large number of Mn states in SQS D around E_F , most noticeably in spin down, but also in spin up. The projected density

of states of SQSs A, B, and E are included in appendix A.2 (unable to plot PDOS for SQS C).

7.2.3 The band gap of $(\text{CrFeMnNi})\text{Si}_2$ with SCAN and HSE06

As expressed previously, in this work we invoke 3 steps of Jacob's ladder: GGA (PBE), meta-GGA (SCAN) and hybrid functional (HSE06), to determine the band gap. The outcome of these 3 functionals are showcased in table 7.4.

SQS	XC-functional	E_G^{up} (eV)	E_G^{dw} (eV)	E_G^{tot} (eV)
A	PBE	0.082	0.052	0.028
	SCAN	0	0	0
	HSE06	0.708	0.026	0.026
B	PBE	0.293	0.052	0.052
	SCAN	0.147	0.089	0.089
	HSE06	0.286	0.182	0.182
C	PBE	0.236	0.034	0.034
	SCAN	0.069	0.112	0.112
	HSE06	0.174	0.033	0.020
D	PBE	0.339	0	0
	SCAN	0	0.108	0
	HSE06	0.378	0	0
E	PBE	0.308	0.050	0.050
	SCAN	0.154	0.111	0.105
	HSE06	0.548	0.013	0.013

Table 7.4: Band gaps of five supercells of $(\text{CrFeMnNi})\text{Si}_2$ in spin up, spin down and total, calculated with PBE, SCAN and HSE06 functionals.

We will begin dissecting table 7.4 by comparing SCAN to PBE. The first distinction we make notice of is in SQS A. Here calculations with the SCAN functional predicts a metallic compound, contrary to the the PBE band gap of 0.03 eV. Alike the band gap of SQS D discussed previously, the 0 band gap in this structure with SCAN is caused by defect states. Neglecting such states and evaluating the band gap from exclusively almost completely filled and empty eigenstates yield $E_{G, \text{SCAN}}^{\text{up,eigen}}(0.01) = 0.032$ eV and $E_{G, \text{SCAN}}^{\text{dw,eigen}}(0.01) = 0.053$ eV, and a total band gap of 0.032 eV. This value seems to agree better with the PBE band gap of this supercell, but we observe that E_G^{up} is larger in PBE. This is a recurrent pattern with SCAN across all five SQSs, where $E_{G, \text{SCAN}}^{\text{up}} < E_{G, \text{PBE}}^{\text{up}}$, and moreover $E_{G, \text{SCAN}}^{\text{dw}} > E_{G, \text{PBE}}^{\text{dw}}$. This can be seen in figure 7.9, where we plot the density of states of SQS E (a, b) and C (c, d). Note that the SCAN band gap in SQS C has the opposite spin polarization of PBE; this is also the case in SQS D,

as seen in table 7.4.

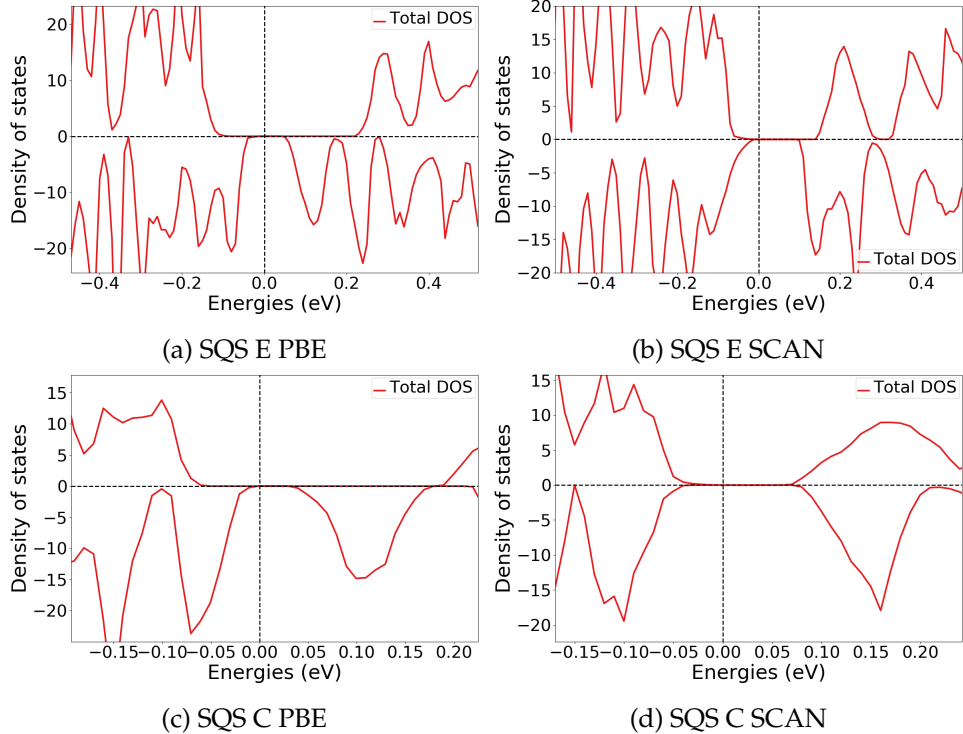


Figure 7.9: Density of states [states/eV] illustrating the difference between band gaps of SQS E and D of (CrFeMnNi)Si₂ with PBE and SCAN.

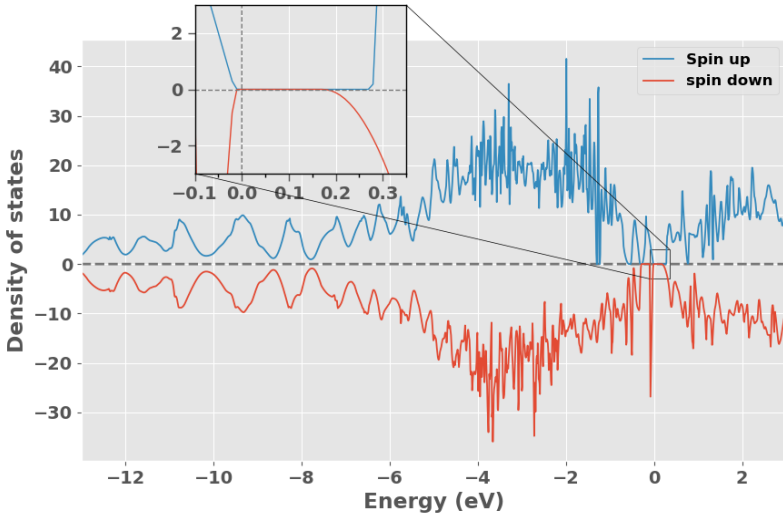


Figure 7.10: Density of states [states/eV] of SQS B of (CrFeMnNi)Si₂ with HSE06.

With the HSE06 functional we observe the opposite trend in SQS A and E compared to SCAN, here $E_{G, \text{HSE06}}^{\text{up}} > E_{G, \text{PBE}}^{\text{up}}$ and $E_{G, \text{HSE06}}^{\text{dw}} < E_{G, \text{PBE}}^{\text{dw}}$. But

in other cases $E_{G, HSE06}^{up}$ is lesser (SQS C) or similar to PBE (SQS B and D). On the other hand $E_{G, HSE06}^{dw}$ is consistently smaller in all structures compared to PBE, with the exception of SQS B. In this structure the HSE06 functional predicts large band gaps in both spin directions, this can be seen in the density of states plotted in figure 7.10 above.

As we discussed in section 5.1, hybrid functionals are much more computationally demanding compared to both meta-GGA and GGA functionals. In this project we experienced particular difficulty of converging calculations with HSE06 of the compositionally complex SQSs. To reduce the cost of the HSE06 functional we performed such calculations with a lower density of k-points, see section 6.1. The small amount of k-points could as discussed lead to numerical inaccuracies relating to the calculation of the Fermi surface in metallic structures. Furthermore, the reduced mesh of k-points could result in artificially exaggerated band gaps from failing to encapsulate the exact minimum transition between the valence band and conduction band.

XC-functional	Transition (k-point)
PBE	$(1/4, 0, 1/4) \rightarrow (0, 0, 0)$
SCAN	$(1/4, 0, 1/4) \rightarrow (0, 1/3, 0)$
HSE06	$(1/2, 0, 0) \rightarrow (0, 0, 0)$

Table 7.5: Minimum gap between k-point in valence band and conduction band in SQS B of $(\text{CrFeMnNi})\text{Si}_2$ from PBE, SCAN and HSE06 simulations.

In table 7.5 we list the transition between the highest occupied k-state in the valence band and lowest unoccupied k-state in the conduction band for SQS B with PBE, SCAN and HSE06 respectively. We observe that all 3 functionals find different k-point transitions. A concerning factor is that the highest energy k-point in the valence band from PBE calculations $(1/4, 0, 1/4)$ is not included in the HSE06 calculation with the narrow mesh of $2 \times 2 \times 2$ k-points. Thus, one may suspect that the HSE06 calculation overlooks the minimum transition and hence returns an enlarged band gap instead. This could be the case in $E_{G, A}^{up}$ and $E_{G, B}^{dw}$ where HSE06 predicts much larger values than PBE. However, without an experimental baseline we can not conclude that this is the case. As in the other instances we find that HSE06 produces similar or lower band gaps compared to PBE despite of the smaller number of k-points.

As stated in section 6.2, we did not manage to converge the hybrid calculations using the tetrahedron method. We overcame this problem by first calculating the charge density using Gaussian smearing and utilizing the charge density to expedite TBC HSE06 calculations. The respective HSE06 band gaps of the five SQSs of the $(\text{CrFeMnNi})\text{Si}_2$ system from utilizing both methods are displayed in table 7.6. Here, the band gap is calculated from the eigenvalues at different cutoff occupancy occ to highlight the part of defect states.

SQS	Smearing (type)	$E_G^{up,eigen}$ (0.5) (eV)	$E_G^{down,eigen}$ (0.5) (eV)	$E_G^{up,eigen}$ (0.01) (eV)	$E_G^{down,eigen}$ (0.01) (eV)	$E_G^{tot,eigen}$ (0.5) (eV)	$E_G^{tot,eigen}$ (0.01) (eV)
A	Gaussian (0.05)	0.784	0.149	-	0.298	0.149	0.298
	Gaussian (0.005)	0.212	0.101	-	-	0.101	-
	TBC	0.708	0.026	-	-	0.026	-
B	Gaussian (0.05)	0.278	0.170	0.299	0.314	0.151	0.298
	Gaussian (0.005)	0.284	0.182	-	-	0.180	-
	TBC	0.286	0.182	-	-	0.181	-
C	Gaussian (0.05)	0.108	0.106	0.241	0.184	0.065	0.184
	Gaussian (0.005)	0.130	0.022	-	-	0.022	-
	TBC	0.174	0.033	-	-	0.020	-
D	Gaussian (0.05)	0.366	0.059	-	0.187	0.059	0.187
	Gaussian (0.005)	0.374	0.072	-	-	0.072	-
	TBC	0.378	0	-	0.267	0	0.267
E	Gaussian (0.05)	0.665	0.144	-	0.168	0.144	0.168
	Gaussian (0.005)	0.583	0.121	-	-	0.121	-
	TBC	0.548	0.013	-	-	0.013	-

Table 7.6: Band gap of five supercells of $(\text{CrFeMnNi})\text{Si}_2$ from HSE06 calculations using Gaussian smearing, with smearing width σ equal to 0.05 eV and 0.005 eV, and the tetrahedron method (TBC). "-" means that the band gap are unchanged between $\text{occ} = 0.5$ and $\text{occ} = 0.01$.

As we experienced for SQS B (PBE) in section 7.2.1, defect states are only a factor in the calculations using Gaussian smearing with $\sigma = 0.05$ eV. These band gaps contain defect states, and can consequently be enlarged. By comparing E_G^{up} and E_G^{dw} at $occ = 0.5$ and $occ = 0.01$, the defects appear to have a lesser role in spin up, as per SQS C the band gap in spin up is either consistent or only marginally different between the defect band gap and the hypothetical defect less band gap. E_G^{dw} on the other hand, increases significantly by removing the defect states. The Gaussian smearing method is generally in better agreement with TBC at lower smearing width. But even in this case we observe several dissimilarities. In SQS A and E, E_G^{dw} is larger with the Gaussian method, additionally E_G^{up} is much lower in SQS A. Furthermore, while the HSE06 band gap in SQS D using TBC is in good agreement with PBE, where both results in a spin up half-metal. The HSE06 calculation of this SQS using Gaussian smearing, predicts a semiconductor with band gap equal to 0.07 eV with $\sigma = 0.005$ eV. In this project we have based our choice of numerical smearing on the advice on the VASP manual stating that for accurate total energies and density of states in semiconductors, one should opt for the tetrahedron method [65]. However, seeing as our system is comprised of metals in addition to Si, we include the results from utilizing Gaussian smearing. There are of course many more factors that affect the accuracy and reliability of both methods, but these are outside the scope of this project.

The fact that the majority of functionals and SQS agree on the presence of a band gap is in itself an overwhelmingly positive result, that allow us to state with high certainty that the potential high-entropy silicide $(\text{CrFeMnNi})\text{Si}_2$ is in fact a semiconductor, or possibly a half-metal based on the observed spin polarization and the most stable configuration. Regarding the 3 functionals applied in this project, we experience best cohesion between PBE and HSE06 that both agree on a spin up polarization of the band gap, while SCAN predicts more symmetric band gaps. This can also be seen from the magnetic moment, whereas PBE and HSE06 yields a final magnetic moment (per atom) of $0.083 \mu_B$ across all SQSs, with SCAN this is reduced to half the amount. In the nonmagnetic $\beta\text{-FeSi}_2$ structure we find better agreement between PBE and SCAN. Both correctly predicts that the material is nonmagnetic, however compared to the experimental value of about 0.85 eV and the PBE band gap of 0.65 eV, we get a smaller band gap of 0.61 eV with SCAN. Thus, the SCAN functional does not necessarily result in increased accuracy over PBE, even in the simpler nonmagnetic structure. To conclude this section on the band gap of the $(\text{CrFeMnNi})\text{Si}_2$ alloy, when studying the band gap with DFT, particularly PBE is well known to underestimate the band gap of the real material as we experienced for FeSi_2 . Therefore, a band gap found with PBE indicates the existence of a band gap of at least the same size of the real material. In the following sections, we will heavily emphasize the PBE functional to determine the band gap from both the fast and reliable use in addition to the points mentioned above. Furthermore, from our experiences in this project in conjunction with the lack of support, the SCAN function looks to perform quite poorly with respect to band gaps. The HSE06 functional on

the other hand, yielded much more reliable results, however since it was often computationally expensive and troublesome to implement for the structures in this project, we apply this scarcely in proceeding sections.

7.2.4 Pair distribution functions

The pair distribution functions of SQS D and B are included below in figure 7.11. We compare the PDFs of the most stable configuration (SQS D) with those of SQS B to investigate distinctions between the half-metallic structure and the most stable semiconducting configuration (SQS B).

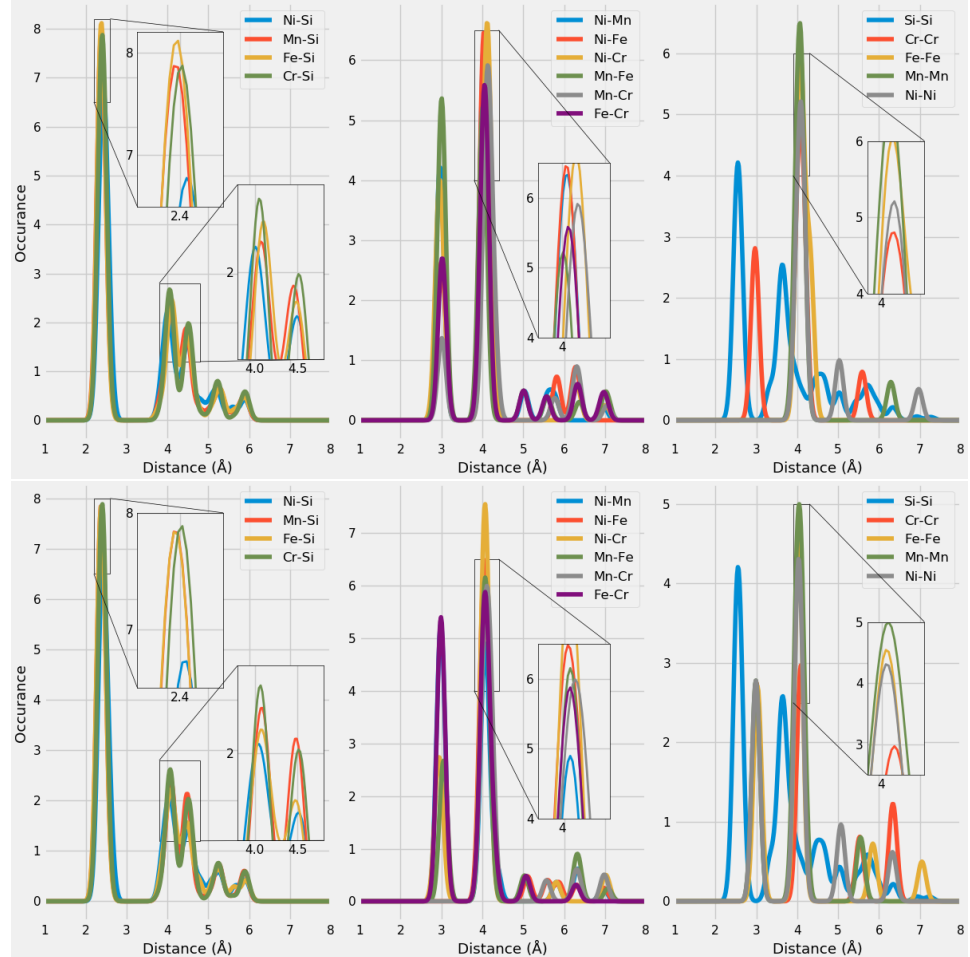


Figure 7.11: Pair distribution functions of SQS D (top) and B (bottom) of $(\text{CrFeMnNi})\text{Si}_2$.

With the aid of the ICSD [66], we can compare the PDFs in figure 7.11 to a compilation of PDFs based on a large number of experimental compounds. As these SQSs contains a total of 15 different bonds, comparing each one to the ICSD values would be an exhaustive process. According to the ICSD, the preferred bond-length of TM-Si bonds is observed at two values, with the shorter length the most occurring. Specifically Fe-Si bonds range between 2.25-2.75 Å and 4-5 Å, Mn-Si

between 2.25-2.75 Å and 3.5-5 Å, Ni-Si between 2.25-2.5 Å and 3.85-5 Å, and finally Cr-Si between 2.35-2.65 Å and 4-5 Å. Clearly, the PDFs of the SQSs are in good agreement with the listed values of TM-Si bonds. The relative occurrence of the bonds between SQS D and B are mostly consistent, other than marginally reduced Fe-Si occurrence at 2.4 Å in B.

Nevertheless, we observe several differences between TM-TM bonds in SQS D and B, such as Mn-Fe, Cr-Fe, and Ni-Mn bonds. This is simply a consequence of how the SQSs are generated; the silicon atoms are placed as before in the new supercells, but the TM elements are quasi-randomly distributed. Thus, it's reasonable that we would find the major differences between TM-TM bonds. Recalling that manganese in particular had a distinct presence in spin down around E_F in SQS D, we observe that this particular supercell compared to SQS B has a preference of Mn-Fe bonds at 3 Å compared to Fe-Cr in SQS B, and overall larger preference of Mn-Mn bonds. However, the differences between PDFs are difficult to relate to the observed properties. Firstly because of the sheer number of total bonds to analyze, and secondly considering the uniqueness of each SQS.

7.2.5 Charge density

Below we include the calculated charge density with PBE of SQS A, B, D and E of the $(\text{CrFeMnNi})\text{Si}_2$ alloy. We note that the half-metallic configuration (SQS D) appears to contain a marginally larger number of delocalized electronic charges in the lattice ,compared to the semiconducting SQSs. The charge density of SQS C is found in appendix A.3.

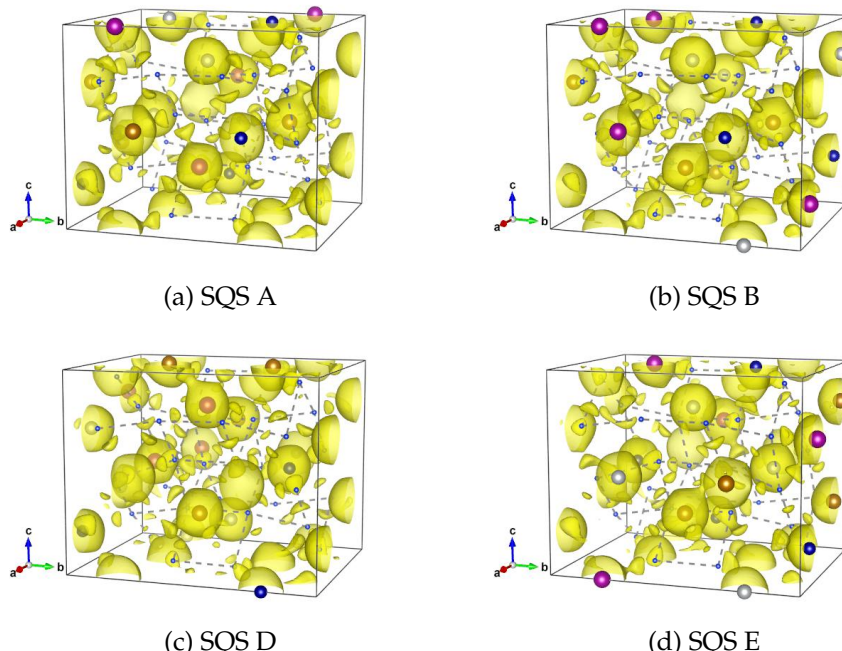


Figure 7.12: Contour plots of the Charge density of SQS A, B, D and E of $(\text{CrFeMnNi})\text{Si}_2$.

7.2.6 SQS size

Above we have presented the results of a high-entropy silicide $(\text{CrFeMnNi})\text{Si}_2$, investigated by five 48-atom SQSs with a volume of 700 \AA^3 . This intermediate size allowed for more computationally affordable computations, and enabled us to calculate the band gap by more complex and expensive functionals, moreover test different settings, computational factors and compositions. However, as we discussed in section 4.3, the application of the SQS method to HEAs is not necessarily straightforward. The most pressing concern is the size of the SQS model and if it's sufficient enough to correctly model the disordered multi-component structure. In this section we will investigate factors of the SQS-method on the band gap and related results, by studying the difference between the 48 atom SQSs discussed above, to that of 96 and 192-atom SQSs with volumes 1200 \AA^3 and 2400 \AA^3 respectively. The computational cost of the 3 models are displayed below in figure 7.13 in terms of the number of CPU hours for both geometric and electronic relaxation of the structures.

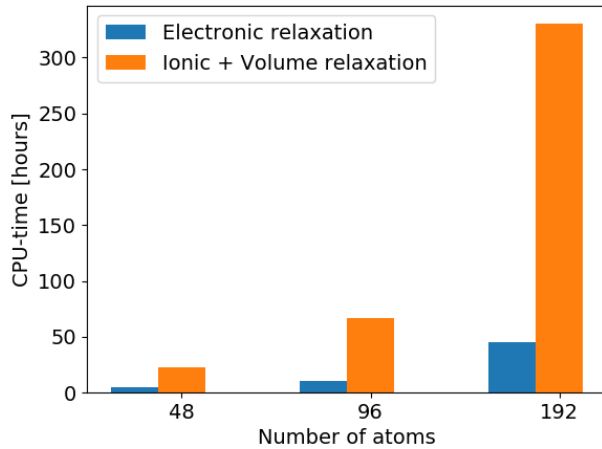


Figure 7.13: CPU time of 48, 96 and 192-atom SQSs of $(\text{CrFeMnNi})\text{Si}_2$

like the 48-atom model, the 96 and 192-atom SQS were tested by five unique configurations. In table 7.7 we list the mean and standard deviation from the set of configurations for all three sizes, with respect to the total energy per atom and final magnetic moment per atom, in addition to the formation energy of the mean total energy. Clearly, the 3 properties show minimal variation between the three sizes, furthermore we do not observe any indication of convergence with respect to the size. Thus, we may state that the 48-atom SQSs is sufficient for these materials. On the other hand, we observe that the larger models contain larger deviation between configurations, this can be expected given the increased total number of atoms that can vary between configurations.

SQS size	Toten (eV)		Mag (μ_B)		E_{FPA} (eV)
	mean	std	mean	std	
48 atoms	- 6.611	0.004	0.083	0.000	-0.292
96 atoms	- 6.609	0.002	0.071	0.011	-0.292
192 atoms	- 6.612	0.002	0.076	0.017	-0.295

Table 7.7: Total energy (Toten), magnetic moment (Mag) and formation energy ($E_{text{FPA}}$) of 48, 96 and 192 atom SQSs of (CrFeMnNi)Si₂

The band gap corresponding to SQSs of each size are listed in table 7.8. First and foremost the band gap is evident in all three and exhibits analogous spin polarization, however appears to be less frequent and smaller in the larger structures. This result could simply be related to the uniqueness of each SQS, as also in the larger SQSs we observe sizable band gaps in certain configuration. Additionally, the larger cells has an increased possibility to create defect states.

SQS size	SQS	$E_G^{up,eigen}(0.5)$ (eV)	$E_G^{dw,eigen}(0.5)$ (eV)	$E_G^{tot,eigen}(0.5)$ (eV)
48 atoms	A	0.082	0.052	0.028
	B	0.293	0.052	0.052
	C	0.236	0.034	0.034
	D	0.339	0	0
	E	0.308	0.050	0.050
96 atoms	A	0.171	0.044	0.037
	B	0.139	0.027	0.027
	C	0.135	0.036	0.008
	D	0.089	0.040	0.040
	E	0.161	0	0
192 atoms	A	0.120	0.032	0.032
	B	0.144	0	0
	C	0.187	0	0
	D	0.048	0.034	0
	E	0.013	0.018	0.013

Table 7.8: Band gap of SQSs of 48, 96 and 192-atoms of (CrFeMnNi)Si₂. The names are arbitrary, A in 48 does not equal A in 96 or A in 192. The values listed in *italic* relate to a defect band gap. Structures listed in bold text represents the most stable supercell of the set of SQSs.

Equivalent to structure D in the 48 atom SQS, we find that the 0 band gap in SQS E in the 96 atom model suffers from defect states, without defects we find $E_G^{dw,eigen}(0.01) = 0.016$ eV. The same is true for SQS B and C (192), but require $occ = 0.001$ to yield a small finite value. The

band gap in SQS D and E (192) on the other hand, is finite at $occ = 0.5$, but can be enlarged from increasing occ , as we described for calculations utilizing Gaussian smearing with $\sigma = 0.05$ eV. Specially, In SQS D (192-atoms), $E_G^{up,eigen}(0.01) = 0.075$ eV and $E_G^{dw,eigen}(0.01) = 0.05$ eV, similarly $E_G^{up,eigen}(0.01) = 0.05$ eV, and $E_G^{dw,eigen}(0.01) = 0.048$ eV in SQS E (192-atoms). In such cases where the eigenvalues inclusive of defect states return a finite band gap, the density of states does not. This is seen in figure 7.14 for SQS E in the 192-atom model that clearly has nonzero DOS at E_F in both spin direction.

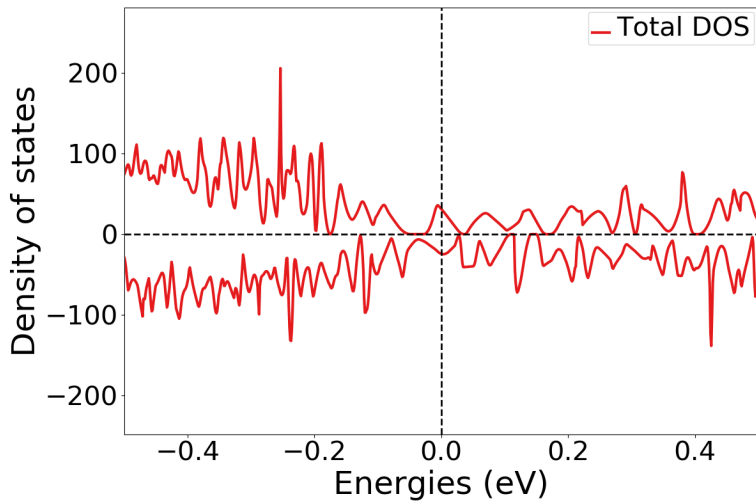


Figure 7.14: Density of states [states/eV] of SQS E of the 192-atom model of $(\text{CrFeMnNi})\text{Si}_2$.

One could wonder if the very narrow band gap in SQS E (192) of 0.013 eV is subject to numerical precision in the DOS. But on the grounds of the small value we calculated the DOS in this case by 20000 points over the energy range -12 eV to 12 eV, which results in a resolution of about 8 points per 0.01 eV. In other words this should not be a factor.

Drawing any conclusion on the band gaps is difficult seeing as we find very different results within all 3 sizes. The most stable SQSs suggests that the band gap converge towards a small or possible non-existent band gap with increasing SQS size. On the other hand we also find evidence of large band gaps in the larger cells in less stable configurations. This goes back to section 3.3 where we mentioned that one particular difficulty of the SQS method is the large number of possible atomic configurations of one compositions.

Looking at the pair distribution functions of the most stable SQS in each model (figure 7.15), we observe that short-range interactions is well represented and identical across all three models. The distinctions between preferences as discussed in section 7.2.4 are most likely a product of the uniqueness of the SQSs more so than the size. On the other hand, the larger SQSs clearly provide a better description of long-range interactions that is

not nearly as present in the smaller supercell. But, as seen from the minimal variation of the values in table 7.7 between the 3 models, in accordance with the fundamental philosophy of the SQS method, the functional properties are determined primarily from short-range interactions in the lattice. Thus, despite the fact that the larger SQSs offer improvements over the smaller SQSs, the gain is not justified by the increased computational cost.

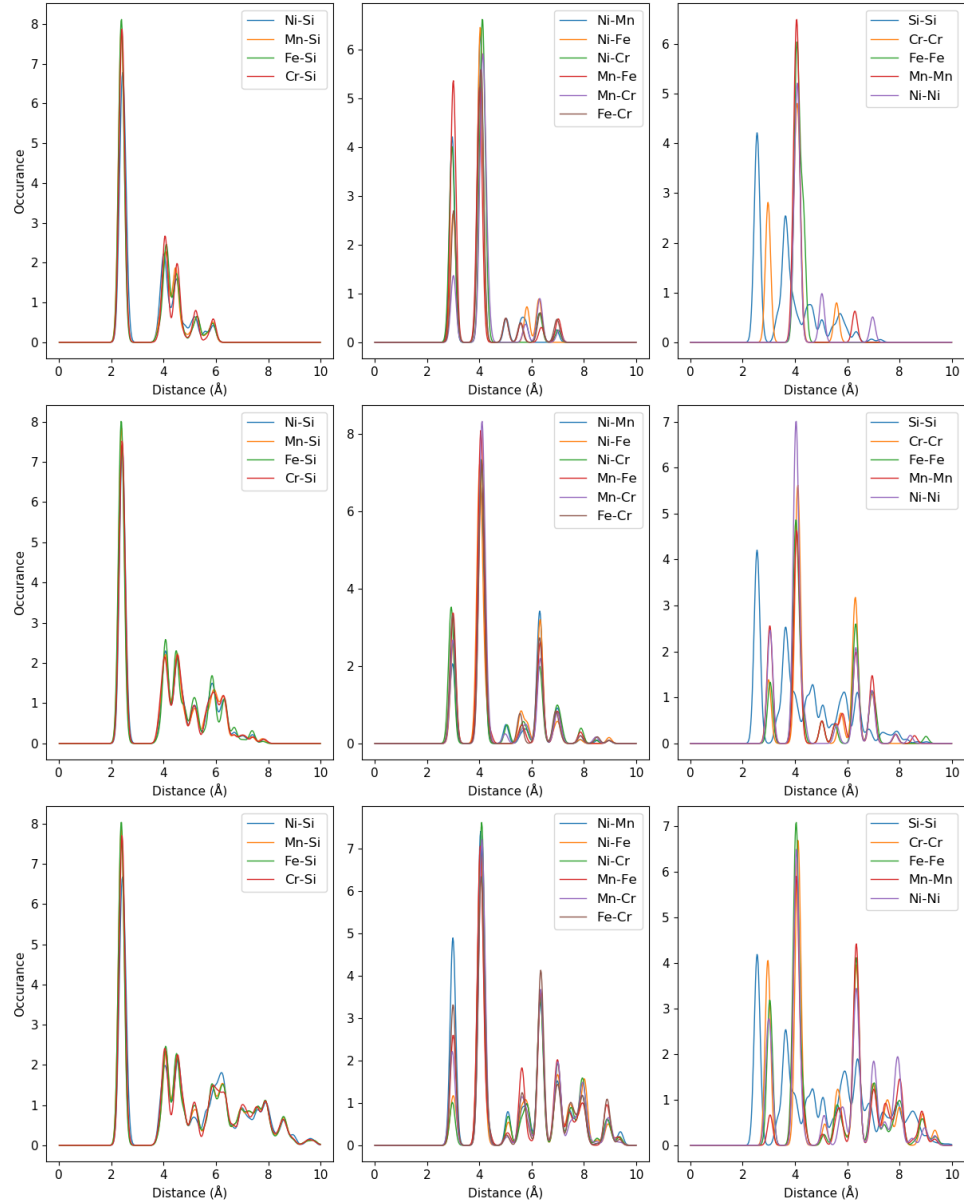


Figure 7.15: Pair distribution functions of $(\text{CrFeMnNi})\text{Si}_2$ (top) 48-atom SQS, (middle) 96-atom SQS, (bottom) 192-atom SQS.

Chapter 8

Alternative compositions

Up until this point we have looked in detail at the high-entropy silicide $(\text{CrFeMnNi})\text{Si}_2$. In this chapter we will broaden our search of compositions based on the β - FeSi_2 structure. First, we will look at various compositions inside the quaternary phase diagram of Cr, Fe, Mn and Ni, then consider some compositions where chromium, manganese or nickel are replaced by cobalt or titanium.

8.1 Exploring the quaternary phase diagram of Cr, Fe, Mn and Ni.

In this section, we aim to expand our search of this diagram by generating SQSs of the 48 atom model slightly away from equimolar distribution of 3d elements. The list of compositions are listed in table 8.1, with corresponding total energy, magnetic moment and formation energy in the familiar format. Ideally each composition would differ only by one element to provide a clear view of each direction in the phase diagram, but the TDEP implementation insisted in also reducing Nickel to stay consistent with the 48 atom supercell.

Composition	Toten (eV)		Mag (μ_B)		E_{FPA} (eV)
	mean	std	mean	std	
$\text{Cr}_3\text{Fe}_3\text{Mn}_7\text{Ni}_3\text{Si}_{32}$	- 6.695	0.004	0.138	0.019	-0.300
$\text{Cr}_5\text{Fe}_5\text{Mn}_3\text{Ni}_3\text{Si}_{32}$	- 6.671	0.003	0.113	0.022	-0.286
$\text{Cr}_5\text{Fe}_3\text{Mn}_5\text{Ni}_3\text{Si}_{32}$	- 6.685	0.004	0.138	0.046	-0.271
$\text{Cr}_3\text{Fe}_5\text{Mn}_5\text{Ni}_3\text{Si}_{32}$	- 6.680	0.004	0.094	0.021	-0.315
$\text{Cr}_3\text{Fe}_3\text{Mn}_3\text{Ni}_7\text{Si}_{32}$	- 6.392	0.008	0.016	0.010	-0.285

Table 8.1: Total energy (Toten), magnetic moment (Mag) and formation energy E_{FPA} of various compositions of the Cr-Fe-Mn-Ni-Si system.

In table 8.1 we observe that moving away from the equimolar system result in both less and more stable alloys. Clearly the lowest formation

energies (most stable) correspond to compositions rich in manganese and poor in chromium. Likewise the least stable compositions in table 8.1 contain either increased amounts of Cr or reduced amounts of Mn compared to the equimolar system. In the equimolar composition the magnetic moment was attributed to primarily Cr and Mn atoms in the lattice. In table 8.1 we observe similarly that compositions rich in Cr and Mn exhibits the largest magnetic moments and vice versa. The band gaps of the respective compositions in five unique SQSs can be seen in table 8.2 below, calculated with PBE GGA.

Composition	SQS	$E_G^{\text{up, eigen}}(0.5)$ (eV)	$E_G^{\text{dw, eigen}}(0.5)$ (eV)	$E_G^{\text{tot, eigen}}(0.5)$ (eV)
$\text{Cr}_3\text{Fe}_3\text{Mn}_7\text{Ni}_3\text{Si}_{32}$	A	0.339	0	0
	B	0.475	0	0
	C	0.134	0	0
	D	0.195	0.006	0.006
	E	0.421	0	0
$\text{Cr}_5\text{Fe}_5\text{Mn}_3\text{Ni}_3\text{Si}_{32}$	A	0.003	0	0
	C	0.210	0	0
	D	0.067	0.041	0.037
	E	0.362	0	0
$\text{Cr}_5\text{Fe}_3\text{Mn}_5\text{Ni}_3\text{Si}_{32}$	A	0.208	0	0
	B	0.405	0	0
	C	0.466	0	0
	D	0.084	0.012	0.012
	E	0.301	0	0
$\text{Cr}_3\text{Fe}_5\text{Mn}_5\text{Ni}_3\text{Si}_{32}$	A	0.392	0	0
	C	0.129	0	0
	D	0.260	0.100	0.100
	E	0.359	0.100	0.085
$\text{Cr}_3\text{Fe}_3\text{Mn}_3\text{Ni}_7\text{Si}_{32}$	A	0	0	0
	B	0	0	0
	C	0	0	0
	D	0	0	0
	E	0.040	0	0

Table 8.2: Band gaps of various compositions of the Cr-Fe-Mn-Ni-Si system. The most stable SQS of a set is highlighted in bold text, defect/impurity band gaps are listed in *italic*. Some SQSs were excluded from the table due to unsuccessful calculations. All band gaps calculated with PBE GGA.

From table 8.2 we observe that most compositions are half-metals like the equimolar system with a spin up polarization. Each composition shows large variation between configurations. We note $E_{G,\text{max}}^{\text{up}} \approx 0.5$ eV and $E_{\text{min}}^{\text{up}} \approx 0.1$ eV in both $\text{Cr}_3\text{Fe}_3\text{Mn}_7\text{Ni}_3\text{Si}_{32}$ and $\text{Cr}_5\text{Fe}_3\text{Mn}_5\text{Ni}_3\text{Si}_{32}$, and further

$E_{G,\max}^{\text{up}} \approx 0.4$ eV and $E_{\min}^{\text{up}} \approx 0.1$ eV in $\text{Cr}_3\text{FeMn}_5\text{Ni}_3\text{Si}_{32}$. In all three of these compositions the proportion of manganese is increased relative to the equimolar system, and two out of the three compositions contain reduced amounts of chromium. Looking at the two compositions with the least indication of a band gap $\text{Cr}_5\text{Fe}_5\text{Mn}_3\text{Ni}_3\text{Si}_{32}$ and $\text{Cr}_3\text{Fe}_3\text{Mn}_3\text{Ni}_7$, these contain reduced amounts of manganese. Thus, based on the few compositions tested in this experiment we can state a relation of the band gap mainly to manganese, but also chromium.

Based on the most stable configuration of each composition, we observe very encouraging results in the $\text{Cr}_3\text{Fe}_3\text{Mn}_7\text{Ni}_3\text{Si}_{32}$ composition with the largest E_G^{up} of the set of configurations. Likewise the most stable SQS of the $\text{Cr}_3\text{Fe}_5\text{Mn}_5\text{Ni}_3\text{Si}_{32}$ composition is a semiconductor with a total band gap of about 0.1 eV. In the composition $\text{Cr}_5\text{Fe}_5\text{Mn}_3\text{Ni}_3\text{Si}_{32}$, the most stable SQS predicts a defect or impurity band gap as we discussed previously where the eigenvalues return a finite band gap despite of defect states. However we have not been able to investigate the nature and effect of this impurity band gap to further extent, likewise for the similar impurity gaps listed in table 8.2 and the 0 band gaps in spin down. Below in figures 8.1 and 8.2 we include the projected density of states around E_F of the most stable SQS of each composition. Because we only include and discuss the most stable SQS, the features of these figures can be subject to the uniqueness of that particular SQS rather than a distinct feature of the exact composition, however as stated previously the most stable configuration provides the most likely properties of the composition within the scope of this project.

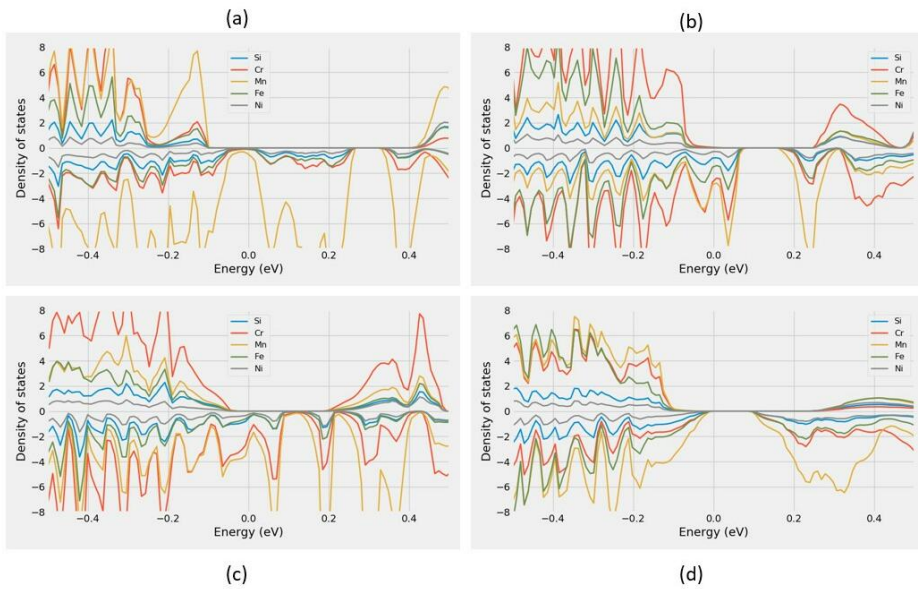


Figure 8.1: Projected density of states [states/eV] of (a) $\text{Cr}_3\text{Fe}_3\text{Mn}_7\text{Ni}_3\text{Si}_{32}$ (SQS B), (b) $\text{Cr}_5\text{Fe}_5\text{Mn}_3\text{Ni}_3\text{Si}_{32}$ (SQS C), (c) $\text{Cr}_5\text{Fe}_3\text{Mn}_5\text{Ni}_3\text{Si}_{32}$ (SQS A), (d) $\text{Cr}_3\text{Fe}_5\text{Mn}_5\text{Ni}_3\text{Si}_{32}$ (SQS D)

The PDOSs are in good agreement with the listed values in table 7.2.

$\text{Cr}_3\text{Fe}_3\text{Mn}_7\text{Ni}_3\text{Si}_{32}$ and $\text{Cr}_5\text{Fe}_3\text{Mn}_5\text{Ni}_3\text{Si}_{32}$ both display sizable band gaps in spin, while figure 8.1 d point to a total band gap around 0.1 eV for SQS D of $\text{Cr}_3\text{Fe}_5\text{Mn}_5\text{Ni}_3\text{Si}_{32}$. On the other hand we observe as for the 192-atom SQS a dissimilarity between the density of states band gap in $\text{Cr}_5\text{Fe}_5\text{Mn}_3\text{Ni}_3\text{Si}_{32}$ SQS C (figure 8.1 b) and the eigenvalue (impurity) band gap listed in table 7.2. This can be better understood by figure A.3 in appendix A.1 that clearly show small finite values at E_F in spin up. This DOS may resemble that of a doped material.

In figure 7.7 we observed that manganese distinctly occupied states in the spin down channel around E_F and was a key contributor as to why the spin down channel of $(\text{CrFeMnNi})\text{Si}_2$ was metallic in the most stable SQS. This is also largely the case in the compositions shown above in figure 8.1 and 8.2, and is particularly evident in figure 8.1 where Mn dominates the spin down states around E_F in the $\text{Cr}_3\text{Fe}_3\text{Mn}_7\text{Ni}_3\text{Si}_{32}$ composition. By reducing the number of Mn we still find that the Mn states prohibit the band gap in spin down, as seen in figure 8.1 b. In the chromium rich compositions plotted in figures 8.1 b and c, we observe that also Cr states prohibit the spin down band gap, and dominate states near E_F in spin up as well. Contrary, in the $\text{Cr}_3\text{Fe}_3\text{Mn}_3\text{Ni}_7\text{Si}_{32}$ composition plotted in figure 8.2, we do not observe any distinct peaks of elements, but rather consistent small finite DOS around E_F in all elements. The sole composition with clear evidence of a spin down gap is from the chromium poor system plotted in figure 8.1 d. Also in this structure we see that the effects of Mn around E_F is dominant in spin down from the relative large amounts of Mn, but in comparison to the other composition these states are pushed away from the Fermi energy.

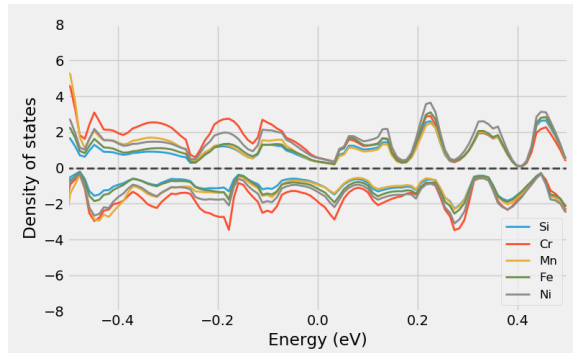


Figure 8.2: Projected density of states [states/eV] of $\text{Cr}_3\text{Fe}_3\text{Mn}_3\text{Ni}_7\text{Si}_{32}$ around the Fermi energy.

An important factor of these results is that because each composition alters simultaneous elements, interpreting and relating the results to a particular alteration is challenging. For example, is the result of the $\text{Cr}_5\text{Fe}_3\text{Mn}_5\text{Ni}_3\text{Si}_{32}$ permutation a consequence of less Fe or increments to both Cr and Mn? Furthermore, is the large band gap in spin up of $\text{Cr}_3\text{Fe}_3\text{Mn}_7\text{Ni}_3\text{Si}_{32}$ a product of increasing manganese or reducing the other elements? From the comparatively large gaps in spin up of

$\text{Cr}_3\text{Fe}_3\text{Mn}_7\text{Ni}_3\text{Si}_{32}$ and $\text{Cr}_3\text{Fe}_5\text{Mn}_5\text{Ni}_3\text{Si}_{32}$, in combination with a larger presence of Cr states in spin up in the Cr rich permutations, we here ascribe the large band gaps to a reduction of chromium, more so than other effects. However, we observe from both $\text{Cr}_5\text{Fe}_5\text{Mn}_4\text{Ni}_3\text{Si}_{32}$ and $\text{Cr}_3\text{Fe}_3\text{Mn}_3\text{Ni}_7\text{Si}_{32}$ (figure 8.2) in addition to the manganese rich composition, that Mn plays a vital role on the band gap of these structures. It's clear that the $\text{Cr}_3\text{Fe}_5\text{Mn}_5\text{Ni}_3\text{Si}_{32}$ alloy manages to strike a balance between 3d elements that results in a specific interplay and correspondingly very promising properties. It could have been instructive to look at for example the pair distribution functions and compare to the equimolar system, but from the factors discussed in section 7.2.4, we leave this to future work.

As stated previously, we have relied on the PBE GGA functional to determine the band gap, from its reliability and favorable computation cost. Nevertheless, we have conducted calculations with SCAN and HSE06 on some of the more promising structures. For instance, in SQS D of the $\text{Cr}_3\text{Fe}_5\text{Mn}_5\text{Ni}_3\text{Si}_{32}$ alloy, we get lower values in both spin up and down with SCAN, specifically $E_{G,\text{SCAN}}^{\text{up}} = 0.21 \text{ eV}$ and $E_{G,\text{SCAN}}^{\text{dw}} = 0.08 \text{ eV}$. With the HSE06 functional we get $E_{G,\text{HSE06}}^{\text{up}} = 0.53 \text{ eV}$ and $E_{G,\text{HSE06}}^{\text{dw}} = 0 \text{ eV}$. In SQS B of the $\text{Cr}_3\text{Fe}_3\text{Mn}_7\text{Ni}_3\text{Si}_{32}$ alloy, the PBE functional resulted in band gaps equal to $E_{G,\text{PBE}}^{\text{up}} = 0.47 \text{ eV}$ and $E_{G,\text{PBE}}^{\text{dw}} = 0 \text{ eV}$. Contrary, SCAN yields a small band gap in spin down of about 0.002 eV, and a 0 gap in spin up of this structure. Similarly, the HSE06 band gaps of this structure are $E_{G,\text{HSE06}}^{\text{up}} = 0.08 \text{ eV}$ and $E_{G,\text{HSE06}}^{\text{dw}} = 0.11 \text{ eV}$. Moreover, this is a defect band gap, thus we can get $E_{G,\text{HSE06}}^{\text{up, eigen}}(0.01) = 0.18 \text{ eV}$ and $E_{G,\text{HSE06}}^{\text{dw, eigen}}(0.01) = 0.16 \text{ eV}$.

8.2 High-entropy silicides with cobalt/titanium

The compositions in this section are deliberate combinations, intended to both investigate the role of individual elements in the $(\text{CrFeMnNi})\text{Si}_2$ system, and broaden our search of potential high-entropy silicides based on $\beta\text{-FeSi}_2$. In these alloys we replace Cr, Mn or Ni, with Co or Ti. Note that the alloys contains a total of 48 atoms as before, with equimolar distribution of 3d elements. In similar fashion to the preceding section, we begin by presenting in table 8.3, the mean and standard deviation of the total energy and magnetic moment of 5 distinct SQSs of each alloy

Composition	Toten (eV)		Mag (μ_B)		E_{FPA} (eV)
	mean	std	mean	std	
$(\text{CrFeCoNi})\text{Si}_2$	- 6.466	0.006	0.008	0.016	- 0.308
$(\text{CoFeMnNi})\text{Si}_2$	- 6.473	0.005	0.000	0.000	- 0.355
$(\text{CrFeTiNi})\text{Si}_2$	- 6.422	0.009	0.031	0.029	- 0.209
$(\text{CrFeMnTi})\text{Si}_2$	- 6.699	0.007	0.114	0.064	- 0.199
$(\text{CrFeMnCo})\text{Si}_2$	- 6.769	0.003	0.133	0.033	- 0.323

Table 8.3: Total energy (Toten), magnetic moment (Mag) and formation energy (E_{FPA}) of alloys based on combinations of Cr, Fe, Mn, Ni, Co, Ti and Si.

In terms of the formation energy, we observe that cobalt evidently yield the most stable alloys, with $(\text{CoFeMnNi})\text{Si}_2$ at the top and $(\text{CrFeCoNi})\text{Si}_2$ at the bottom. On the other side, both $(\text{CrFeTiNi})\text{Si}_2$ and $(\text{CrFeMnTi})\text{Si}_2$ where we introduce titanium in place of manganese and nickel respectively, results in the overall least stable compositions. A precise physical interpretation of the stability between compositions is challenging from the shallow analysis in this project, but we note that the two most stable alloys consists of the most chemically similar elements, with respect to properties such as electronegativity and atomic size. Accordingly, the least stable alloys are comprised of the most chemically dissimilar elements. This is in good agreement with the discussion in section 2.2, regarding phase formation of high-entropy alloys. Additionally, in the compositions discussed in the previous section, we observed that the most stable composition was $\text{Cr}_3\text{Fe}_5\text{Mn}_5\text{Ni}_3\text{Si}_{32}$, where the Cr proportion was reduced. In conjunction with the results of the titanium alloys above, we may suspect that smaller elements are ill-suited in these alloys constructed from the FeSi_2 structure.

In line with the other compositions studied in this project, the magnetization is clearly related to chromium and manganese also in this case. This is seen by the overall lowest magnetic moments in the two compositions without these elements, and reversely the highest magnetic moments are associated to compositions comprised of both chromium and manganese. Comparing the magnetic moments of $(\text{CrFeCoNi})\text{Si}_2$

and $(\text{CoFeMnNi})\text{Si}_2$, it appears that chromium is most responsible for the magnetism of these alloys. Furthermore, we observe that substituting Ni with either Ti and Co yields increased magnetic moments. As we have discussed previously, the uniqueness of each SQS makes it difficult to draw conclusion on various properties. In table 8.4 below, we list the magnetic moments of the most stable SQS of each alloy. Contrary to the mean value of the set of configurations, the most stable supercell of $(\text{CrFeCoNi})\text{Si}_2$, like the $(\text{CoFeMnNi})\text{Si}_2$ alloy is nonmagnetic. Moreover, the $(\text{CrFeMnTi})\text{Si}_2$ composition is less magnetic relative to both $(\text{CrFeMnCo})\text{Si}_2$ and $(\text{CrFeMnNi})\text{Si}_2$, as opposed to the mean values.

Composition	Magnetic moment (μ_B)
$(\text{CrFeCoNi})\text{Si}_2$	0
$(\text{CoFeMnNi})\text{Si}_2$	0
$(\text{CrFeTiNi})\text{Si}_2$	0.065
$(\text{CrFeMnTi})\text{Si}_2$	0.079
$(\text{CrFeMnCo})\text{Si}_2$	0.167

Table 8.4: Magnetic moment of the most stable SQS of alloys comprised of combinations of Cr, Fe, Mn, Ni, Co, Ti and Si.

Thus, based on the most stable configurations of each composition, we can state that replacing either Cr or Mn (with Co), removes the magnetic moment of the alloy. Furthermore we find that the magnetic moment is reduced when Ni is substituted with Ti, and increased by Co. However, while substituting manganese with Co yields a nonmagnetic alloy, Ti for Mn only slightly reduces the magnetic moment.

In regards to the band gaps of these alloys, the majority are metals with the exception of the $(\text{CrFeMnCo})\text{Si}_2$ alloy. Here, we locate a band gap in the spin up direction slightly below 0.5 eV. In addition, the $(\text{CrFeTiNi})\text{Si}_2$ also exhibits a small band gap in the spin up direction. As have been the case throughout this project, we learn that the metallic structures are caused by defect states at the band edges. By removing said defect states analogous to what we have done previously, we can find total band gaps of around 0.05 eV in the most stable supercell in each of five alloys. Furthermore, both of the spin up band gaps found for the $(\text{CrFeTiNi})\text{Si}_2$ alloy and $(\text{CrFeMnCo})\text{Si}_2$, are enlarged from neglecting defect states, deeming these as defect band gaps equal to what we have experienced in other instances. Following the discussion above on the magnetic moments of the different compositions, we note the largest spin polarization of the hypothetical band gaps in the $(\text{CrFeMnCo})\text{Si}_2$ and $(\text{CrFeTiNi})\text{Si}_2$ alloys. On the other hand, the remaining three compositions exhibits identical hypothetical band gaps in both spin directions. The results discussed above can be seen in table 8.5. The projected density of states of the half-metallic supercell of the $(\text{CrFeMnCo})\text{Si}_2$ alloy is displayed in figure 8.3.

Composition	<i>occ</i>	$E_G^{\text{up, eigen}}$ (eV)	$E_G^{\text{dw, eigen}}$ (eV)	$E_G^{\text{tot, eigen}}$ (eV)
$(\text{CrFeCoNi})\text{Si}_2$	0.5	0	0	0
	0.1	0.001	0.040	0.001
	0.01	0.063	0.063	0.063
$(\text{CrFeTiNi})\text{Si}_2$	0.5	0.007	0	0
	0.1	0.061	0.009	0.009
	0.01	0.061	0.037	0.037
$(\text{CoFeMnNi})\text{Si}_2$	0.5	0	0	0
	0.1	0.004	0.004	0.004
	0.01	0.027	0.027	0.027
$(\text{CrFeMnTi})\text{Si}_2$	0.5	0	0	0
	0.1	0.021	0.001	0
	0.01	0.030	0.030	0.022
$(\text{CrFeMnCo})\text{Si}_2$	0.5	0.461	0	0
	0.1	0.607	0.022	0.022
	0.01	0.607	0.025	0.025

Table 8.5: The band gaps in spin up/down and total of the most stable SQS of alloys comprised of combinations of Cr, Fe, Mn, Ni, Co, Ti and Si. Calculated from eigenvalues with different occupancy cutoff *occ* using PBE GGA.

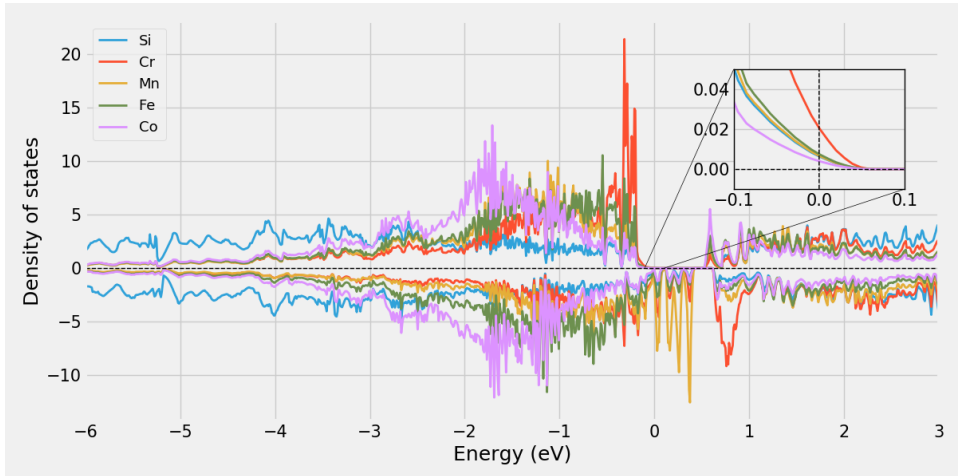


Figure 8.3: Projected density of states [states/eV] of $(\text{CrFeMnCo})\text{Si}_2$.

As was generally the case for the Cr:Fe:Mn:Ni:Si alloys, this structure displays a dominant number of manganese states in spin down at energies just above E_F , and a large number of Cr states right below E_F in spin up. Analog to the most stable supercell of the $\text{Cr}_5\text{Fe}_5\text{Mn}_3\text{Ni}_3\text{Si}_{32}$ alloy discussed in section 8.1, the presence of defect states in the spin up band gap of

CrFeMnCoSi_2 , results in small finite DOS at the Fermi energy, and the band gap calculated from the eigenvalues is shifted above E_F , resembling that of a doped material. The PDOSs of the other four alloys is displayed in figure 8.4. In agreement with the values listed in table 8.5, we observe from the PDOS that these are metallic compounds with finite DOS at E_F in both spins.

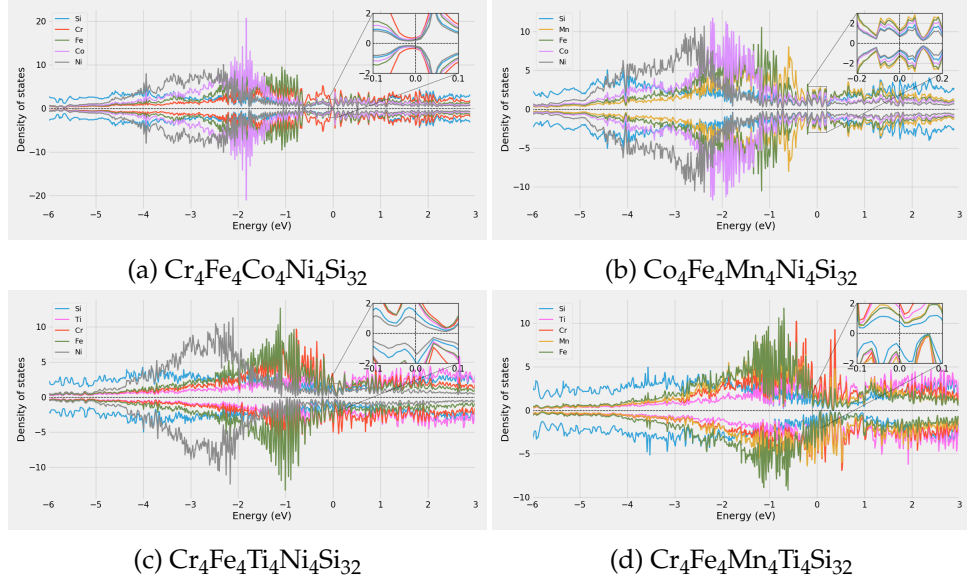


Figure 8.4: Projected density of states [states/eV] of alloys comprised of combinations of Cr, Fe, Mn, Ni, Co, Ti and Si.

Above we have evaluated the band gaps of the different compositions based solely on the most stable supercells. In $(\text{CrFeCoNi})\text{Si}_2$, $(\text{CrFeTiNi})\text{Si}_2$, $(\text{CrFeMnTi})\text{Si}_2$ and $(\text{CrFeMnCo})\text{Si}_2$, we find similar properties across all five configurations. On the other side, in the metallic alloy $(\text{CoFeMnNi})\text{Si}_2$, we discover very narrow total band gaps in two lesser stable configurations (SQS A and E) of 0.03 eV and 0.006 eV respectively. The density of states of these structures are displayed in figure 8.5.

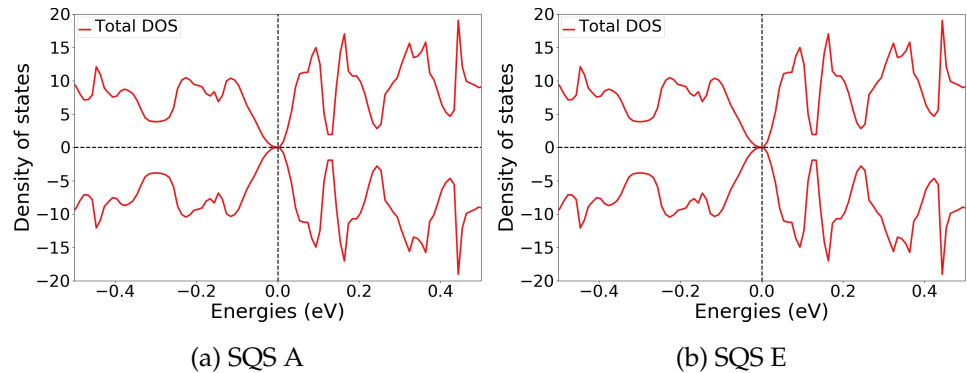


Figure 8.5: Density of states [states/eV] of SQS A and E of $(\text{CoFeMnNi})\text{Si}_2$.

8.3 Negative systems

In the above sections we have observed that aside from the $(\text{CrFeMnNi})\text{Si}_2$ alloy, we have had limited success in locating semiconducting alloys when moving away from the $(\text{CrFeMnNi})\text{Si}_2$ alloy, and particularly from the Cr-Fe-Mn-Ni-Si system. In addition to the alloys disused above, we have carried out similar simulations on other alloys not included in this report. In most of these alloys we experienced limited or no success with respect to the band gap. All five SQSs of a $(\text{ScVMnZn})\text{Si}_2$ alloy based on FeSi_2 turned out metallic. In $(\text{VMnFeCu})\text{Si}_2$, we found one supercell with a defect band gap of 0.007 eV. Furthermore, we tested various four-element compositions such as $\text{Cr}_6\text{Co}_6\text{Ni}_4\text{Si}_{32}$, $\text{Cr}_6\text{Fe}_6\text{Co}_4\text{Si}_{32}$, $\text{Cr}_6\text{Fe}_6\text{Ni}_4\text{Si}_{32}$ and $\text{Fe}_6\text{Co}_6\text{Ni}_4\text{Si}_{32}$. Out of these four compositions and corresponding 20 total SQSs, noteworthy we found a defect band gap of 0.15 eV in the spin up direction in one supercell of $\text{Cr}_6\text{Fe}_6\text{Co}_4\text{Si}_{32}$, and a spin up band gap of 0.27 eV in $\text{Cr}_6\text{Fe}_6\text{Ni}_4\text{Si}_{32}$. In the latter, we observed smaller single spin band gaps in additional configurations as well. The other two compositions were metallic across all tested supercells.

In this project, we have based our alloys on the Semiconductor β - FeSi_2 . However, we started this project by examining high-entropy silicides based on trigonal Fe_2Si . Here, we constructed similarly five distinct supercells of $(\text{CrFeCoNi})_2\text{Si}$ and $(\text{CrFeMnNi})_2\text{Si}$. The supercells consisted of a total of 54 atoms, with 18 silicon atoms and the remaining 32 sites distributed equimolarly between 3d elements. Furthermore, we have performed simulations of the $(\text{CrFeMnNi})\text{Si}_2$ composition in 72-atom SQSs of hexagonal CrSi_2 , and 44-atom SQSs of tetragonal and orthorombic Mn_4Si_7 as well. First and foremost, these systems were much more computationally demanding than the FeSi_2 based alloys, thus not all five supercells of these systems succeeded. Of the structures successfully relaxed and electronically converged, we found predominantly metallic structures.

Part IV

Conclusion and future work

Chapter 9

Conclusion

High-entropy alloys has emerged as a rapidly growing interest in materials science from the large range of possibilities and flexibility. In this project we have set out to study the possibility of a narrow gap semiconducting high-entropy silicide with top of the line computational power and methods, in the prospect of discovering next-generation efficient thermoelectric materials. The materials in mind were based on the FeSi_2 semiconductor, and modeled with the SQS method in the framework of DFT. To study the potential semiconductors we generated five distinct configurations of each composition and investigated the band gap, mainly with PBE GGA.

Our most successful effort was based around a 48-atom model of chromium, iron, manganese, and nickel in the Cr:Fe:Mn:Ni:Si system. In the equimolar composition $(\text{CrFeMnNi})\text{Si}_2$, we observed large variation of the band gap between the five distinct configurations. In the spin up direction, the band gap ranged from 0.08 - 0.34 eV. The most stable supercell was a half-metal with a spin up band gap of 0.34 eV, while the other four supercells displayed small spin down gaps between 0.03 eV and 0.05 eV as well. Calculations with SCAN and HSE06 produced unpredictable outputs that varied greatly between SQSs, and contained a larger degree of uncertainty compared to PBE. However, with HSE06 we found spin up band gaps of 0.55 eV and 0.71 eV in two respective supercells, and a total band gap of 0.18 eV in another. With the SCAN functional we found total band gaps around 0.1 in three SQSs, one metallic supercell, and one half-metallic structure with a spin down band gap of 0.1 eV.

Following the equimolar composition, we conducted a brief exploration of the quaternary phase diagram of this composition. Contrary to the equimolar system, we found here more frequently half-metallic structures. By analyzing the projected density of states we were able to relate the metallic spin down channel to a dominant presence of manganese states around the Fermi energy. Inside the number of different compositions that we tested, we found evidence for that there exists a positive relation between the band gap, most notably in spin up, and compositions poor in chromium and/or rich in manganese. Specifically, we located two promising compositions: $\text{Cr}_3\text{Fe}_3\text{Mn}_7\text{Ni}_3\text{Si}_{32}$ and $\text{Cr}_3\text{Fe}_5\text{Mn}_5\text{Ni}_3\text{Si}_{32}$, where the most stable supercell of the former displayed a spin up band gap of

0.47 eV, and the latter a total band gap of 0.1 eV, with PBE.

Lastly, we tested compositions of the FeSi₂ based alloys consisting of cobalt/titanium in place of either Cr, Mn or Ni. Based on the most stable configurations of these compositions, the only band gaps we found in this experiment was a spin up band gap of 0.46 eV in (CrFeMnCo)Si₂. By manually investigating the calculated eigenvalues of the different compositions, we were able to relate the metallic compounds to defect states. This is a familiar term in random alloys, in which states at the band edges deviate slightly from completely full/empty occupancy.

In accordance with the spin polarization of the band gap, we noted a finite magnetic moment in most alloys. Distinctly, the equimolar alloy contained a magnetic moment of $0.083\mu_B$ in all five configurations of the equimolar alloy. Upon investigation of the local magnetic moments, we discovered that the magnetism was mainly attributed to chromium and manganese atoms in the lattice. This was found as a general trend for all alloys based on the FeSi₂ structure. From this severe spin polarization of the band gap, a possible application of the Cr-Fe-Mn-Ni-Si alloys, could be as spintronics [67].

In terms of thermoelectric applications, we find limited success in respect to the band gap. Recalling that good thermoelectrics are semiconductors with band gaps around 0.2 eV, the band gaps of the (CrFeMnNi)Si₂ alloy are too small. However, we have found instances more suitable, such as the HSE06 band gap of 0.18 eV in one of the supercells, and the 0.1 eV band gap in Cr₃Fe₅Mn₅Ni₃Si₃₂. Furthermore, we can expect that the band gap of the real material to be larger than the PBE value, thus the Cr-Fe-Mn-Ni-Si system could have potential application as a thermoelectric.

Chapter 10

Future work

In future studies, I would first and foremost try to resolve several of the uncertainties circling the results presented in this project. This would include a more thoughtful investigation of the true ground state of the $(\text{CrFeMnNi})\text{Si}_2$ alloy. For example conduct a test of multiple configurations and a larger number of SQS sizes, in order reduce variance and obtain a converged value of the band gap. Secondly, to decide on the most representative configuration, we should have put more effort into correctly/optimally specify the magnetic configuration of each SQS. Also, a possible extension could be to study excited states, to account for entropic contributions to the stability. Moreover, a test of different crystal structures in addition to the orthorombic CMCE space group should be done, as the local minima method of DFT does not guarantee that this is the most stable conformation of the alloy.

The overarching motivation of this thesis has been to simply locate a band gap in high-entropy silicides. Now that we have located such a compound, in future work we could devote more effort into specifically analyze the band gap. Potentially try to plot and analyze the band structure of the alloys and qualitatively scrutinize the band gap by different band gap specific functionals. Furthermore, we performed only a very limited search of the quaternary phase diagram of the Cr-Fe-Mn-Ni-Si system, but found promising results in the direction of less chromium and more manganese. Thus, a future study on more deliberate compositions in these directions would also be interesting. Provided that these results yielded positive outcomes of the band gap, suitable for thermoelectric application, future work could focus on a complete study of this material as a thermoelectric, and consider properties such as the Seebeck coefficient, electrical conductivity, and thermal conductivity.

Appendix A

Figures

A.1 Density of states

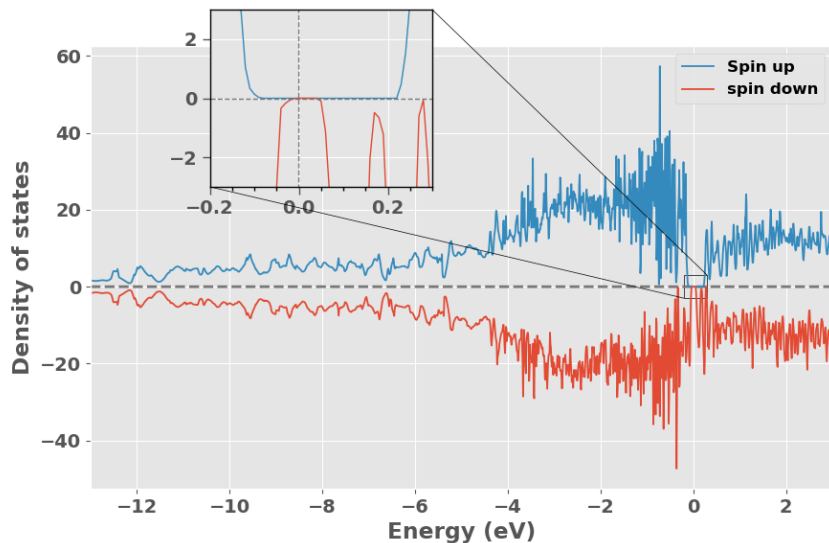


Figure A.1: Density of states [states/eV] of SQS E of (CrFeMnNi)Si₂.

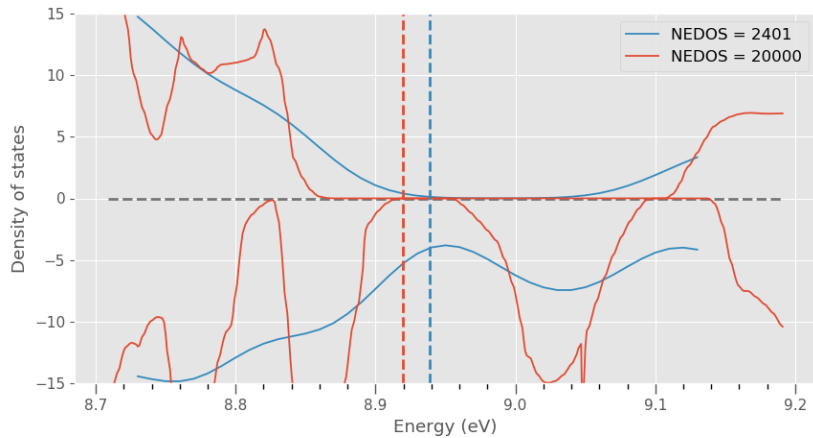


Figure A.2: Density of states [states/eV] of SQS C (CrFeMnNi) Si_2 . NEDOS represents the number of points in the DOS calculation.

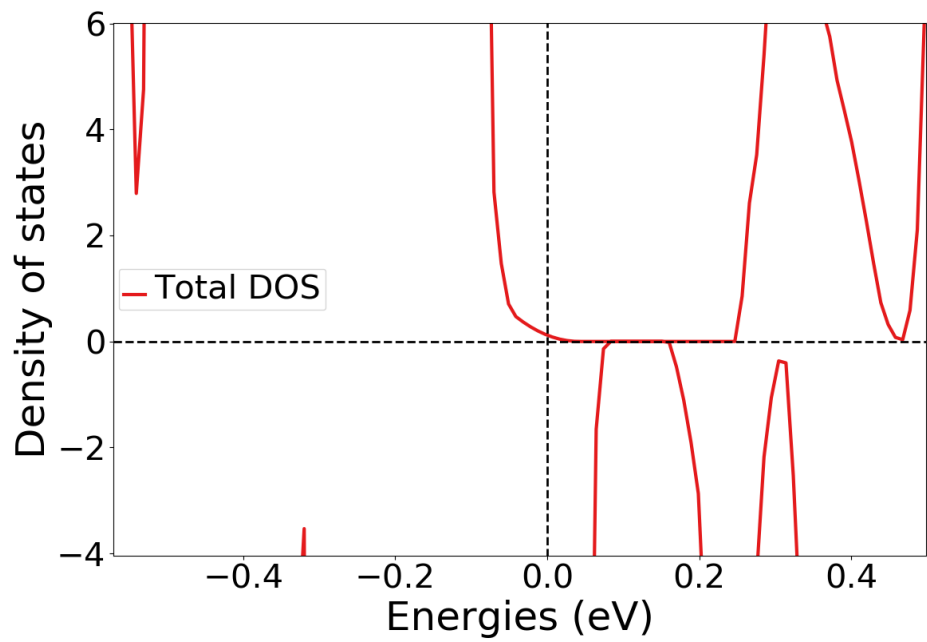


Figure A.3: Density of states [states/eV] of SQS C of $\text{Cr}_5\text{Fe}_5\text{Mn}_3\text{Ni}_3\text{Si}_{32}$, illustrating the small finite DOS at E_F due to the impurity gap.

A.2 Projected density of states

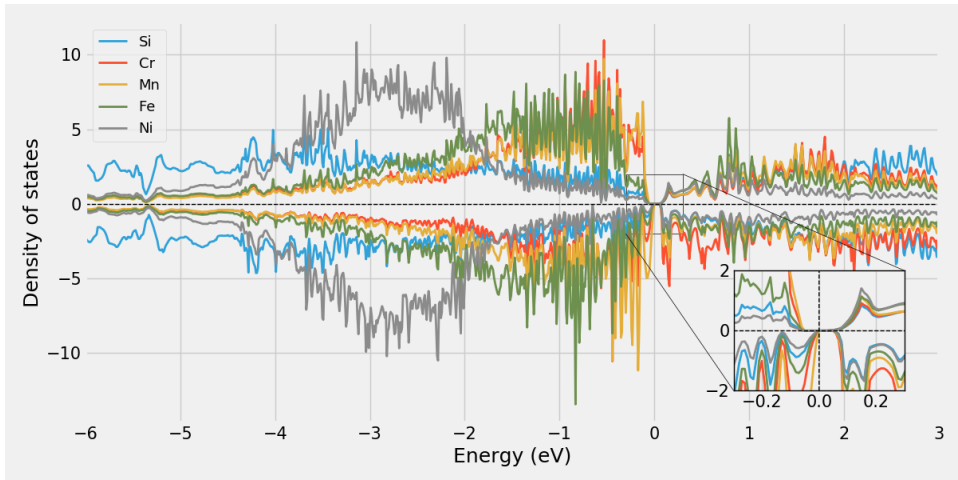


Figure A.4: Projected density of states [states/eV] of SQS A of (CrFeMnNi)Si₂

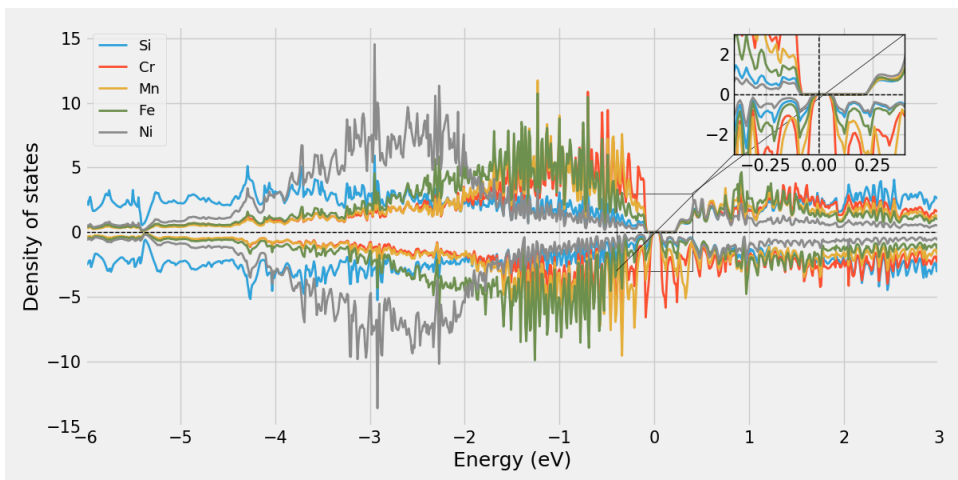


Figure A.5: Projected density of states [states/eV] of SQS B of (CrFeMnNi)Si₂

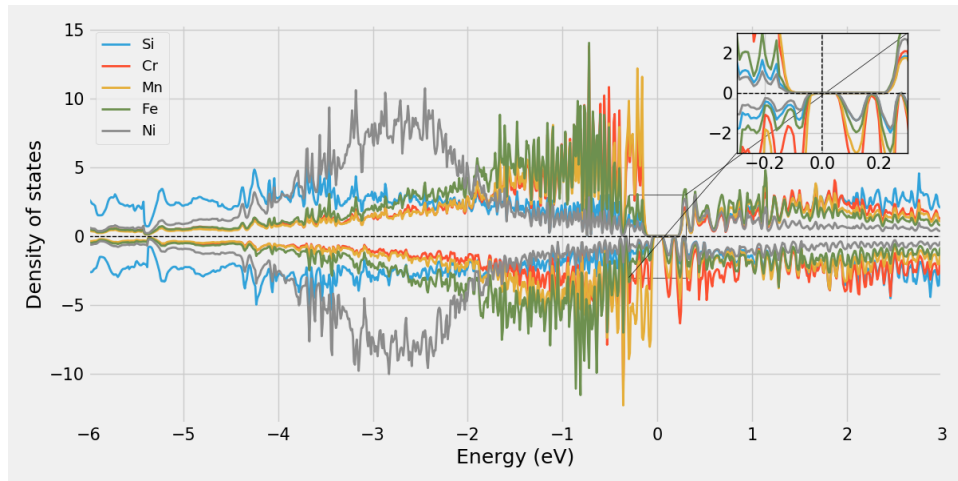


Figure A.6: Projected density of states [states/eV] of SQS E of $(\text{CrFeMnNi})\text{Si}_2$

A.3 Charge density

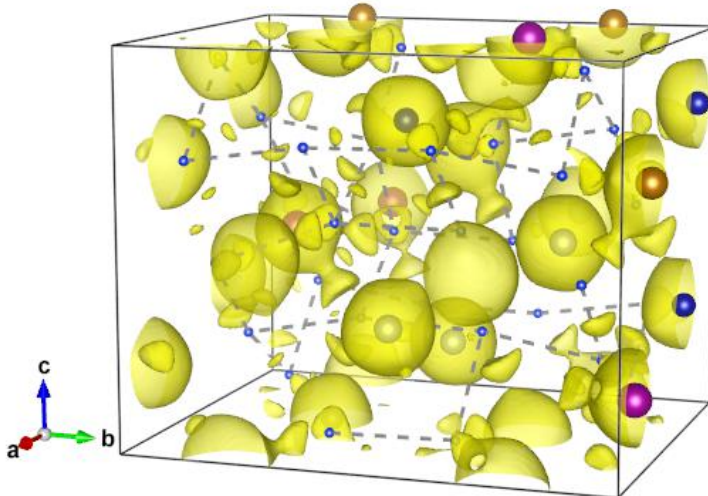


Figure A.7: Contour plot of the charge density of SQS C of $(\text{CrFeMnNi})\text{Si}_2$.

Bibliography

- [1] termoelektrisitet. *Velkommen til en termoelektrisk verden!* nor. Nov. 2013. URL: <https://termoelektrisitet.no/2013/11/24/velkommen-til-en-termoelektrisk-verden/> (visited on 24/11/2013).
- [2] Wikipedia. *Thermoelectric materials.* en. Page Version ID: 989933448. Nov. 2020. URL: https://en.wikipedia.org/w/index.php?title=Thermoelectric_materials&oldid=989933448 (visited on 22/11/2020).
- [3] Eddwi H. Hasdeo et al. 'Optimal band gap for improved thermoelectric performance of two-dimensional Dirac materials'. In: *Journal of Applied Physics* 126.3 (July 2019), p. 035109. ISSN: 1089-7550. DOI: 10.1063/1.5100985. URL: <http://dx.doi.org/10.1063/1.5100985>.
- [4] G. Jeffrey Snyder and Eric S Toberer. 'Complex thermoelectric materials'. eng. In: *Nature materials* 7.2 (2008), pp. 105–114. ISSN: 1476-1122.
- [5] Jorge Osvaldo Sofo and GD Mahan. 'Optimum band gap of a thermoelectric material'. In: *Physical Review B* 49.7 (1994), p. 4565.
- [6] Tsai. Ming-Hung and Yeh. Jien-Wei. 'High-Entropy Alloys: A Critical Review'. In: *Materials Research Letters* 2.3 (2014), pp. 107–123. DOI: 10.1080/21663831.2014.912690. eprint: <https://doi.org/10.1080/21663831.2014.912690>. URL: <https://doi.org/10.1080/21663831.2014.912690>.
- [7] Joshua Gild et al. 'A high-entropy silicide: (Mo_{0.2}Nb_{0.2}Ta_{0.2}Ti_{0.2}W_{0.2})Si₂'. In: *Journal of Materiomics* 5.3 (2019), pp. 337–343. ISSN: 2352-8478. DOI: <https://doi.org/10.1016/j.jmat.2019.03.002>. URL: <https://www.sciencedirect.com/science/article/pii/S2352847819300334>.
- [8] Mari Mathillas Røsvik. *Structural Characterization of High Entropy Metal Silicide Alloys.* 2021.
- [9] Burkov. A. 'Silicide Thermoelectrics: Materials for Energy Harvesting'. In: *physica status solidi (a)* 215 (June 2018). DOI: 10.1002/pssa.201800105.
- [10] Jien-Wei Yeh. 'Overview of High-Entropy Alloys'. In: *High-Entropy Alloys: Fundamentals and Applications.* Ed. by Michael C. Gao et al. Cham: Springer International Publishing, 2016, pp. 1–19. ISBN: 978-3-319-27013-5. DOI: 10.1007/978-3-319-27013-5_1. URL: https://doi.org/10.1007/978-3-319-27013-5_1.

- [11] Yong Zhang et al. ‘Phase Formation Rules’. In: *High-Entropy Alloys: Fundamentals and Applications*. Ed. by Michael C. Gao et al. Cham: Springer International Publishing, 2016, pp. 21–49. ISBN: 978-3-319-27013-5. DOI: 10.1007/978-3-319-27013-5_2. URL: https://doi.org/10.1007/978-3-319-27013-5_2.
- [12] Jien-Wei Yeh. ‘Physical Metallurgy’. In: *High-Entropy Alloys: Fundamentals and Applications*. Ed. by Michael C. Gao et al. Cham: Springer International Publishing, 2016, pp. 51–113. ISBN: 978-3-319-27013-5. DOI: 10.1007/978-3-319-27013-5_3. URL: https://doi.org/10.1007/978-3-319-27013-5_3.
- [13] Jien-Wei Yeh et al. ‘Functional Properties’. In: *High-Entropy Alloys: Fundamentals and Applications*. Ed. by Michael C. Gao et al. Cham: Springer International Publishing, 2016, pp. 237–265. ISBN: 978-3-319-27013-5. DOI: 10.1007/978-3-319-27013-5_7. URL: https://doi.org/10.1007/978-3-319-27013-5_7.
- [14] Lewis Robert Owen and Nicholas Gwilym Jones. ‘Lattice distortions in high-entropy alloys’. In: *Journal of Materials Research* 33.19 (2018), pp. 2954–2969. DOI: 10.1557/jmr.2018.322.
- [15] Tingting Zuo et al. ‘Tailoring magnetic behavior of CoFeMnNiX (X = Al, Cr, Ga, and Sn) high entropy alloys by metal doping’. In: *Acta Materialia* 130 (2017), pp. 10–18. ISSN: 1359-6454. DOI: <https://doi.org/10.1016/j.actamat.2017.03.013>. URL: <https://www.sciencedirect.com/science/article/pii/S1359645417302008>.
- [16] Oldřich Schneeweiss et al. ‘Magnetic properties of the CrMnFeCoNi high-entropy alloy’. In: *Phys. Rev. B* 96 (1 July 2017), p. 014437. DOI: 10.1103/PhysRevB.96.014437. URL: <https://link.aps.org/doi/10.1103/PhysRevB.96.014437>.
- [17] Fuyang Tian. ‘A Review of Solid-Solution Models of High-Entropy Alloys Based on Ab Initio Calculations’. In: *Frontiers in Materials* 4 (2017). ISSN: 2296-8016. DOI: 10.3389/fmats.2017.00036. URL: <https://www.frontiersin.org/article/10.3389/fmats.2017.00036>.
- [18] S.-H. Wei et al. ‘Electronic properties of random alloys: Special quasirandom structures’. In: *Phys. Rev. B* 42 (15 Nov. 1990), pp. 9622–9649. DOI: 10.1103/PhysRevB.42.9622. URL: <https://link.aps.org/doi/10.1103/PhysRevB.42.9622>.
- [19] Z. W. Lu, S.-H. Wei and Alex Zunger. ‘Electronic structure of ordered and disordered Cu₃ Au and Cu₃ Pd’. In: *Phys. Rev. B* 45 (18 May 1992), pp. 10314–10330. DOI: 10.1103/PhysRevB.45.10314. URL: <https://link.aps.org/doi/10.1103/PhysRevB.45.10314>.
- [20] Su-Huai Wei and Alex Zunger. ‘Band offsets and optical bowings of chalcopyrites and Zn-based II-VI alloys’. In: *Journal of Applied Physics* 78.6 (1995), pp. 3846–3856. DOI: 10.1063/1.359901. eprint: <https://doi.org/10.1063/1.359901>. URL: <https://doi.org/10.1063/1.359901>.

- [21] Michael C. Gao et al. 'Applications of Special Quasi-random Structures to High-Entropy Alloys'. In: *High-Entropy Alloys: Fundamentals and Applications*. Ed. by Michael C. Gao et al. Cham: Springer International Publishing, 2016, pp. 333–368. ISBN: 978-3-319-27013-5. DOI: 10.1007/978-3-319-27013-5_10. URL: https://doi.org/10.1007/978-3-319-27013-5_10.
- [22] A. van de Walle et al. 'Efficient stochastic generation of special quasirandom structures'. In: *Calphad* 42 (2013), pp. 13–18. ISSN: 0364-5916. DOI: <https://doi.org/10.1016/j.calphad.2013.06.006>. URL: <https://www.sciencedirect.com/science/article/pii/S0364591613000540>.
- [23] Shen Wang et al. 'Comparison of two calculation models for high entropy alloys: Virtual crystal approximation and special quasi-random structure'. In: *Materials Letters* 282 (2021), p. 128754. ISSN: 0167-577X. DOI: <https://doi.org/10.1016/j.matlet.2020.128754>. URL: <https://www.sciencedirect.com/science/article/pii/S0167577X20314610>.
- [24] Peng Wei et al. 'Understanding magnetic behaviors of FeCoN-iSi0.2M0.2 (M=Cr, Mn) high entropy alloys via first-principle calculation'. In: *Journal of Magnetism and Magnetic Materials* 519 (2021), p. 167432. ISSN: 0304-8853. DOI: <https://doi.org/10.1016/j.jmmm.2020.167432>. URL: <https://www.sciencedirect.com/science/article/pii/S0304885320323994>.
- [25] Muhammad Rashid et al. 'Ab-initio study of fundamental properties of ternary ZnO_{1-x}S_x alloys by using special quasi-random structures'. In: *Computational Materials Science* 91 (2014), pp. 285–291. ISSN: 0927-0256. DOI: <https://doi.org/10.1016/j.commatsci.2014.04.032>. URL: <https://www.sciencedirect.com/science/article/pii/S0927025614002742>.
- [26] V. Sorkin et al. 'First-principles-based high-throughput computation for high entropy alloys with short range order'. In: *Journal of Alloys and Compounds* 882 (2021), p. 160776. ISSN: 0925-8388. DOI: <https://doi.org/10.1016/j.jallcom.2021.160776>. URL: <https://www.sciencedirect.com/science/article/pii/S092583882102185X>.
- [27] Clas Persson. *A Brief Introduction to the Density Functional Theory*. 1st ed. Department of Physics, University of Oslo, 2020.
- [28] David S. Sholl and Janice A. Steckel. 'Density functional theory a practical introduction'. In: (2009).
- [29] Daniel W. Hook, Simon J. Porter and Christian Herzog. 'Dimensions: Building Context for Search and Evaluation'. In: *Frontiers in Research Metrics and Analytics* 3 (2018). <https://www.frontiersin.org/articles/10.3389/frma.2018.00023/pdf>, p. 23. DOI: 10.3389/frma.2018.00023. URL: <https://app.dimensions.ai/details/publication/pub.1106289502>.

- [30] Aron J. Cohen, Paula Mori-Sánchez and Weitao Yang. ‘Insights into Current Limitations of Density Functional Theory’. In: *Science* 321.5890 (2008), pp. 792–794. DOI: 10.1126/science.1158722. eprint: <https://www.science.org/doi/pdf/10.1126/science.1158722>. URL: <https://www.science.org/doi/abs/10.1126/science.1158722>.
- [31] John P. Perdew and Mel Levy. ‘Physical Content of the Exact Kohn-Sham Orbital Energies: Band Gaps and Derivative Discontinuities’. In: *Phys. Rev. Lett.* 51 (20 Nov. 1983), pp. 1884–1887. DOI: 10.1103/PhysRevLett.51.1884. URL: <https://link.aps.org/doi/10.1103/PhysRevLett.51.1884>.
- [32] Michael Foster and Karl Sohlberg. ‘Empirically corrected DFT and semi-empirical methods for non-bonding interactions’. In: *Physical Chemistry Chemical Physics - PHYS CHEM CHEM PHYS* 12 (Jan. 2010). DOI: 10.1039/b912859j.
- [33] Carlos Borca (<https://scicomp.stackexchange.com/users/8020/carlos-borca>). *Limitations of Density Functional Theory as a computational method?* Computational Science Stack Exchange. eprint: <https://scicomp.stackexchange.com/q/11443>. URL: <https://scicomp.stackexchange.com/q/11443>.
- [34] NobelPrize.org. *The Nobel Prize in Chemistry 1998*. Accessed: 2022-15-04. URL: <https://www.nobelprize.org/prizes/chemistry/1998/summary/>.
- [35] John P. Perdew et al. ‘Prescription for the design and selection of density functional approximations: More constraint satisfaction with fewer fits’. In: *The Journal of Chemical Physics* 123.6 (2005), p. 062201. DOI: 10.1063/1.1904565. eprint: <https://doi.org/10.1063/1.1904565>. URL: <https://doi.org/10.1063/1.1904565>.
- [36] John P Perdew and Yue Wang. ‘Accurate and simple analytic representation of the electron-gas correlation energy’. In: *Physical review B* 45.23 (1992), p. 13244.
- [37] John P Perdew, Kieron Burke and Matthias Ernzerhof. ‘Generalized gradient approximation made simple’. In: *Physical review letters* 77.18 (1996), p. 3865.
- [38] Fabian (<https://mattermodeling.stackexchange.com/users/295/fabian>). *What makes PBE the most preferred functional over other GGA functionals?* Matter Modeling Stack Exchange. URL: <https://mattermodeling.stackexchange.com/q/402>.
- [39] Jianmin Tao et al. ‘Climbing the Density Functional Ladder: Nonempirical Meta-Generalized Gradient Approximation Designed for Molecules and Solids’. In: *Phys. Rev. Lett.* 91 (14 Sept. 2003), p. 146401. DOI: 10.1103/PhysRevLett.91.146401. URL: <https://link.aps.org/doi/10.1103/PhysRevLett.91.146401>.

- [40] Fabien Tran and Peter Blaha. ‘Importance of the Kinetic Energy Density for Band Gap Calculations in Solids with Density Functional Theory’. In: *The Journal of Physical Chemistry A* 121.17 (2017). PMID: 28402113, pp. 3318–3325. DOI: 10.1021/acs.jpca.7b02882. eprint: <https://doi.org/10.1021/acs.jpca.7b02882>. URL: <https://doi.org/10.1021/acs.jpca.7b02882>.
- [41] Jianwei Sun, Adrienn Ruzsinszky and John P. Perdew. ‘Strongly Constrained and Appropriately Normed Semilocal Density Functional’. In: *Phys. Rev. Lett.* 115 (3 July 2015), p. 036402. DOI: 10.1103/PhysRevLett.115.036402. URL: <https://link.aps.org/doi/10.1103/PhysRevLett.115.036402>.
- [42] Jianwei Sun et al. ‘Accurate first-principles structures and energies of diversely bonded systems from an efficient density functional’. In: *Nature chemistry* 8.9 (2016), pp. 831–836.
- [43] Arup Chakraborty et al. ‘Predicting accurate cathode properties of layered oxide materials using the SCAN meta-GGA density functional’. In: *npj Computational Materials* 4.1 (2018), pp. 1–9.
- [44] Axel D Becke and Erin R Johnson. ‘A simple effective potential for exchange’. In: *The Journal of chemical physics* 124.22 (2006), p. 221101.
- [45] Carlo Adamo and Vincenzo Barone. ‘Toward reliable density functional methods without adjustable parameters: The PBE0 model’. In: *The Journal of Chemical Physics* 110.13 (1999), pp. 6158–6170. DOI: 10.1063/1.478522. eprint: <https://doi.org/10.1063/1.478522>. URL: <https://doi.org/10.1063/1.478522>.
- [46] Aliaksandr V. Kruckau et al. ‘Influence of the exchange screening parameter on the performance of screened hybrid functionals’. In: *The Journal of Chemical Physics* 125.22 (2006), p. 224106. DOI: 10.1063/1.2404663. eprint: <https://doi.org/10.1063/1.2404663>. URL: <https://doi.org/10.1063/1.2404663>.
- [47] Jochen Heyd, Gustavo E Scuseria and Matthias Ernzerhof. ‘Hybrid functionals based on a screened Coulomb potential’. In: *The Journal of chemical physics* 118.18 (2003), pp. 8207–8215.
- [48] Paula Mori-Sánchez and Aron J. Cohen. ‘The derivative discontinuity of the exchange–correlation functional’. In: *Phys. Chem. Chem. Phys.* 16 (28 2014), pp. 14378–14387. DOI: 10.1039/C4CP01170H. URL: <http://dx.doi.org/10.1039/C4CP01170H>.
- [49] Pedro Borlido et al. ‘Large-Scale Benchmark of Exchange–Correlation Functionals for the Determination of Electronic Band Gaps of Solids’. In: *Journal of Chemical Theory and Computation* 15.9 (2019). PMID: 31306006, pp. 5069–5079. DOI: 10.1021/acs.jctc.9b00322. eprint: <https://doi.org/10.1021/acs.jctc.9b00322>. URL: <https://doi.org/10.1021/acs.jctc.9b00322>.

- [50] G. Kresse and D. Joubert. ‘From ultrasoft pseudopotentials to the projector augmented-wave method’. In: *Phys. Rev. B* 59 (3 Jan. 1999), pp. 1758–1775. DOI: 10.1103/PhysRevB.59.1758. URL: <https://link.aps.org/doi/10.1103/PhysRevB.59.1758>.
- [51] P. E. Blöchl. ‘Projector augmented-wave method’. In: *Phys. Rev. B* 50 (24 Dec. 1994), pp. 17953–17979. DOI: 10.1103/PhysRevB.50.17953. URL: <https://link.aps.org/doi/10.1103/PhysRevB.50.17953>.
- [52] G. Kresse and J. Hafner. ‘Ab initio molecular dynamics for liquid metals’. In: *Phys. Rev. B* 47 (1 Jan. 1993), pp. 558–561. DOI: 10.1103/PhysRevB.47.558. URL: <https://link.aps.org/doi/10.1103/PhysRevB.47.558>.
- [53] G. Kresse and J. Hafner. ‘Ab initio molecular-dynamics simulation of the liquid-metal–amorphous–semiconductor transition in germanium’. In: *Phys. Rev. B* 49 (20 May 1994), pp. 14251–14269. DOI: 10.1103/PhysRevB.49.14251. URL: <https://link.aps.org/doi/10.1103/PhysRevB.49.14251>.
- [54] G. Kresse and J. Furthmüller. ‘Efficiency of ab-initio total energy calculations for metals and semiconductors using a plane-wave basis set’. In: *Computational Materials Science* 6.1 (1996), pp. 15–50. ISSN: 0927-0256. DOI: [https://doi.org/10.1016/0927-0256\(96\)00008-0](https://doi.org/10.1016/0927-0256(96)00008-0). URL: <https://www.sciencedirect.com/science/article/pii/0927025696000080>.
- [55] G. Kresse and J. Furthmüller. ‘Efficient iterative schemes for ab initio total-energy calculations using a plane-wave basis set’. In: *Phys. Rev. B* 54 (16 Oct. 1996), pp. 11169–11186. DOI: 10.1103/PhysRevB.54.11169. URL: <https://link.aps.org/doi/10.1103/PhysRevB.54.11169>.
- [56] Hellman. Olle et al. ‘Temperature dependent effective potential method for accurate free energy calculations of solids’. In: *Phys. Rev. B* 87 (10 Mar. 2013), p. 104111. DOI: 10.1103/PhysRevB.87.104111. URL: <https://link.aps.org/doi/10.1103/PhysRevB.87.104111>.
- [57] Anubhav Jain et al. ‘The Materials Project: A materials genome approach to accelerating materials innovation’. In: *APL Materials* 1.1 (2013), p. 011002. ISSN: 2166532X. DOI: 10.1063/1.4812323. URL: <http://link.aip.org/link/AMPADS/v1/i1/p011002/s1%5C&Agg=doi>.
- [58] Vei Wang et al. ‘VASPKIT: A user-friendly interface facilitating high-throughput computing and analysis using VASP code’. In: *Computer Physics Communications* 267 (2021), p. 108033. ISSN: 0010-4655. DOI: <https://doi.org/10.1016/j.cpc.2021.108033>. URL: <https://www.sciencedirect.com/science/article/pii/S0010465521001454>.
- [59] Shyue Ping Ong et al. ‘Python Materials Genomics (pymatgen): A robust, open-source python library for materials analysis’. In: *Computational Materials Science* 68 (2013), pp. 314–319. ISSN: 0927-0256. DOI: <https://doi.org/10.1016/j.commatsci.2012.10.028>. URL: <https://www.sciencedirect.com/science/article/pii/S0927025612006295>.

- [60] Koichi Momma and Fujio Izumi. ‘VESTA3 for three-dimensional visualization of crystal, volumetric and morphology data’. In: *Journal of Applied Crystallography* 44.6 (Dec. 2011), pp. 1272–1276. DOI: 10.1107 / S0021889811038970. URL: <https://doi.org/10.1107/S0021889811038970>.
- [61] S. J. Clark et al. ‘Structure and electronic properties of FeSi₂’. In: *Phys. Rev. B* 58 (16 Oct. 1998), pp. 10389–10393. DOI: 10.1103/PhysRevB.58.10389. URL: <https://link.aps.org/doi/10.1103/PhysRevB.58.10389>.
- [62] Voicu Popescu and Alex Zunger. ‘Effective Band Structure of Random Alloys’. In: *Phys. Rev. Lett.* 104 (23 June 2010), p. 236403. DOI: 10.1103/PhysRevLett.104.236403. URL: <https://link.aps.org/doi/10.1103/PhysRevLett.104.236403>.
- [63] R. Eppenga. ‘Ab initio band-structure calculation of the semiconductor β-FeSi₂’. In: *Journal of Applied Physics* 68.6 (1990), pp. 3027–3029. DOI: 10.1063/1.346415. eprint: <https://doi.org/10.1063/1.346415>. URL: <https://doi.org/10.1063/1.346415>.
- [64] H Lange. ‘Electronic properties of semiconducting silicides’. In: *physica status solidi (b)* 201.1 (1997), pp. 3–65.
- [65] ISMEAR - Vaspwiki. URL: <https://www.vasp.at/wiki/index.php/ISMEAR>.
- [66] Igor Levin. *NIST Inorganic Crystal Structure Database (ICSD)*. National Institute of Standards and Technology, 2018. URL: <https://doi.org/10.18434/M32147>.
- [67] Xingxing Li and Jinlong Yang. ‘First-principles design of spintronics materials’. In: *National Science Review* 3.3 (Apr. 2016), pp. 365–381. ISSN: 2095-5138. DOI: 10.1093/nsr/nww026. eprint: <https://academic.oup.com/nsr/article-pdf/3/3/365/31566317/nww026.pdf>. URL: <https://doi.org/10.1093/nsr/nww026>.